Solar Electron Beam Transport in the Inner Heliosphere

Hamish Andrew Sinclair Reid, BSc, MSc

Astronomy and Astrophysics Group

Department of Physics and Astronomy

Kelvin Building

University of Glasgow

Glasgow, G12 8QQ

Scotland, U.K.

Presented for the degree of

Doctor of Philosophy

The University of Glasgow

October 2010

To my parents, John and Aenea, my brother Iain and my partner in life, Holly

This thesis is my own composition except where indicated in the text. No part of this thesis has been submitted elsewhere for any other degree or qualification.

08 October 2010

Abstract

Impulsive solar electron beams have an attractive diagnostic potential for poorly understood particle acceleration processes in solar flares. Solar flare accelerated electron beams propagating away from the Sun can interact with the turbulent interplanetary media, producing Langmuir waves and type III radio emission. In this thesis, we simulate electron beam propagation from the Sun to the Earth in the weak turbulent regime taking into account the self-consistent generation of Langmuir waves. We show that an injected single power-law spectrum will be detected at 1 AU as a broken power-law due to wave-particle interaction in the inhomogeneous plasma. We further extend these results by investigating the Langmuir wave interaction with background electron density fluctuations from low frequency MHD turbulence. We find a direct correlation between the spectra of the double power-law below the break energy and the turbulent intensity of the background plasma.

Solar flares are believed to accelerate both upward and downward propagating electron beams which can radiate emission at radio and X-ray wavelengths correspondingly. The correlation between X-ray and radio emissions in a well observed solar flare allowed us detailed study of the electron acceleration region properties. We used the Nançay Radioheliograph, Phoenix-2 and RHESSI to infer the type III position, type III starting frequency and spectral index of the HXR emission respectively. Using these datasets and numerical simulations of the electron beam transport in the corona plasma, we were able to infer not only the location (the height in the corona), but to estimate the spatial length of the electron acceleration site.

Contents

Bibliography

List of Figures

Preface

This thesis deals with the propagation of solar flare accelerated electron beams travelling from the Sun to the Earth. Specifically we are simulating the wave-particle interactions which occur between high energy ($> 1\,\mathrm{keV}$) electrons and Langmuir waves.

Chapter 1 reviews the necessary background material relevant to this thesis. The basic understanding of a solar flare is introduced, with particular emphasis on energy release and accelerated electrons. The chapter then describes the physics behind the resonant interaction between electrons and Langmuir waves and the emission of radio waves by the Langmuir waves. It then concludes with a summary of the different types of observable radio bursts and their properties.

Chapter 2 starts by introducing the properties of observed in-situ electron beams near the Earth. A description of the physical terms initially simulated is given together with the initial conditions for the electron beam, thermal Langmuir waves and background electron density. Analysis of the resultant beam-plasma structure is given followed by discussion of the electron beam fluence spectrum at the Earth

Chapter 3 introduces the topic of background electron density turbulence in the solar wind. The numerical model from the previous chapter is improved to more realistically simulate solar electron beams. The chapter then investigates how Langmuir waves interact with background density fluctuations and discusses how this further alters the fluence spectrum of the electron beam.

Chapter 4 diverts from the previous theoretical chapters by observationally analysing a solar flare's radio and HXR spectra. The theory of HXR spectra is briefly summarised together with the reasons for simultaneous study of HXR and radio emission. The chap-

ter derives a relation between observed emission parameters and unknown acceleration region properties. It then goes on to find the observed parameters from the flare's HXR and radio data and estimate the acceleration region height and size. Numerical simulations of electron beam transport are then employed to verify the estimated acceleration region properties.

Chapter 5 concludes the thesis with discussion about how the electron beam simulations can be related to observed type III properties. This final chapter also discusses future work which will be carried out to further our understanding of solar electron beam transport.

Acknowledgements

Thanks also goes out to Nicole who helped with a chapter of this thesis and for taking me into the next stage of my research career. I can only hope it will be as successful and enjoyable as this PhD has been.

A final thanks goes to my internal and external examiners Alex and Sarah for many useful comments which have helped to polish off this thesis.

Chapter 1

Introduction

The main aim of this thesis is to explore the transport of high energy (> 1 keV) solar electron beams from the Sun to the Earth, accelerated during solar flares. Propagation of energetic electron beams is a non-trivial subject on account of wave-particle interactions which occur with the background solar wind plasma inducing Langmuir waves. This chapter initially reviews the common understanding of solar flare physics. It then goes on to review the physics behind electron transport with emphasis on induced Langmuir waves. The chapter concludes by describing the properties of radio emission created through Langmuir waves undergoing wave-wave interactions.

1.1 Flare Overview

1.1.1 General solar flare description

Solar flares, magnetically driven explosions in the solar atmosphere, are a very impulsive phenomena. Solar flares are caused by the local coronal magnetic field becoming unstable and changing from a high energy, stressed topology to a low energy, relaxed topology. The difference in energy is released into the solar atmosphere which accelerates the surrounding particles to very high velocities with respect to the quasi-thermal level.

The origin of flares lies below the optically thick surface of the Sun. The turbulent

convection zone below the photosphere creates complex plasma flows that develop concentrated regions of magnetic field. This magnetic field rises through the photosphere and into the solar atmosphere via magnetic buoyancy. The magnetic field remains anchored in the dynamic photosphere/convection zone which adds shear and twist to the field. The free magnetic energy[1] increases, storing energy in magnetic form over periods of hours to weeks. Storing of energy cannot happen indefinitely and the plasma reaches a critical point where an instability occurs, releasing some large fraction of stored energy over a period of minutes to hours. This release of energy is known as a solar flare.

Solar flare energy release is typically described in three phases; pre-flare, impulsive, and decay. The majority of this energy is believed to be released in the impulsive phase which can last for at most 10^3 s during which they eject a huge amount of energy (between $10^{29} - 10^{33}$ ergs) into the solar atmosphere at heights around $10^9 - 10^{10}$ cm from the photosphere[2]. The energy goes into both accelerating particles and waves in the background coronal plasma. These waves and particles interact both with each other and with the coronal and chromospheric ambient plasma, releasing photons from radio waves through to gamma rays.

The most observed by-product of a solar flare are electron beams. Electron beams travel both downwards into the dense chromospheric plasma and upwards into the rarefied upper corona and inner heliosphere. They create emission at a variety of different wavelengths that can be detected via spacecraft and ground based telescopes. The two wavelengths of emission we are going to focus on in this thesis are radio waves and to a lesser extent Hard X-rays (HXR).

Upward propagating electron beams can travel into the high corona and inner heliosphere to produce coherent radio bursts (Section 1.4). These radio bursts typically start at a few hundred MHz and over time can drift down to a few tens of KHz (Dulk 1985). The decreasing frequency over time tracks the local plasma frequency where

---

[1]The difference in energy between the force free field and the potential field

[2]There is still quite a lot of uncertainty in the solar flare acceleration height. See Chapter 4 for a further discussion.

the electron beam is present.

HXRs are emitted from non-thermal electron beams accelerated in the corona which travel downwards into the dense chromosphere (Section 4.1.1). HXR emission is released through electron-ion bremsstrahlung emission (Arnoldy et al. 1968, see also review by Vilmer 1987). Most of their energy heats the chromospheric plasma (McDonald et al. 1999) to millions of degrees which rises to the low corona due to the pressure difference. Through collisional losses, this heated plasma radiates soft X-rays (SXR) (Emslie 1989).

A pictorial representation of a flare emitting X-rays and radio waves is shown in Figure 1.1. Believed to be accelerated by the same process, the generation of these oppositely directed electron beams has been reported to be temporally correlated (e.g. Arzner & Benz 2005, see also review by Pick & Vilmer 2008 and Chapter 4).

1.1.2 Solar flare energy

The loss of magnetic equilibrium starting the energy release in solar flares is usually considered to be their cause. Gravitational, thermal and nuclear energy in such a small rarefied area in the corona associated with solar flares is not enough to meet the high energy requirement of 10^{32} ergs (e.g. Priest & Forbes 2002). There are two magnetic field properties which have been previously related to solar flares, namely the unsigned magnetic flux Φ of the active region at the photosphere and a measure of the unsigned flux near strong-field polarity inversion lines (Welsch et al. 2009). This gives the picture of both strong regions of oppositely signed magnetic flux converging due to photospheric flows and flux emergence as drivers for the loss of magnetic equilibrium. The exact generation mechanism is not part of the modelling undertaken in this thesis.

Magnetic Reconnection

The loss of magnetic equilibrium whereby the magnetic field relaxes to a lesser energy state occurs through a process called magnetic reconnection. The topic of magnetic reconnection is highly complex and not the focus of this work so just a brief outline is
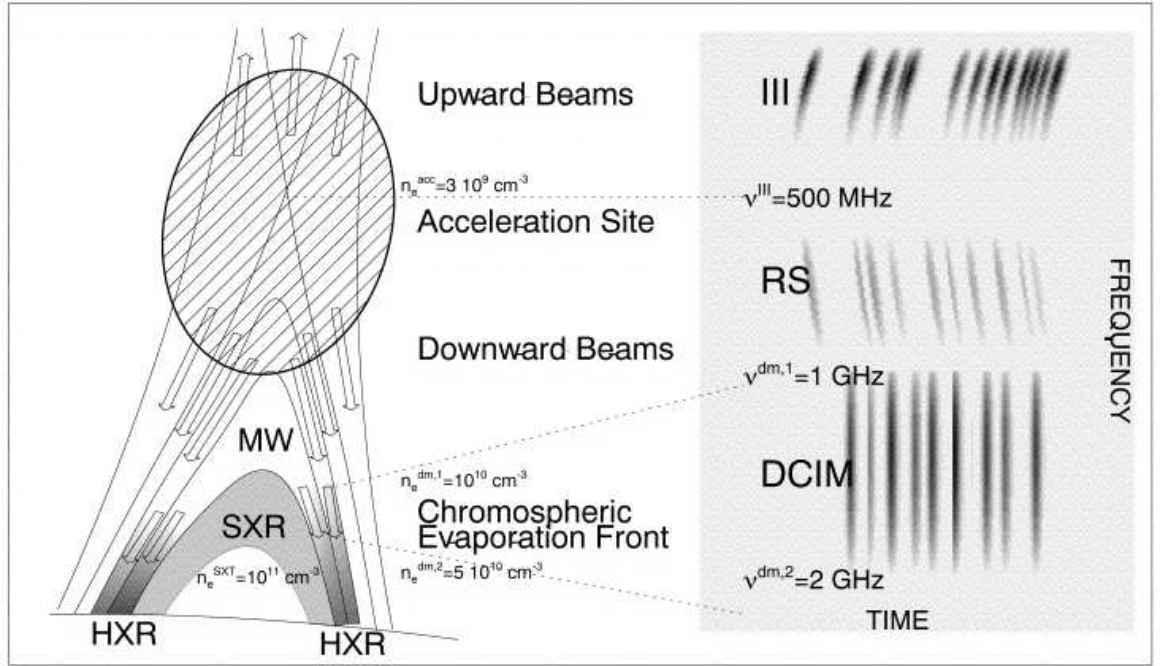
Figure 1.1: Diagram of a flare model envisioning magnetic reconnection and chromospheric evaporation processes in the context of our electron density measurements. The panel on the right illustrates a dynamic radio spectrum with radio bursts (see Section 1.4) indicated in the frequency-time plane (Aschwanden & Benz 1997). DCIM is decimetric radio emission and RS is reverse slope type III radio bursts.

given here. Interested parties are directed to reviews by Priest & Forbes (2000, 2002); Aschwanden (2002).

One of the simplest[3] reconnection models considered is steady 2D reconnection. When oppositely directed magnetic fields converge towards each other a boundary (diffusion) region is created. In this diffusion region the magnetic field can change connectivity such that positive polarity is able to flow to a different negative polarity. Magnetic field magnitude in the diffusion region tends to zero, increasing the plasma β[4] to values above unity. Plasma is then able to flow perpendicular to the magnetic field. The magnetic pressure also increases, causing the field to relax outwards via

---

[3]Sadly reconnection in any form is far from simple.

[4]A ratio of the plasma pressure to the magnetic pressure
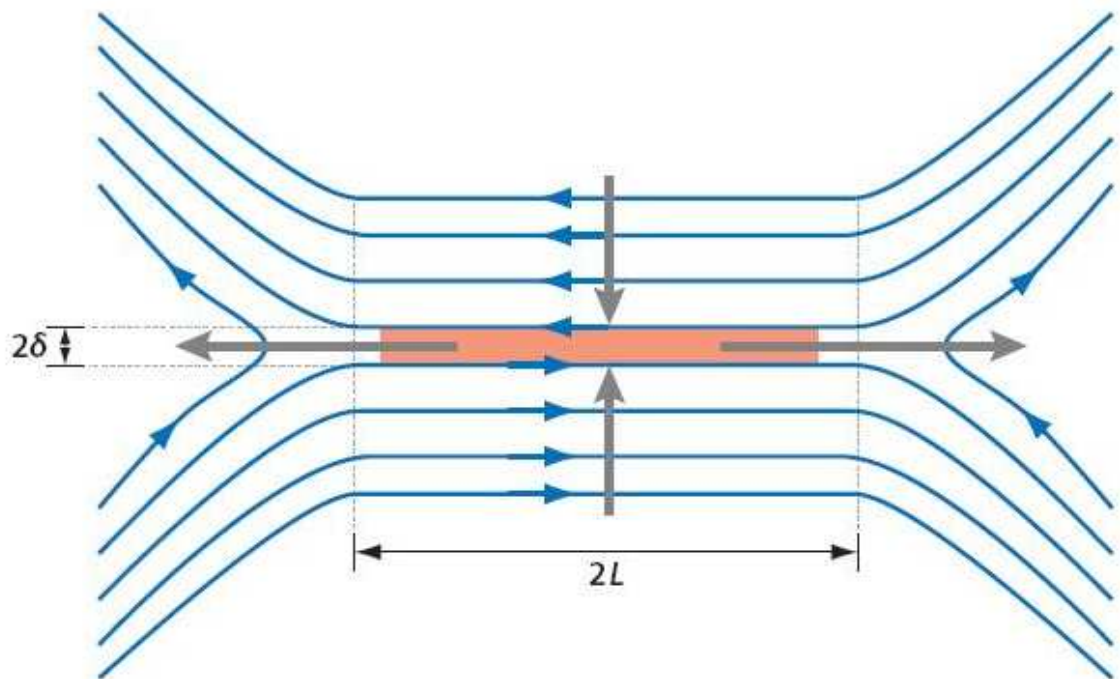
Figure 1.2: Diagram of Sweet-Parker reconnection showing the inflow and outflow of the bulk plasma (grey arrows) and the diffusion region (pink rectangle) (Zweibel & Yamada 2009)

the magnetic tension force. This relaxation process can 'slingshot' particles and is the basic conversion mechanism of magnetic to kinetic energy. The Lorentz force creates an electric field perpendicular to both the inflow and outflow of the bulk plasma, accelerating particles. The induced current layer in the diffusion region forms a current sheet.

One of the first models for 2D steady reconnection is the Sweet-Parker current sheet flare model (Figure 1.2) proposed by Sweet (1958); Parker (1963). In this model the diffusion region is much longer than it is wide. Unfortunately the energy conversion is too slow to explain solar flares on account of plasma having to flow along this narrow current sheet. An alternative model was introduced by Petschek (1964) which proposed a much smaller diffusion region allowing energy conversion to happen on

timescales $< 10^3$ s. After later numerical simulations by Biskamp (1986) a series of more general 2D reconnection models were developed, namely the 'almost-uniform', the 'non-uniform' and the 'burst' models (Priest & Forbes 2002).

Unsteady 2D reconnection models also exist where the reconnection becomes impulsive. When current sheets form they are susceptible to resistive instabilities. A long current sheet can become unstable to the tearing mode instability. The tearing mode instability gives rise to magnetic islands. These are able to very efficiently accelerate electrons (e.g. Kliem 1994; Drake et al. 2006) through a Fermi process where electrons are reflected from the ends of the magnetic island, experiencing the same small electric field many times.

If one goes from 2D to 3D then the geometry becomes even more complicated. The lines separating oppositely directed magnetic fields become a 2D separatrix surface. When two separatrix surfaces meet they create 1D separatrix lines which can meet to form null points where the magnetic field is zero. 3D reconnection gives rise to three different types of reconnection: 'spine', 'fan' and 'separator' reconnection (Priest & Forbes 2000).

Particle Acceleration

To accelerate the observed electron beams in solar flares requires substantial particle acceleration. There are three forms of particle acceleration considered for solar flares:

- DC electric field acceleration.

- Stochastic acceleration.

- Shock acceleration.

The requirements for any acceleration model is that it can explain the high energies ($>$ 100 keV) that electrons are accelerated to, the number of electrons that are accelerated, the power-law energy spectra of the electron beams observed and the fast timescales of energetic electrons.

DC acceleration can be classified into two regimes of sub and super Dreicer electric fields. The Dreicer electric field is defined as

$$E_D = \frac{e \ln \Lambda}{\lambda_D^2} \tag{1.1}$$

where $\ln \Lambda$ is the Coulomb logarithm and λ_D is the Debye length (e.g. Holman 1985). If the electric field is larger than E_D a particle with thermal velocity v_{Te} is able to be freely accelerated out of the thermal distribution. Holman (1985) finds that sub-Dreicer electric fields are able to explain HXR emitting electron beams given electric fields over the scale of 10 Mm. Unfortunately to explain the number of HXR producing electrons the electric current associated with the beam needs to be so large that its magnetic field would exceed typical coronal values by a few orders of magnitude (Litvinenko 2003). Moreover, such a large current sheet would be susceptible to the tearing mode instability and generate magnetic islands. Super-Dreicer electric fields have the advantage of explaining HXR emitting electron beams by acceleration over much shorter distances. The acceleration times are a few milliseconds and could correspond to the burstiness of HXR observations (see Litvinenko 2003, for a review).

Stochastic acceleration involves an AC electric field associated with waves to energise electrons. The basic theory of wave-particle interactions is covered in the next section. Whistler waves are one candidate which could accelerate electrons to high enough energies. Numerical simulations by Hamilton & Petrosian (1992) found that fits to the HXR spectra are possible with loop lengths of 100 Mm and electrons are able to be accelerated up to a few MeV. Another candidate is Langmuir waves. These run into the problem of having waves at high enough phase velocities to explain the acceleration of electrons up to energies of MeV (Melrose 1980b).

Shock acceleration is another way of generating high energy electrons. The underlying principle of shock acceleration is a Fermi process developed in 1949 by Fermi to explain how magnetic clouds accelerate particles to cosmic ray energies. This considers particles interacting with a magnetic mirror. If the particle has an opposite velocity to the moving mirror, it gains energy and vice versa. Fermi then developed this theory into two types of acceleration mechanism. The first ('first order Fermi') is via mag-

netic mirrors moving closer together with particles gaining energy at every reflection. The second ('second order Fermi') involves a stochastic motion of the magnetic mirrors where particles are statistically more likely to have energy gaining reflections than energy losing ones. Shock acceleration in the corona from flares is most likely second order Fermi due to the small observed timescales (Benz 2002). In this second order Fermi process electrons are reflected through the shock front upstream and downstream via resonant interaction of whistler waves. Particle energy varies stochastically in both directions, however, they have a net gain in energy from their more frequent head on encounters with the shock. Shock acceleration is a candidate for energizing particles in solar flares if the required turbulent wave spectrum is present.

1.1.3   Interplanetary particles

When solar flares release energy, many particles are accelerated up to high speeds. It is widely believed that non-relativistic electrons in the 10-100 keV are energetically the dominant component of flare-accelerated particles (e.g. Ramaty et al. 1980). The mass ratio $m_p/m_e = 1836$ means that the lighter electrons are roughly 2000 times easier to accelerate to high energies. These particles are sometimes able to escape the solar atmosphere and propagate towards Earth along the magnetic field of the Parker spiral (Figure 1.3).

Information on the spectra and ratio of energetic particles at the Earth can give important clues for unravelling the properties of the acceleration mechanism and electromagnetic radiation (normally at radio wavelength) radiated by the particles during transport. The energy spectra at 1 AU represents the combined effect of particle acceleration, coronal transport, release into the inner heliosphere and interplanetary propagation. It is a non-trivial task to find out which properties of the particle spectra are transport related and which are properties of the acceleration region. Moreover, acceleration is also possible in the collisionless inner heliosphere from complicated electromagnetic fields created via shocks, reconnection and wave modes.

The propagation of electron beams is an important topic to study. Electron beams
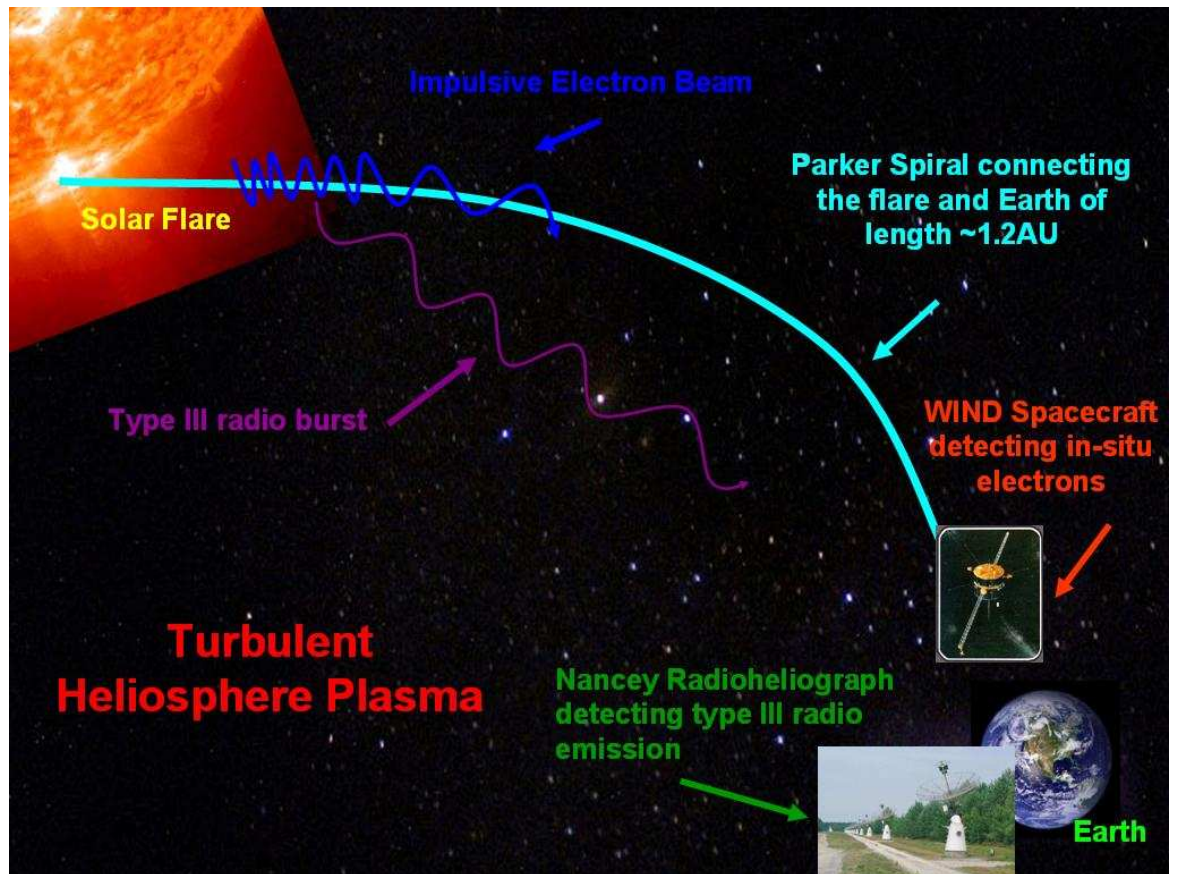
Figure 1.3: Overview of Electron Transport (Reid & Kontar 2009).

are ubiquitous to all solar flares so in this context they can convey lots of insight into what is happening in the solar atmosphere. Electron beams are also closely related to Coronal Mass Ejections (CMEs), dense blobs of plasma which are forcefully ejected into the heliosphere. CMEs are a huge problem for Earth satellites which have to shut down while the storm of particles passes over the Earth. Whilst potentially conveying some early warning of CMEs due to their much faster velocities, electron beams can also be a problem for satellites themselves, causing damage to solar cells and interfering with onboard electronics. Out of the solar context the further understanding of electron beams is a much broader topic, spanning disciplines from lab plasmas to cosmology.

1.1.4 Numerical plasma modelling

To model solar plasma, a variety of different approaches have been utilised depending upon the scale of interest. This thesis will use the kinetic approach, however, other numerical methods are also summarised.

The microscopic scale is modelled through discrete particle orbits in an electromagnetic field known as the test particle approach. In this scenario, the particle trajectories are calculated explicitly through the force equation

$$m\frac{dv}{dt} = q(E + \frac{v}{c} \times B)$$
(1.2)

where m, v, q is particle mass, velocity and charge respectively. E and B are the surrounding electric and magnetic field experienced by the particle. The motion of particles does not affect the surrounding electric and magnetic field so this approach lacks self consistency. It is also numerically time consuming, since large numbers of particles need to be modelled. The independent propagation of particles does lend itself to parallel computation which can speed up the process.

The macroscopic scale is typically modelled as a fluid using the Magnetohydrodynamics (MHD) approach. In this scenario, the plasma is treated as a fluid with a Maxwellian distribution where particles move along magnetic fields. This treatment is justified assuming the collisional time is very small with respect to other important processes. Electromagnetic fields are derived from Maxwell's equations, which describe a precise mathematical framework for evolving the system over time. There are a variety of different types of MHD models ranging from the simple 'Ideal MHD' where resistivity $\eta_r = 0$ to 'Hall MHD' where $\eta_r \neq 0$ and the Hall current term is considered. MHD is a powerful tool for analysing the collective dynamics of many particles and the resultant electromagnetic fields. What it doesn't capture are any effects where the velocities of particle distributions are able to become non-Maxwellian through wave-particle interactions or non-thermal particle beams.

The third, more complete mathematical description of plasma can be modelled through the kinetic approach. The crux of this idea involves applying statistical mechanics to the plasma. In this approach each species of particle is modelled over time

using a distribution function with dimensions in both position and velocity space. This allows the interaction of a large ensemble of particles to be described without modelling individual particle-particle interaction. The distribution function together with the mean electromagnetic field can describe a self-consistent solution using the Vlasov equation[5]

$$\frac{\partial f}{\partial t} + v\frac{\partial f}{\partial x} + \frac{q}{m}(E + \frac{v}{c} \times B)\frac{\partial f}{\partial v} = 0 \tag{1.3}$$

where $f(v,x,t)$ is a particle distribution function with fields E and B being calculated through Maxwell's equations. The distribution function has the useful property that

$$n(x,t) = \int f(v,x,t)d^3v \qquad N(t) = \int n(x,t)d^3x \tag{1.4}$$

where $n(x,t), N(t)$ are the number density and total number of particles respectively. Such properties are very useful becuase they allow some numerical checks to be performed on simulations. Provided any terms which remove energy from the system are ignored, the number of particles should be conserved. Moreover, if there is no terms varying in positing, the number density is conserved. Numerical checks allow the validity of simulations to be explored.

The power of the kinetic approach is being able to self-consistently deal with the entire system whilst also modelling particle movement in phase space. The main drawback in the kinetic approach is the computational time it takes to model 7 dimensional space (3 position, 3 velocity, 1 time). For a plasma, the kinetic approach breaks down if there are not enough particles per cubic Debye length. Fortunately this is not a problem for the solar corona. The kinetic approach is the basis of the computational modelling of electrons described in the following chapters. Consideration of electron motion in phase space is crucial to model wave-particle interactions described in the next section. Moreover, Coulomb collisions are not the dominant process for electrons in the inner heliosphere.

A significant proportion of this thesis involved the numerical modelling of electron beams[6]. The core modelling of the electron beam dynamics was done in Fortran using

---

[5]Vlasov's equation is a collisionless form of the Boltzmann equation
[6]see Chapters 2 and 3 for a discussion of the physics

a previously developed code (Kontar 2001c). Fortran was selected for its speed in iterating through many computational timesteps. The initial code was substantially altered through the course of the thesis to incorporate many new physical processes and to model a variety of different initial electron beams. The output of the electron beam evolution was saved at set time intervals for further analysis after the simulations had completed.

IDL (Interactive Data Language) was used as the tool for analysing the data obtained from the core Fortran code. The IDL language was selected because of its frequent usage in solar physics observational data analysis and it boasts a comprehensive library of routines known as SolarSoft. Data files were read into memory, however, SolarSoft was barely used for the analysis, being more suited to instrument data. A wide array of different programs were created to analyse the data, to gain a deeper understanding of electron beam propagation, to output the many graphs presented in this thesis and to check the consistency of the Fortran code for making sure it was simulating the physical processes correctly.

1.2   Beam-plasma instability

The focus of this thesis is on outwardly propagating electron beams accelerated in solar flares. Radio emission from these beams is known as type III radio bursts. In the standard scenario, the non-linear interaction of beam-driven plasma waves leads to the appearance of type III solar/interplanetary radio emission. The observations of type III solar bursts and energetic particles (Lin et al. 1981; Ergun et al. 1998; Gosling et al. 2003; Krucker et al. 2007) as well as theoretical (Zheleznyakov & Zaitsev 1970; Zaitsev et al. 1972; Mel'Nik 1995) and numerical investigations (Magelssen & Smith 1977; Grognard 1982; Kontar et al. 1998; Yoon et al. 2000; Kontar 2001d; Li et al. 2006a; Ledenev et al. 2004; Krasnoselskikh et al. 2007) provide strong support to the standard type III model.

The rest of this introduction chapter will summarise the basic theory behind the 'standard model' for radio emission from high-energy electron beams and provide an

overview of the observed radio emission properties. It also describes the basic physics that was the starting point for the computational simulations in this thesis.

1.2.1   Wave-particle interactions

The idea of electron beams being responsible for type III radio emission was first developed by Ginzburg & Zhelezniakov (1958). They attributed Langmuir waves[7] to be responsible for the generation of electromagnetic waves at the local plasma frequency. These Langmuir waves are generated through the two stream instability (specifically the more intuitively named bump-in-tail instability). The instability deals with two streams of electrons travelling at different speeds. Specifically for this situation there exists a background Maxwellian plasma with thermal velocity v_{Te} (temperature T_e) and density n_e. There also exists a high energy electron beam which is travelling at velocities around $20v_{Te}$ with density n_b.

The instability is caused by faster electrons outpacing slower electrons. Given a collisionless plasma, electrons are free to travel uninhibited (or adiabatically). From an initial power-law distribution of non-thermal electrons the fastest electrons will reach areas of space before the slower electrons. A positive slope in velocity space is created which is unstable to the generation of Langmuir waves. If a high enough density of non-thermal particles is present, a resonant wave-particle interaction will occur inducing a high level of Langmuir waves in the background plasma.

To visualise this process we have created a one dimensional example of this unstable distribution function (Figure 1.4). The initial distribution function is a combination of a thermal Maxwellian distribution with $v_{Te} = 5.5 \times 10^8$ cm s^{-1} ($T_e = 1$ MK) plus a non-thermal power-law tail (electron beam) with density ratio $n_b/n_e = 10^{-3}$ and spectral index 7 in velocity space. The electron beam has a spatially exponential

---

[7]Irving Langmuir(1881 - 1957) undertook work on thermionic electrons in low pressure atmospheres that led him to recognise the existence of plasmas, a name he coined, and oscillations of electron density in plasmas, now called Langmuir waves. These waves are caused by a restoring force to density perturbations that result from both changes in local electron density pressure and from local electrical polarisation.
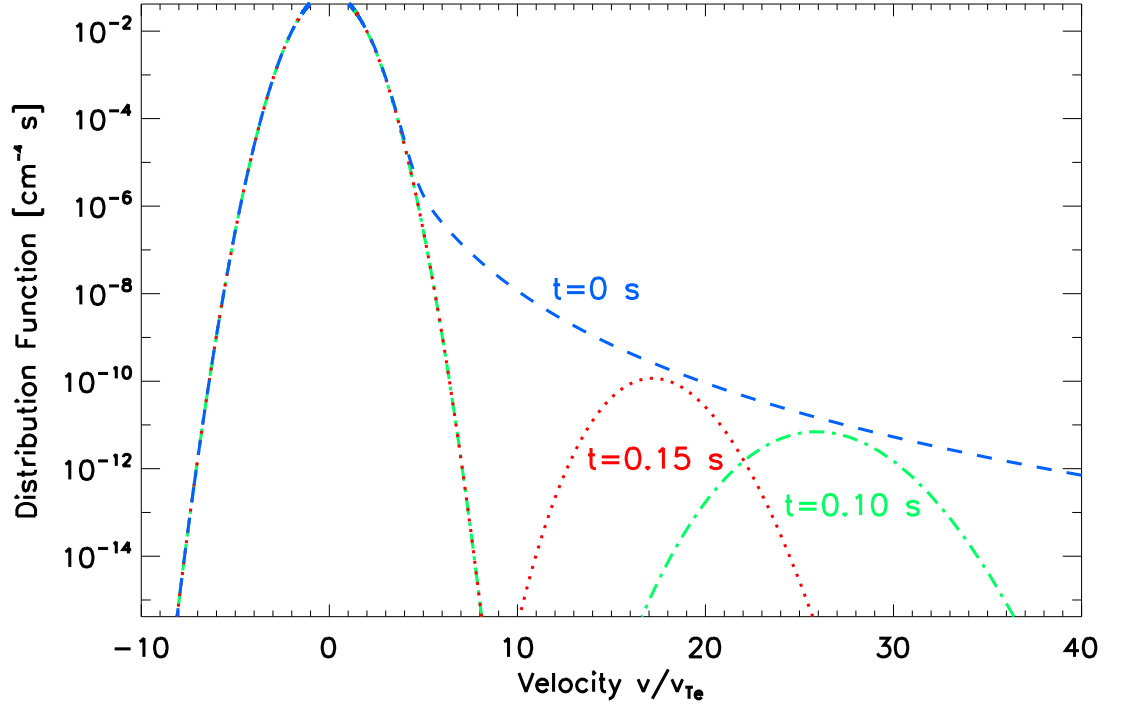
Figure 1.4: The evolution of a thermal Maxwellian and non-thermal electron beam with density ratio $n_b/n_e = 10^{-3}$, $v_{Te} = 5.5 \times 10^8$ cm s^{-1} demonstrating the bump-in-tail instability. The blue dashed line shows the distribution function at $t = 0$ s, $x = 0$ cm. The green and red dashed lines show the electron distribution at later times $t = 0.1$ s, $t = 0.15$ s respectively at $x = 1.5 \times 10^{10}$ cm. Note the development of the positive gradient $\partial f/\partial v > 0$ due to velocity dispersion.

distribution around $x = 0$ with characteristic size 10^9 cm. At later times the higher velocity particles have outpaced the slower particles and arrived at $x = 1.5 \times 10^{10}$ cm first. This creates a point in space where $\partial f/\partial v > 0$ for the electron distribution function $f(v, x, t)$.

It is important to mention the exchange of energy between particles and waves is due to Cerenkov radiation (Cerenkov 1934). Cerenkov radiation is typically known as the emission of electromagnetic radiation when a charge passes through a medium with velocity faster than the speed of light, $v > c/\xi$, where ξ is the refractive index of the

medium (a review can be found in Jelley 1958). The process is similar to the bow waves of a boat moving through water faster than the velocity of the surface waves. In an unmagnetised plasma the refractive index is always less than one. An electron cannot reach velocities faster than the speed of light and therefore electrons cannot induce electromagnetic waves in this way. Langmuir waves are present in a plasma with phase velocities slower than the speed of light and as such an electron can induce Langmuir waves in a plasma through Cerenkov radiation. For electrons to induce Langmuir waves the Cerenkov resonant condition $\omega = kv$ must be satisfied where ω, k are the Langmuir wave angular frequency and wavenumber respectively.

The emission of Langmuir waves by particles transfers energy from the particles to the waves. The growth rate of this process can be found from the quasilinear equations introduced by Vedenov et al. (1962); Drummond & Pines (1962)

$$\frac{\partial f}{\partial t} = \frac{4\pi^2 e^2}{m_e^2} \frac{\partial}{\partial v} \frac{W}{v} \frac{\partial f}{\partial v} \tag{1.5}$$

$$\frac{\partial W}{\partial t} = \frac{\pi \omega_{pe}}{n_e} v^2 W \frac{\partial f}{\partial v} \tag{1.6}$$

where $W(v,t)$ is the spectral energy density of Langmuir waves and $f(v,t)$ is the electron distribution function. For clarity is should be mentioned that v describes both the kinetic velocity of electrons and the phase velocity of Langmuir waves. The quasilinear equations describe the evolution of waves and particles as they exchange energy through wave-particle interactions. The quasilinear equations are a simplification from the Vlasov equation which ignores all other electromagnetic processes present in the plasma. Assumptions are also required that the Langmuir wave energy generated is not larger than the thermal energy of background plasma and that no particles are confined. Provided the perturbations created on a particle through wave-particle interactions are small (for example much less than an electron gyroradius in a gyroperiod) the quasilinear equations are valid. The growth rate of waves from wave-particle interactions is proportional (amongst other things) to $\partial f/\partial v$ (Figure 1.4). The dispersion relation for Langmuir waves is

$$\omega^2(k) = \omega_{pe}^2 + 3k^2 v_{Te}^2/2. \tag{1.7}$$

where ω_{pe} is the local plasma frequency. Velocities considered for a non-thermal electron beam are much higher than the background thermal velocity v_{Te}. Using the resonance condition, the angular frequency of Langmuir waves can be expressed as $\omega^2 = \omega_{pe}^2(1 + 3v_{Te}^2/2v^2)$. For the Langmuir waves in question $v \gg v_{Te}$ giving the approximation $\omega \approx \omega_{pe}$. The Cerenkov resonance condition can thus be written as $\omega_{pe} = kv$.

1.2.2   Quasilinear relaxation

Figure 1.4 can pictorially explain how a positive gradient in velocity space is formed but it does not show the feedback on the electrons from inducing waves. The electrons are decelerated as they transfer energy to the waves. Equation (1.5) describes this feedback whereby electron diffuse down in velocity space where the diffusion coefficient $D = W/v$.

Having a diffusion feedback on the particles causes them to spread in velocity space, removing the positive gradient. The asymptotic solution forms a plateau in velocity space such that $\partial f/\partial v = 0$ (Vedenov & Ryutov 1972; Grognard 1985). The characteristic time for quasilinear relaxation to occur can be defined as the quasilinear time $\tau_{ql} = n_e/(\pi\omega_{pe}n_b)$. An analytical solution is known (e.g. Kontar 2001d) given an initially unstable, simple electron beam in velocity space described by

$$g_0(v) = 2n_b v/v_0, \qquad v < v_0 \tag{1.8}$$

where v_0 is the maximum velocity of the electron beam. A plateau forms in the distribution function

$$f(v, t \approx \tau_{ql}) = \frac{n_b}{v_0} \tag{1.9}$$

where the Langmuir waves are described by

$$W(v, t \approx \tau_{ql}) = \frac{m_e n_b v^3}{v_0 \omega_{pe}} \int_0^v \left(1 - \frac{v_0}{n_b}g_0(v)\right) dv. \tag{1.10}$$

We used a numerical simulation, shown in Figure 1.5, to demonstrate the electron distribution function and spectral energy density of Langmuir waves at three points in time (numerical details given in Kontar 2001c). The initially unstable distribution
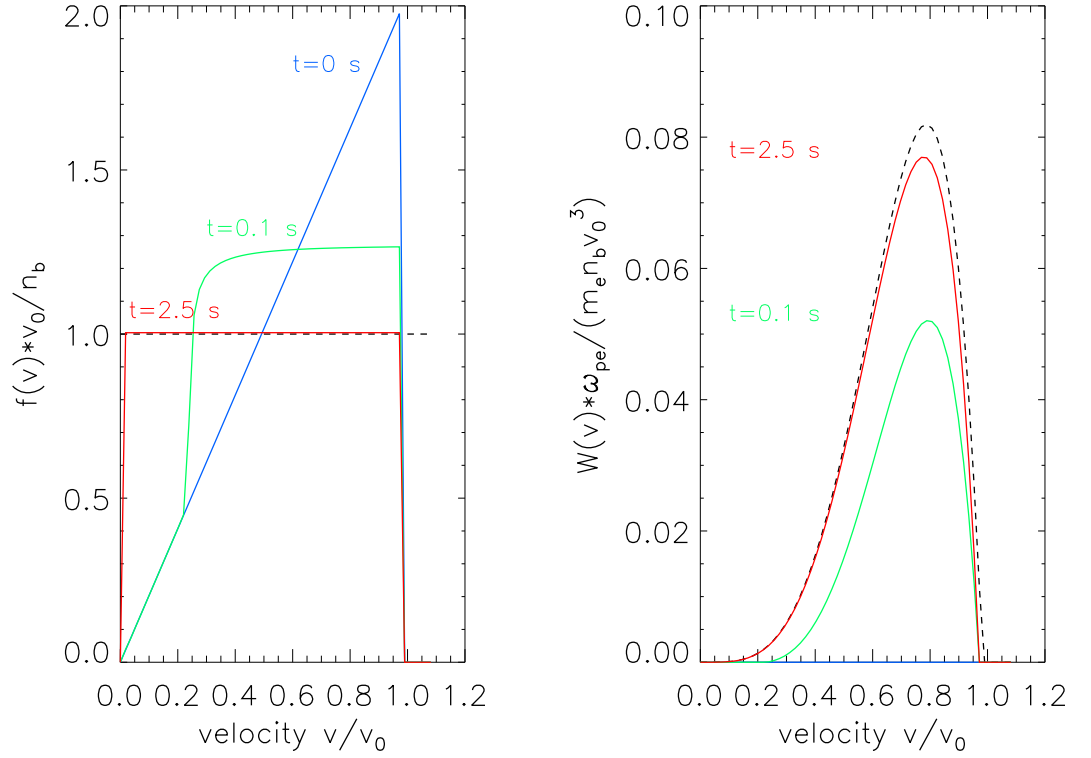
Figure 1.5: The evolution of an unstable electron beam and the corresponding generation of Langmuir waves. f and W are the normalised electron distribution function and wave spectral energy density respectively. The asymptotic solution is given by the dashed lines.

function generates a plateau in velocity space, transferring its energy to the induced Langmuir waves.

The unstable electron beam generated through propagation will behave in a similar manner. Figure 1.6 shows the asymptotic behaviour of this process for a thermal Maxwellian and non-thermal Gaussian 'beam' with density ratio $n_b/n_e = 10^{-4}$, $v_{Te} = 5.5 \times 10^8$ cm s^{-1}. The bump will form a plateau in velocity space which will over time extend all the way from the high energy electron beam to the low energy background Maxwellian plasma. The spectral energy density is also shown and can be seen to exist at larger values of $k\lambda_D$ as the resonant electrons are decelerated to lower velocities. If
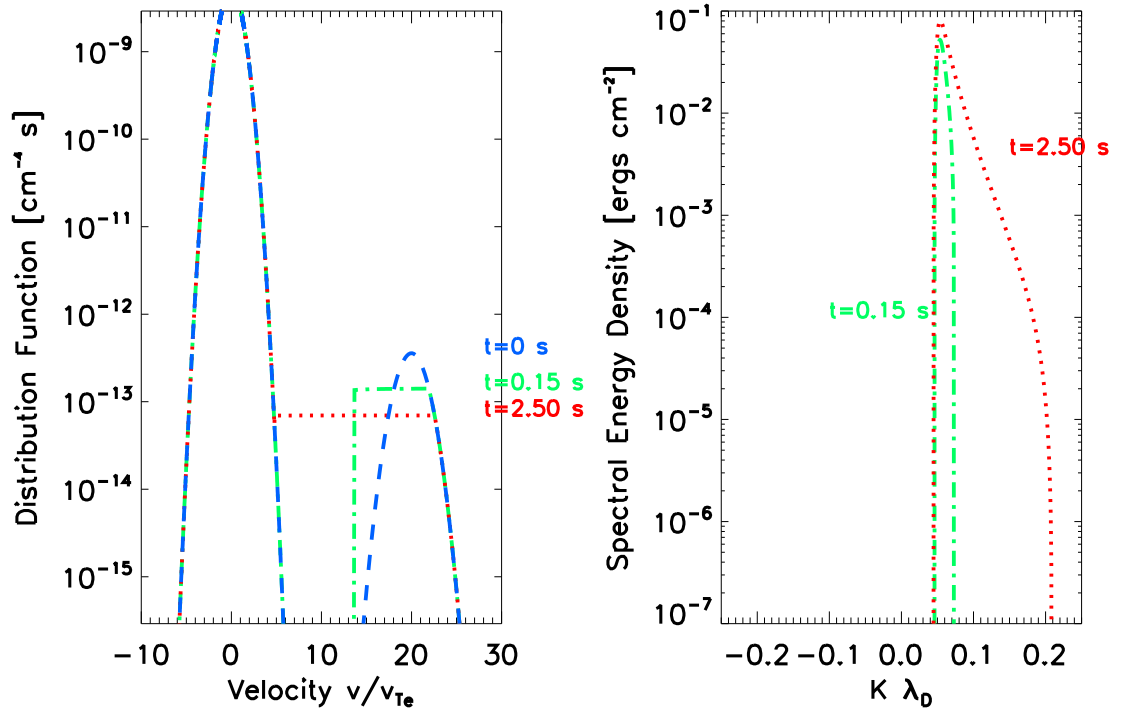
Figure 1.6: The evolution of a thermal Maxwellian and non-thermal electron beam with density ratio $n_b/n_e = 10^{-4}$, $v_{Te} = 5.5 \times 10^8$ cm s^{-1}. The bump in velocity space caused by electron beam propagation diffuses out forming a plateau.

we consider η, the ratio of Langmuir wave energy density to the kinetic energy density of the electron beam it takes the form

$$\eta \approx \frac{E_w}{0.5 n_b m_e V_b^2} \tag{1.11}$$

where E_w is the energy density of Langmuir waves. For the analytical solution we have an asymptotic limit of $\eta = 0.5$.

Figure 1.6 shows what will happen as $t \to \infty$ for a thermal Maxwellian and a non-thermal bump at 20 v/v_{Te}. It is not typical of what will happen to an electron beam as it propagates through space with time. It is likely that the high energy part of the electron beam will never relax enough to the state shown at $t = 2.5$ s because the electrons are not remaining stationary in space. The lower energy electrons may relax to the distribution function as they are closer in velocity space and as such require less

time to relax completely. Moreover an inhomogeneous background plasma can either encourage or hinder the electron beam relaxation (see Chapter 3 for more informaiton).

1.2.3 Sturrock's dilemma

In the early 60s, a problem was pointed out (Sturrock 1964) with the two-stream instability. The standard scenario models a beam of electrons at high energies and a background Maxwellian plasma at thermal energies (Figure 1.6). Considering the coronal and beam parameters $n_e = 10^8$ cm^{-3}, $\omega_{pe} = 10^9$ s^{-1}, $n_b = 10^4$ cm^{-3}, $v_b = 10^{10}$ cm s^{-1}, $\Delta v_b = 10^9$ cms^{-1}, the quasilinear growth rate is of the order of 10^{-7} s. This is much faster than the collisional time of around 10^{-2} s so collisional damping of the Langmuir waves would be ineffectual at inhibiting the instability. Sturrock goes on to estimate that without anything stopping the instability the beam would lose all its energy to Langmuir waves in a few metres. This is a serious problem in the theory as beams of electrons are observed to travel distances ≥ 1 AU.

The initial argument put forward by Sturrock was slightly reformulated by Melrose (1980c) to be independent of the poorly known parameters of the accelerated electron beam. Melrose considers η, the ratio of Langmuir wave energy density to the kinetic energy density of the electron beam as defined above. If the asymptotic quasilinear solution is approached the energy in the stream would decrease exponentially in time. This would cause the beam to lose all of its energy in a very short space of time. To avoid this outcome Melrose argues that $\eta \ll 0.5$ resulting in the beam losing much less energy to Langmuir waves.

The idea proposed by Sturrock to overcome this dilemma was to suppress the level of Langmuir waves via non-linear mechanisms. Langmuir waves can scatter off ions which builds up a secondary stream of Langmuir waves. Langmuir waves are removed from resonance with the electron beam which eventually suppresses wave growth. Another way that Langmuir waves can be removed from resonance with the electron beam is the scattering of Langmuir waves off density inhomogeneities. This could achieve inhibition of waves such that $E_w \ll 0.5 n_b m_e V_b^2$. Simulations taking into account the scattering

of Langmuir waves have been carried out in this thesis, however, they do not appear to be the primary mechanism for overcoming Sturrock's dilemma. Simulations which deal with density fluctuations are explicitly covered in Chapter 3.

1.2.4   Beam-plasma interaction

Another idea which solves the Sturrock dilemma is the formation of a beam-plasma structure where the electron beam and Langmuir waves exist in a state of quasi-stability. That this could happen has been observed analytically by Zheleznyakov & Zaitsev (1970) and further developed by Zaitsev et al. (1972) who also considered the relativistic equations. The problem was initally worked on numerically by Takakura & Shibahashi (1976); Magelssen & Smith (1977); Grognard (1985). The main idea of the beam-plasma structure consists of electrons generating Langmuir waves at the front of the beam through the usual instability $\partial f/\partial v > 0$. The induced waves are then reabsorbed in the back of the beam where $\partial f/\partial v < 0$. Electrons are able to restore their energy which had been transfered to the Langmuir waves. The electron beam is thus able to retain its energy over the long distances > 1 AU.

Starting off with a stable electron beam where $\partial f/\partial v < 0$ at all places in phase space, the electron beam is allowed to propagate through space. The different velocities of the electrons cause them to move at different speeds. Faster electrons outpace slower electrons, Langmuir waves are induced at the front of the beam, and a plateau is formed in velocity space much like that described above. What is important to the theory is that the electrons are still at different energies which will cause faster electrons to outpace the slower electrons again. This creates a beam-plasma structure that travels at a constant velocity equal to the mean velocity of the electrons which are taking part in this structure. The beam-plasma structure is able to travel through a background plasma without any energy losses if you only consider spatial transport and the quasilinear equations.
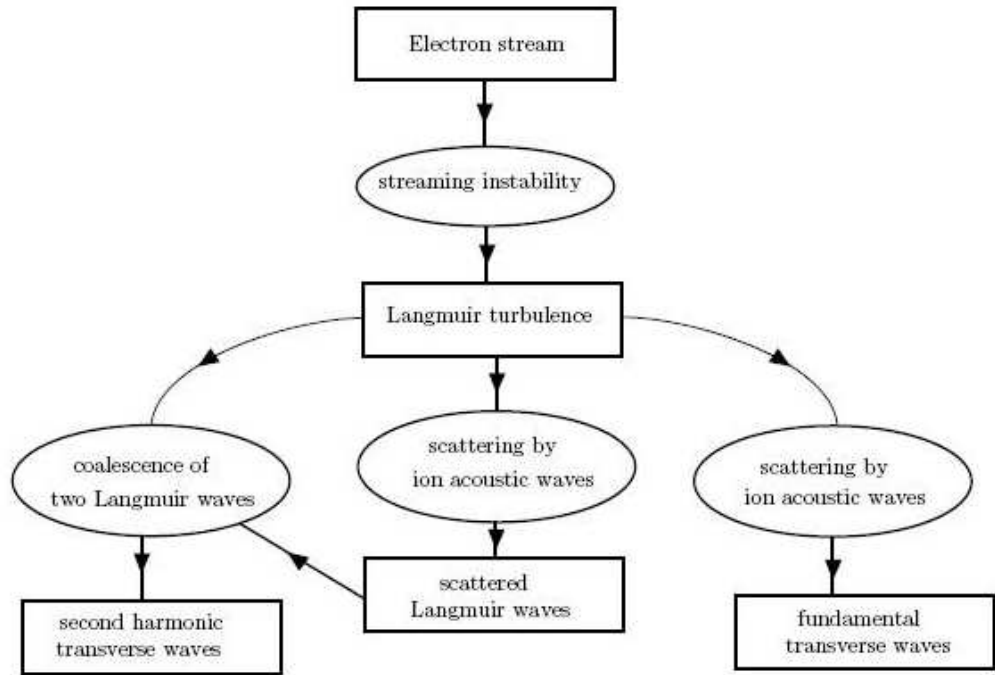
Figure 1.7: A flow diagram indicating the stages in plasma emission in an updated version on the original theory (Melrose 2009).

1.3   Wave-wave interactions

Electron beams propagating as a beam-plasma structure travel with a given distribution of Langmuir waves. Langmuir waves are susceptible to wave-wave processes which can create different types of waves. The most observable waves which can be produced are transverse electromagnetic waves. Radiation is emitted at either the local plasma frequency ('fundamental') or at twice the local plasma frequency ('harmonic'). An overview of the dominant processes is shown in Figure 1.7. The amount of energy converted to transverse waves is very small and as such the local distribution of Langmuir waves can be considered to be unaffected by these processes. They are an important diagnostic tool for the evolution of an electron beam.

The conversion of Langmuir waves into electromagnetic emission is important to explain the coherent radio emission observed from the Sun. It is not, however, the focus of this work. The main processes are presented here to give the reader a complete

picture from electron beam to Langmuir wave to radio wave. A detailed description of the processes can be found in Melrose (1980b,c, 1985) and Benz (2002). In the description we are assuming weak turbulence, which is valid provided the level of Langmuir waves is not too intense.

1.3.1 First harmonic emission

The two main processes to explain fundamental emission are:

- Scattering of Langmuir waves off thermal ions, denoted $l \rightarrow t$.

- The coalescence and decay of Langmuir waves with ion sound waves, denoted $l + s \rightarrow t$, $l \rightarrow s + t$.

The scattering of Langmuir waves off thermal ions is similar to Thomson scattering. It is not a single electron which scatters the wave but the Debye shielding cloud of electrons which accompanies an ion. With first harmonic emission, we observe transverse wave frequencies that are at the local plasma frequency requiring $\omega_t \approx \omega_l$. For a wave scattering off a thermal ion with velocity v_{Ti}, the incident Langmuir wave and induced transverse wave will have frequencies and wave vectors ω_l, $\mathbf{k_l}$ and ω_t, $\boldsymbol{k_t}$ related by

$$\omega_l - \mathbf{k_l} v_{Ti} = \omega_t - \mathbf{k_t} v_{Ti} \qquad (1.12)$$

due to the conservation of momentum and energy. Given the small magnitude of fundamental transverse wave vectors $\boldsymbol{k_t}$ this leads to $\Delta\omega \approx \mathbf{k_l} v_{Ti} \approx \omega_{pe} v_{Ti}/v_b$, where v_b is the inducing electron beam velocity and v_{Ti}/v_b is typically around 10^{-3}. The ion velocity is considered unaltered as $k_b T_i \gg \hbar \omega_l$.

In Thomson scattering, the rate at which the energy density W_t of transverse waves is generated from the incident transverse waves W_t' in a vacuum is $\frac{dW_t}{dt} = \sigma_T n_e c W_t'$ where $\sigma_T = 8\pi r_e^2/3$ is the Thomson scattering cross section and r_e is the classical electron radius. The only modification this requires for Langmuir waves (with energy density W) in a plasma generating transverse waves is that the power radiated is proportional to the refractive index $\xi(\omega) = (1 - \omega_{pe}^2/\omega^2)^{0.5}$ and that the cross-section

$\sigma_i = \sigma_T/4$ (see Melrose 1980b,c, for a complete description) giving

$$\frac{dW_t}{dt} = \xi(\omega)\sigma_i n_e c W. \tag{1.13}$$

For reasonable coronal and inner heliosphere parameters this rate is very small with W_t reaching only $10^{-10}W$ over a distance of 10^7 cm.

It is possible to increase the rate via the process of induced scattering. The emitted transverse waves can stimulate the ions which greatly amplifies the rate of scattering. As the process is then proportional to both the Langmuir and transverse wave energy density this can lead to exponential growth. Induced scattering becomes important when the effective temperature of transverse waves T_t reaches a threshold brightness temperature of $T_i v_b/v_{Ti}$. The threshold is roughly 10^8 K in the solar corona, well within the observed brightness temperatures of coherent radio emission (see Section 1.4).

The second process to generate transverse waves involves the coalescence or decay of Langmuir waves with ion sound waves. In this scenario the parametric conditions are

$$\omega_1 + \omega_2 = \omega_3 \tag{1.14}$$

$$\mathbf{k_1} + \mathbf{k_2} = \mathbf{k_3}. \tag{1.15}$$

An important consequence of Equation (1.15) is that the ion sound wave will have a wave vector $\boldsymbol{k_s} \approx \pm \boldsymbol{k_l}$. This condition rules out MHD waves and non-thermal whistler waves from the process of generating transverse waves from Langmuir waves as their wave vector is not large enough to satisfy Equation (1.15). The coalescence of $l + s = t$ describes local plasma turbulence greatly enhancing the scattering process of Langmuir waves with ions. The rate of conversion is increased by a factor of T_s/T_e where T_s is the effective temperature of ion sound waves. For ion sound waves, T_s is much larger than T_e leading to a huge increase in transverse waves. Saturation of the process thus becomes important, occurring when $T_t = T_l$. The process is much more efficient than induced scattering of ions to explain radio emission with high brightness temperatures. It runs into difficulties when plasma conditions lead to strong ion sound wave damping around $T_e \leq T_i$. A typical observed ratio of $T_e/T_i = 2.8$ in the solar wind at 1 AU

(Lin et al. 1986) would permit this. Heating of the electrons during solar flares is a possible example when emission via ion sound waves may be taking place in the corona.

1.3.2 Second harmonic emission

The production of second harmonic emission is better understood. From the parametric conditions (1.14), (1.15) the only process that can produce waves at $2\omega_{pe}$ is the coalescence of two nearly oppositely directed Langmuir waves $l + l' = t$. They are required to be nearly in opposite directions to produce a transverse wave with small $\boldsymbol{k}$. Langmuir waves in the backward direction can be created by reflection off positive background electron density gradients. The analogy with Thomson scattering can be continued to find the growth rate of transverse waves. The cross section for this scattering $\sigma_l = \sigma_T/5$ and the rate is given by (Melrose 1985)

$$\frac{dW_t}{dt} = \frac{6}{5}\sigma_T n_e W \xi(\omega) c \frac{T_{l'}}{m_e c^2} \tag{1.16}$$

The rate is large enough to explain the observed spectra of second harmonic emission from radio bursts. The saturation of this process occurs when the brightness temperature of the transverse waves reaches

$$T_{max} = 2\frac{T_l T_{l'}}{T_l + T_{l'}} \tag{1.17}$$

where the 2 arises from the frequency $2\omega_{pe}$. Langmuir waves travelling in the opposite direction will have a smaller temperature producing saturation of this process at $T_t = 2T_{l'}$. The observation of two bands of coherent radio emission with frequency ratio nearly 1:2 confirms the general idea about second harmonic emission.

1.4 Solar radio bursts

1.4.1 Overview of radio bursts

The first and second harmonic emission induced by Langmuir waves which, in turn, were induced by electron beams are observed both in-situ by spacecraft and remotely by
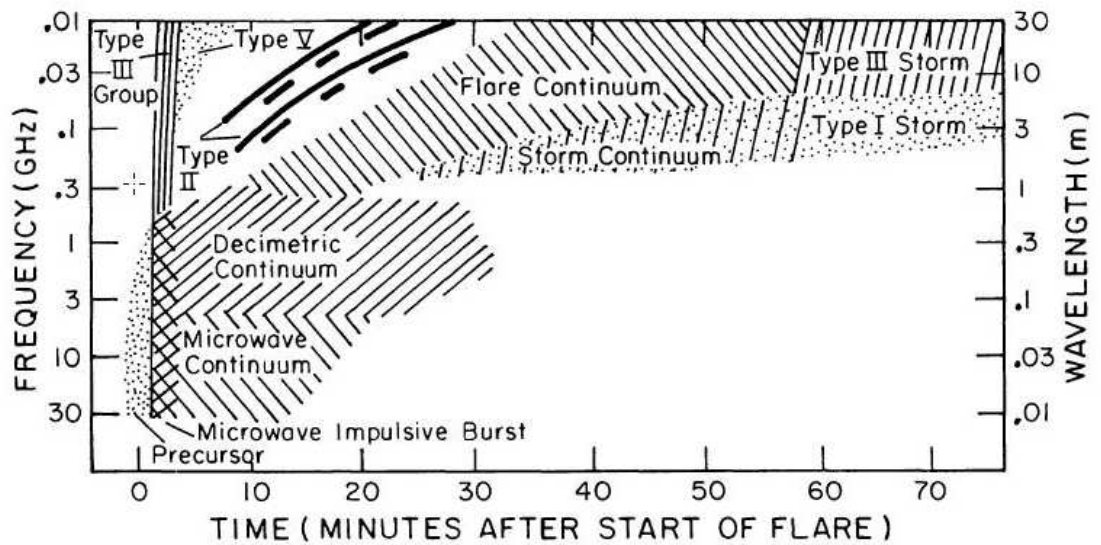
Figure 1.8: Schematic dynamic spectrum of a solar radio outburst such as might be produced by a large flare. Outbursts often vary considerably from this 'typical spectrum' (Dulk 1985)

ground based observatories. Being at the local plasma frequency the electromagnetic emission occurs at radio wavelengths ranging from GHz deep in the solar atmosphere to kHz near the Earth. Due to the discrete or impulsive nature of electron beams, the radio emission is referred to as bursts.

Radio bursts come in a variety of forms and are differentiated through how their frequency changes in time, known as their frequency drift rate or drift frequency. Initially three types of radio emission were classified as type I, II and III in order of ascending drift frequency (Wild & McCready 1950). Later it became necessary to introduce two more types IV and V. Each type has subtypes that further describe the array of complex behaviour these radio bursts display. Figure 1.8 shows an overview of the many different types of radio bursts which can occur in a large flare.

There are a number of different reviews (e.g. Dulk 1985; Bastian et al. 1998; Nindos et al. 2008) that cover radio bursts including their properties. For the analysis of electron beams these properties are part of the key to understanding electron propagation dy-

namics. As the generation of coherent radio bursts is a two-stage process it is very hard to infer the properties of the initial electron beam from the radio emission. To gain further understanding of coherent emission, computer simulations have been created to replicate electron beam propagation (e.g. Grognard 1985; Kontar 2001a). The focus of electron beam simulations has generally been to understand the behaviour of the electron beam when it induces Langmuir waves and how both these interact with the background plasma density.

Coherent radio emission is a powerful diagnostic tool for electron beam propagation. As the electron beam propagates through the heliosphere, it encounters a changing background electron density. With induced Langmuir waves being at the local plasma frequency, the coherent emission effectively tracks the transport of the electron beam across the heliosphere. By understanding how the properties of radio bursts are linked to the Langmuir waves which induce them we can further diagnose how high energy electron beams vary during their transport. Radio bursts are thus one of the best ways we can infer properties of the electron beam near the Sun.

Radio spectrographs are used to image large bands of radio frequencies to illustrate the spectral analysis of radio bursts. There are enough radio spectrographs to get a complete picture of any individual burst from GHz to kHz if the burst extends that far. Of note are the Phoenix-2 radiospectrometer (Messmer et al. 1999) in the range 0.1 to 4 GHz, the ARTEMIS radiospectrometer (Maroulis et al. 1993) in the range 90-30 MHz and the WAVES instrument (Bougeret et al. 1995) which can detect the frequency range 14 MHz-20 kHz. The radio spectrographs create dynamic spectra, similar to Figure 1.8 where the intensity of the radio source is given by the colour of the contours, creating a three dimensional representation of intensity vs frequency vs time.

Radioheliographs are used to generate a two-dimensional image of the radio burst at discrete frequencies. Of these the Nançay Radioheliograph (NRH) (Kerdraon & Delouis 1997) is able to image within the range 432 - 164 MHz. Radioheliographs are particularly useful as they allow not only the position of the radio burst to be ascertained but also their position with respect to other emission.
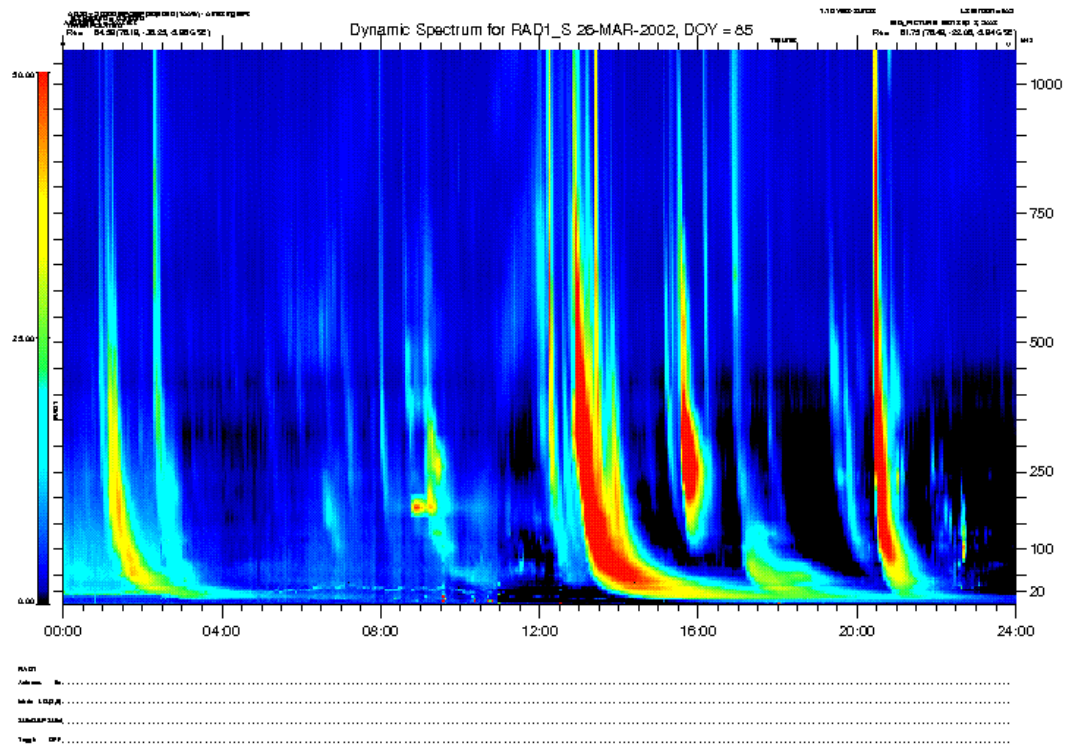
Figure 1.9: A daily plot using the RAD1 instrument on the WAVES experiment on-board the WIND spacecraft (from the WAVES website). A series of type III radio bursts are shown from 1 MHz down to 20 kHz. Note the decreasing drift frequency of the radio emission.

1.4.2 Type III emission

The most widely studied yet not completely understood radio bursts are type III radio bursts. Electrons originating high in the solar atmosphere can propagate along the interplanetary magnetic field lines of the Parker spiral towards the Earth. These electrons, travelling at velocities around one third of the speed of light, become unstable and create Langmuir waves. It is these Langmuir waves which are partially transformed into radio emission at the plasma frequency f_{pe} or its second harmonic $2f_{pe}$ via non-linear plasma processes (Melrose 1990). An example of a series of type III bursts is given in Figure 1.9.

Drift frequency

Type III bursts have a wide range of properties that distinguish them from other radio bursts. The first property is their high drift rate df/dt. Type III bursts have a rough frequency range from around 700 MHz to 20 KHz, representing propagation from the low corona to the Earth, although they are known to propagate further into the heliosphere. Type III bursts have been reported to drift at a rate of $df/dt = -0.01f^{1.84}$ MHz s^{-1} derived from a least squares fit to reports by various authors in the frequency range 550 MHz to 74 kHz (Alvarez & Haddock 1973). The drift rate can be then used to deduce the exiter speed by assuming the electron density structure in the corona/heliosphere. Alvarez & Haddock (1973) derived exciter speeds within the range 0.2 c $\leq v_b \leq 0.8$ c. Specifically in the corona, the drift rate has been found to vary as $df/dt = -0.2f$ (Melrose 1980c). For the electron beam the drift rate represents the mean speed of the electron beam-plasma structure as it propagates from the Sun to the Earth. As we shall see in Chapter 3 the energies of electrons participating in this structure are radially dependent with the maximum energy decreasing over time. The beam-plasma structure thus decelerates with distance from the Sun. Another factor that determines the drift frequency is the radial decrease of plasma density from the Sun to the Earth. The decrease can be approximated by two power-laws with a break from high to low spectral index around 9 R_s. Both these conditions give rise to the observed frequency drift rate and will be discussed in a later chapter.

Reverse drift type III

Type III bursts with a positive drift rate are observed in the low corona. These are generally associated with downward propagating electron beams, often responsible for HXR emission in the chromosphere (e.g. Aschwanden et al. 1995a). In a positive density gradient a lower level of Langmuir waves are induced by an electron beam (e.g. Kontar 2001b). Recent work has been done to simulate these electron beams (Hannah et al. 2009) showing substantial Langmuir wave growth for the large beam densities predicted from HXR observations.

Source size

The size of Type III bursts increases with decreasing frequency. Measurements at various frequencies for a variety of bursts give averages (half widths to 1/e brightness) of 5 arcmin at 169 MHz (Bougeret et al. 1970), 11 arcmin at 80 MHz, 20 arcmin at 43 MHz (Dulk & Suzuki 1980), 5 degrees at 1 MHz, 50 degrees at 100 KHz (Steinberg et al. 1985) and 1 AU at 10 KHz (1 AU) (Lin et al. 1973). A comprehensive study of type III radio source sizes is undertaken by Steinberg et al. (1985) who deduces an f^{-1} variation of source angular size with observing frequency. This is directly proportional to the distance from the Sun implying expansion in a fixed cone of 80° with the apex in the active region. They also extend the standard scattering model to deduce that interplanetary density inhomogeneity roughly doubles the source size as observed at 1 AU. An electron beam would thus leave the corona and expand in a cone of angle roughly 40° from the active region.

Frequency range

Many type III bursts do not make it out of the corona. These type III bursts usually consist of a small group between 1 and 10 individual bursts. Their lack of propagation could be due to a variety of different beam properties which control the generation of Langmuir waves or it could be to do with the properties of the background coronal plasma such as the magnetic field configuration confining the electron beam to the corona. Some type III radio bursts do make it out into the heliosphere and are labelled interplanetary (IP) type III bursts. The point where corona ends and the inner heliosphere starts is subjective. Bursts are commonly called IP if they are detected by the WAVES experiment at around 10 MHz. IP bursts are generally a collection of many small bursts observed in the high corona which merge into one observable burst because the background density gradient decreases.

Rise and decay of bursts

The rise and decay of type III radio emission in the interplanetary medium generally takes the form of a Gaussian total rise time t_e followed by a power-law e-folding decay time t_d. The general trend in emission is a shorter rise time $t_e < t_d$. A statistical study of rise and decay time between 2.8 MHz and 67 kHz was undertaken by Evans et al. (1973). The study found with a least squares fit through the data the relations $t_e = 4.0 \times 10^8 f^{-1.08}$ and $t_d = 2.0 \times 10^8 f^{-1.09}$ where t is in seconds and f is in Hz. The power-law form of the decay time is currently unexplained as collisional damping of Langmuir waves would lead to a much longer decay time. There must be another process which accounts for either the spatial damping of Langmuir waves or the suppression of Langmuir waves inducing electromagnetic emission.

Harmonic Structure

Both fundamental (F) and second harmonic (H) emission are exhibited in a significant proportion of type III radio bursts. The H-F ratio, naively expected to be 2:1, actually ranges from 1.6:1 to 2:1 with a mean near 1.8:1 (Wild et al. 1954a; Stewart 1974). To explain this it has been suggested that F emission near the local plasma frequency is not able to escape and be observed (e.g. Suzuki & Dulk 1985). At frequencies > 100 MHz the H emission is usually detected whilst in the interplanetary medium between 1 and 100 MHz a significant portion of type III bursts are detected with harmonic structure (both F and H emission) (e.g. Wild et al. 1954a; Stewart 1974; Dulk & Suzuki 1980; Suzuki & Dulk 1985; Robinson & Cairns 1994, 1998). F emission is observed to be more common and intense at larger distances from the Sun leading to the general condition that H emission dominates close to the Sun while F emission dominates further away (Robinson & Cairns 1994; Dulk et al. 1998). Generated distributions of Langmuir waves via simulations can possibly shed some light on this.

Brightness temperature

The brightness temperature of emission can be used to categorise emission as thermal, incoherent or coherent with the latter having very high T_b. In brief the observed brightness temperature is the temperature at which a thermal source would need to be to produce the observed emission. The very high brightness temperatures observed confirms that emission processes are coherent. For type III radio bursts T_b usually lies within the range 10^8 and 10^{12} K although it can rise to 10^{16} K (Suzuki & Dulk 1985). The trend for T_b is to increase with decreasing frequency up to around 1 MHz and then either decreases or remains constant (Dulk et al. 1984). There is also a weak anti-correlation between rise times and T_b. Fundamental type III emission is also thought to produce higher T_b than harmonic emission (Dulk et al. 1984; Melrose 1989). It should also be possible to estimate the maximum value of T_b from T_l, the temperature of the inducing Langmuir waves (Melrose 1989) but to do so requires the k-space spectrum of the Langmuir waves. Observational constraints of T_b can thus help in the diagnosis of electron beam simulations.

Polarization

If either x-mode or o-mode electromagnetic waves dominate, the observed radiation is said to be polarized. The polarization of type III emission is weakly circularly polarized with H emission having less polarization than F emission (e.g. McLean 1971; Suzuki & Sheridan 1977; Dulk & Suzuki 1980; Suzuki & Dulk 1985). Dulk & Suzuki (1980) made a thorough analysis of polarization characteristics of 997 bursts finding the average polarisation of F-H pairs were 0.35 and 0.11 respectively while structureless bursts had only a polarization of 0.06. The maximum F polarization was around 0.6. Most of the observed emission is in the o-mode creating the severe restriction on the inducing Langmuir waves that their wave vector must be within 20° of the magnetic field direction (Melrose et al. 1978). Emitted linearly polarized waves tend to be obliterated over any finite band of frequencies by differential Faraday rotation of the plane of polarization during passage through the heliosphere (e.g. Suzuki & Dulk

1985).

Type IIIb bursts

The presence of fine structure in a type III dynamic spectra is classed under the envelope of type IIIb burst. These bursts show a clumpy nature to their emission, usually shown in the F emission. Fine structure in the H component in type IIIb bursts is very rarely observed (Dulk & Suzuki 1980). Ellis & McCulloch (1967) and Ellis (1969) used a particularly fast response radiospectrograph within the range 25-100 MHz which found these bursts only below 60 MHz. de La Noe & Boischot (1972) found the type IIIb bursts preceded type III bursts in 30 % of cases and was from the same spatial location. The common belief (Smith & Riddle 1975; Melrose 1980c, 1983) is that density inhomogeneities in the background plasma which create a clumpy distribution of Langmuir waves are the cause of this fine structure. If density inhomogeneity is responsible for type IIIb bursts, the turbulent intensity may be less close to the Sun at frequencies > 60 MHz. The topic of density inhomogeneities and Langmuir waves are dealt with in Chapter 3.

Inverted U and J bursts

The frequency drift rate of radio bursts has been observed to change sign during a normal type III burst, taking the shape of an inverted U or J (Maxwell & Swarup 1958). These bursts are believed to be electron streams travelling along magnetic fields confined to the corona. For the J bursts, the radio emission stops when the electron beam reverses direction but with U bursts it continues to higher frequencies. The rate of occurrence is very low and they generally occur in H emission within the range 20-300 MHz, although F emission has been observed (e.g. Labrum & Stewart 1970; Aurass & Klein 1997, and references therein). Their polarization is usually below 10 %, agreeing with the properties of H emission. Similar to reverse drift bursts their low occurrence could be to do with increased difficulties to generate Langmuir waves in an increasing density gradient.

1.4.3 Type V emission

Closely related to the type III burst are type V bursts classified due to their long durations (minutes) and wide spectra (Wild et al. 1959). The type V emission appears as a continuation of a type III burst in the dynamic spectra (Figure 1.10). Type V bursts are important because their explanation has to be consistent with any model of type III bursts. Type V bursts appear at low frequencies below 120 MHz and generally have 1-3 minute durations (Dulk et al. 1980). The size of type V bursts increases rapidly with decreasing frequency, with full width at 1/e brightness on average 105 arcmins^2 at 80 MHz and 300 arcmins^2 at 43 MHz (Robinson 1977) similar to type III bursts (Dulk & Suzuki 1980). Type V bursts have also been observed to move relative to the disk surface at speeds ≈ 2 Mm s^{-1} (Weiss & Stewart 1965). A similar problem related to the decay of type V emission exists where the characteristic time of collisional damping of Langmuir waves is much larger than the lifetime of type V emission.

Possibly the most defining observations of type V emission are in their polarization. Their polarizations are low (usually < 0.07 %) which suggests H emission. However, it is common to find their polarization opposite in the sense of the corresponding type III (Dulk et al. 1980). Dulk et al. (1980) suggest the most likely reason for this change is due to x-mode rather than o-mode emission. This could be caused by increased isotropy in the Langmuir wave distribution as the condition for o-mode emission is Langmuir waves within 20° of the magnetic field.

Another deviation of type V emission from their associated type III emission is the occurrence of large position differences, sometimes up to 1 R_s (Weiss & Stewart 1965; Robinson 1977). This is not always observed and the positions of the type III and V can overlap or only be slightly displaced. Some explanations of this phenomenon are low energy electrons travelling along different magnetic field lines or a variation of the beaming of emission changes the position of the centroids (Dulk et al. 1980).
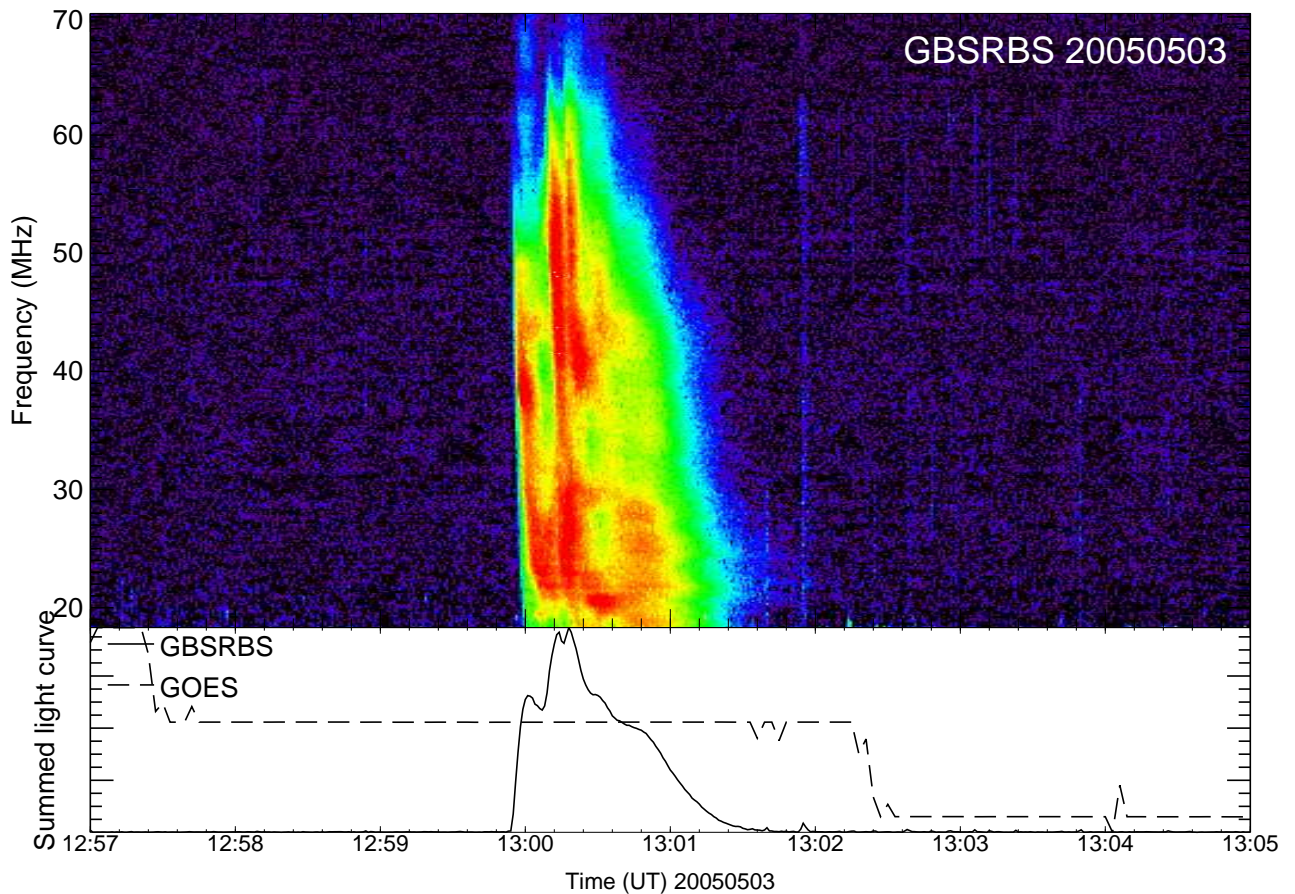
Figure 1.10: An example of a type III/V emission obtained from the Green Bank Solar Radio Burst Spectrometer (from the GBSRBS website). Note the extended duration of the type V emission.

1.4.4   Type II emission

Type II emission, categorised for its slower drift frequency than type III, is associated with the passage of a shock front through the corona (Wild et al. 1954b). This shock front was later described as a collisionless MHD shock (Uchida 1960; Wild 1962). The collisionless shock related to type II emission is believed to be driven by coronal mass ejections (CMEs) (e.g. Gopalswamy et al. 2005; Liu et al. 2009; Gopalswamy et al. 2009). An example of a type II dynamic spectra can be seen in Figure 1.11. A popular electron acceleration method responsible for type II emission is diffusive shock acceleration (electrons receiving one energy gaining reflection) (e.g. Holman & Pesses
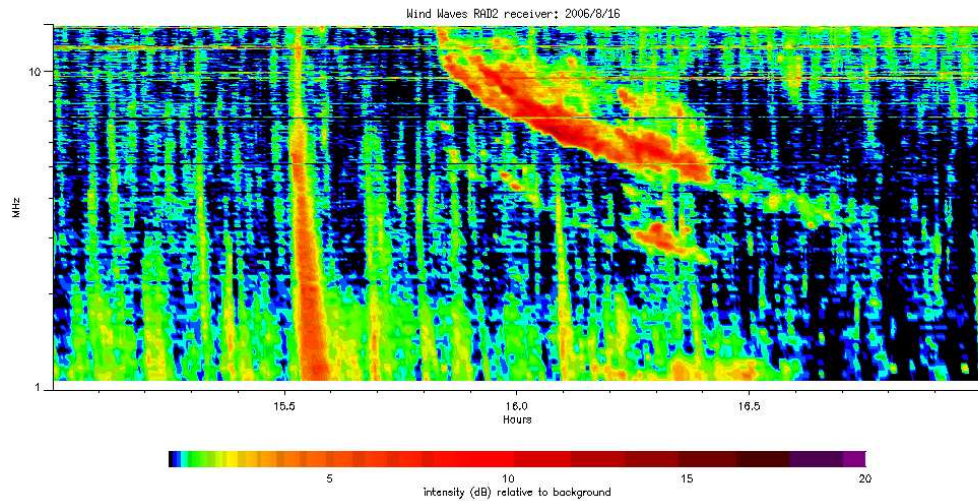
Figure 1.11: An example of a type II and some type III bursts obtained using the RAD2 instrument from the WAVES experiment on board the WIND spacecraft (from the WAVES website). The type II burst (right) has a much slower drift rate and the faint fundamental emission can also be observed.

1983). This process requires a seed population of high energy electrons whose origin is not yet explained. Type II bursts are particularly useful as they provide early warning of interplanetary shocks, which can cause electromagnetic disturbances at the Earth.

Observations of the type II frequency range and the associated CMEs can give insight into requirements for type II generation. The typical type II frequency range is from 150 MHz down to around 20 MHz although type II bursts can be observed with higher starting frequencies and at lower frequencies down to the kHz range. This leads to three different classes of type II event based on their wavelength extent (not their frequency), denoted metric, decahectometric (DH) and kilometric. Kilometric emission is always observed with an interplanetary shock (Cane et al. 1987) which is nearly always associated with a CME (Sheeley et al. 1985). DH emission is generally observed with an interplanetary shock (e.g. Gopalswamy et al. 2000), however not all metric emission is associated with CME driven shocks (Sheeley et al. 1984). Sheeley et al.

(1984) mentions the possibility of some metric type IIs being associated with blast waves from flare activity. A statistical study by Gopalswamy et al. (2005) finds that CME kinetic energy is closely tied to the probability of occurrence of type II bursts in different frequency bands. Lower energy CMEs generally have type II emission confined to the metric range or no type II emission at all. Higher energy CMEs are more likely to produce DH or kilometric emission while the highest energy CMEs are more likely to produce type II emission which spans the entire frequency range from metric to kilometric (see also Gopalswamy et al. 2010). Whilst providing key prediction information regarding the strength of interplanetary shocks, this observation indicates the increase in energy required from the CME to drive lower frequency radio emission. The requirement of increased kinetic energy could be related to the increased difficulty from CME rarefication as it expands into the heliosphere. This result is complemented by the increased source size of type II emission at lower frequencies (Nelson & Melrose 1985).

Type II emission is generally seen 5-20 mins after flare onset and can last from between 2-15 mins. The drift frequency of type II emission is around 1 MHz s^{-1} and together with the normal coronal density maps gives velocities between 0.2-2 Mm s^{-1}. Type II emission has both a fundamental and a harmonic component although sometimes the fundamental is not observed. The type II emission has some subclasses corresponding to their dynamic spectra characteristics which include band splitting (doubling of the bands), herringbone structure (rapidly drifting, short duration substructure) and multiple lanes (believed to be caused by simultaneous shocks close by) (Nelson & Melrose 1985). The fast drift rate in the herringbone structure points to a source common to type III emission. This is further backed up by the high polarisation rate (up to 70%) which is not normally observed in type II emission but is observed in fundamental type III emission. It is also believed that the type III like (herringbone) emission is closely associated with strong density inhomogeneity (e.g. Chernov et al. 2007).
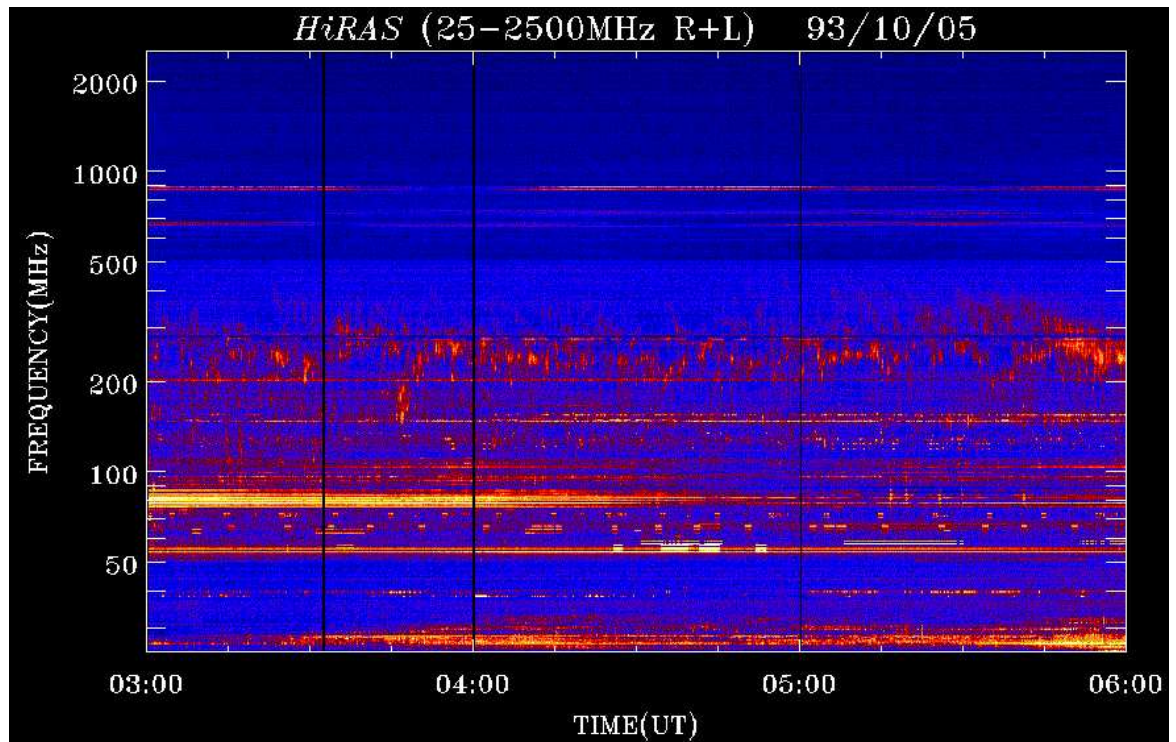
Figure 1.12: An example of a storm type I burst observed with the HiRAS Radio Telescope in Japan (from the HiRAS website).

1.4.5 Type I emission

The burst with the smallest drift frequency, known as a type I burst, takes place in the middle corona (McCready et al. 1947). It is a short, narrow band radio burst which generally occurs in large groups known as type I storms that can last for many hours (Figure 1.12). Type I bursts occur in the metric wavelength range between 30-400 MHz.

The production of type I emission is believed to be related to coalescence of Langmuir waves with ion sound waves (Melrose 1980a). Energetic electrons trapped inside active region magnetic fields confined to the corona produce Langmuir waves through the usual instability. These Langmuir waves then coalesce with ion sound waves, possibly produced through local plasma density turbulence. It is thus possible that the bursty emission is a direct signature of the stochastic nature of either the electron acceleration (e.g. Bárta & Karlický 2001; Sundaram & Subramanian 2005) or the excitation

of ion sound waves.

Type I emission has virtually no drift rate, lasting on average between 0.2 s at 400 MHz and 0.7 s at 100 MHz (Kai et al. 1985). If the drift rate is observable it can be either positive or negative implying that both upward and downward travelling electron beams are responsible. When type I emission is chained together as a storm, it can have a drift rate $> \pm 0.5$ MHz s^{-1} which is smaller than type II drift rates. Possibly the most distinctive property of type I emission is the near 100 % circular polarisation associated with fundamental emission. Why harmonic emission is not generally observed in type I bursts is as yet unknown but must be related to their height and production mechanism.

1.4.6   Type IV emission

Type IV emission (Boischot 1957) is flare-associated by definition, with large spectral width (long period) in the centimeter/decameter wavelength range. Type IV emission can be generally split into two categories, moving type IV and stationary continuum. The moving category (IVM) is believed to be caused by gyrosynchrotron emission and as such is not the focus of this subsection. The stationary continuum type IV (Figure 1.13) comes in two varieties, flare continuum (FC) and storm continuum (SC) (Robinson 1985; Pick 1986). Type IV emission is believed to be caused by electrons trapped in magnetic loops rather than propagating electron streams associated with type III bursts.

FC emission starts in the impulsive phase of solar flares and can have a type III burst as a precursor[8]. It closely resembles type V emission (e.g. Gopalswamy & Kundu 1987) but lasts much longer (10 mins to an hour) and has a strong correlation with microwave emission, with the microwave emission sometimes being called the high frequency part of FC emission. FC has low polarization indicative of second harmonic emission. FC emission can also precede IVM or SC emission. The emission process

---

[8]There is contention in the literature regarding the name of this emission, being called sometimes Part A, FCE, FCM, IVmF and other names (see Robinson 1985; Pick 1986, for a further discussion).
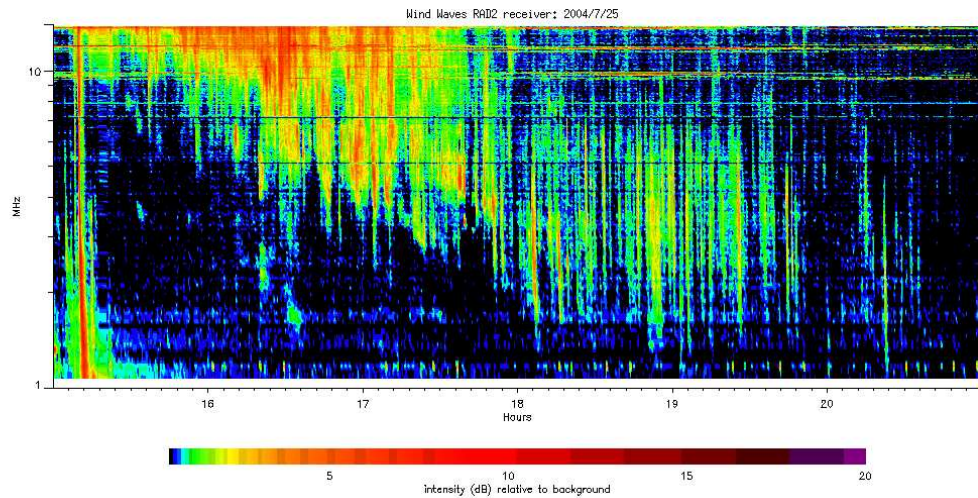
Figure 1.13: An example of a type IV burst obtained using the RAD2 instrument from the WAVES experiment on board the WIND spacecraft (from the WAVES website). The type IV burst shows a lot of fine structure.

is believed to be magnetically trapped electrons, however, observed low polarization points to either unfavourable conditions for ion sound waves to generate fundamental emission or a very weak fundamental component that is not observed.

SC emission occurs at slightly higher frequencies than FC emission and can last longer than FC emission (a few hours). It is associated (commonly near the start) with type II emission and can be a precursor to type I emission. There is some debate as to the name of this emission, with possible subclasses of this emission existing as IVmB, FCII, DCIM (see Robinson 1985; Pick 1986; Gopalswamy & Kundu 1987; Benz et al. 2006, for more info). The literature generally uses the term storm continuum when the emission lasts for many hours. All these emission types frequently show fine structure (e.g. Aurass et al. 2003; Melnik et al. 2010) indicating the presence of background plasma turbulence and/or MHD loop oscillations (Zlotnik et al. 2003). This is strengthened by the association of type II bursts and its inducing MHD shock. SC emission generally has a lower polarization than type I emission, with this quantity

being the main difference between these two types.

Chapter 2

Interplanetary solar electron beams

2.1 Introduction

Solar flare accelerated interplanetary electron beams present an alternative to the more traditional hard X-ray diagnostics of the poorly understood acceleration and transport of solar energetic electrons. While hard X-ray observations provide insight into energetic electrons in the lower dense solar atmosphere (e.g. Arnoldy et al. 1968; Dennis & Schwartz 1989; Brown & Kontar 2005), impulsive solar electron events (e.g. Lin 1985; Krucker et al. 2007) provide crucial information about escaping electrons from the acceleration region. High energy solar electrons propagate outward through the almost collisionless plasma of the solar corona and solar wind (Lin 1985). Even with this collisionless regime the energetic electrons can interact with plasma via generation and absorption of electrostatic Langmuir waves. Propagation can no longer be treated as ballistic and models must take non-linear effects into account.

In this chapter, we investigate electron propagation from the Sun to the Earth taking into account the scattering of electrons by beam-driven Langmuir waves. We show for the first time that the generation and absorption of Langmuir waves by an electron beam in the non-uniform inner heliosphere leads to the appearance of a break energy in the observed spectrum at the Earth and naturally explains the observed early injection of low energy electrons.

2.1.1 In-situ solar electron beam observations

Solar flares are extremely efficient at accelerating electrons to energies well above the thermal, background level. Such electron beams can be observed subsequently either by their emission at X-ray and radio wavelengths or escaping along interplanetary magnetic field lines via direct electron measurements near the Earth (see Benz 2008, for a review). The first in-situ observations of energetic particles (van Allen & Krimigis 1965) opened up the non-electromagnetic window of flare accelerated particle observations. Since then solar energetic electron events have been found to be closely related observationally (e.g. Ergun et al. 1998; Gosling et al. 2003; Krucker et al. 2007) and theoretically to Type III solar radio bursts, having about a 90% association (Lin 1985; Lin et al. 1986).

Electron beams travel through a background flux of non-relativistic electrons, known as the solar wind. Background solar wind electrons are not in thermal equilibrium with a Maxwellian distribution but exist in a quasi-thermal state with electrons extending to much higher energies (Lin et al. 1972). Their velocity distribution function at all pitch angles is usually modelled using two convecting bi-Maxwellians, the core and the halo, shown in Figure 2.1. A skewed distribution also exists in the fast solar wind parallel to the magnetic field direction. Known as the strahl, this high energy tail usually propagates away from the Sun and has a narrow pitch angle distribution between 10-20° wide. Observations of the background solar wind electrons have shown that a kappa distribution can better model the solar wind (Maksimovic et al. 2005; Le Chat et al. 2010). The kappa distribution more accurately models the electron temperature whilst having fewer free parameters than the sum of two Maxwellians.

Electron beams associated with solar flares are generally impulsive in their time profile. Impulsive electron events often extend to 1 keV (Lin et al. 1996) with some even extending down to the 0.1 to 1 keV energy range (Gosling et al. 2003). An example of the time profile of an impulsive electron event can be seen in Figure 2.2 from 2 keV to 500 keV. This time profile shows the rapid onset and also near time-of-flight velocity dispersion (e.g. Lin 1985; Krucker et al. 1999, 2007) typical of such
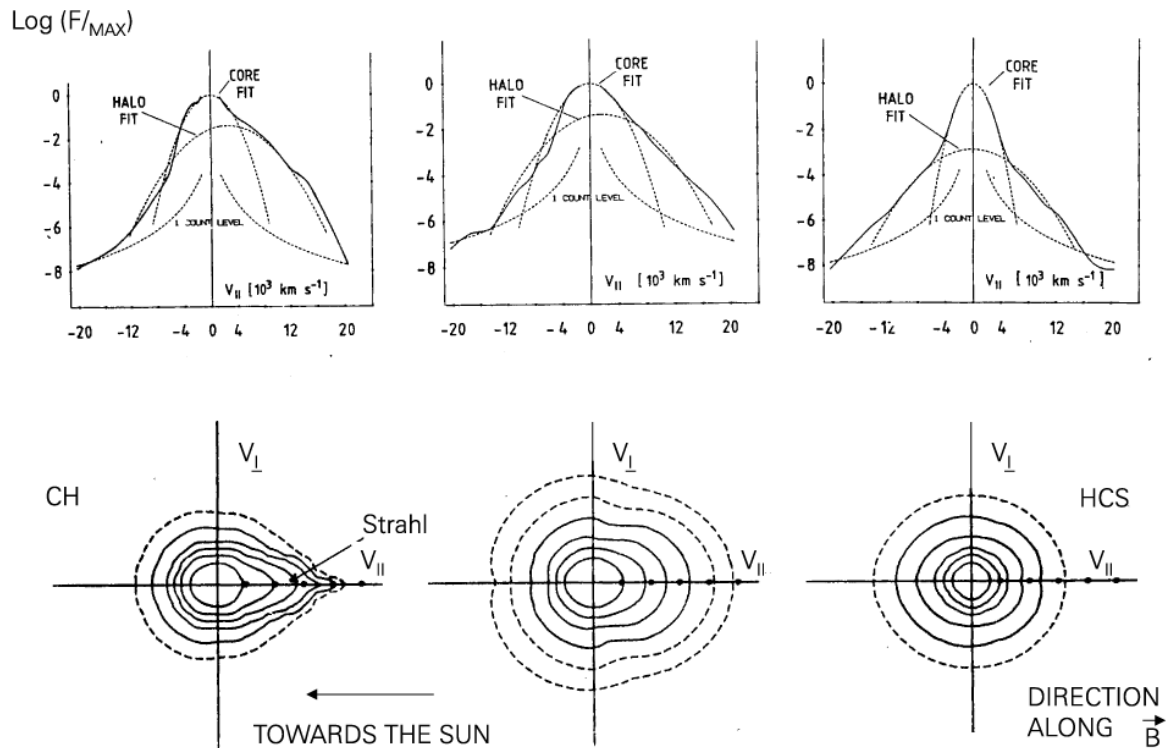
Figure 2.1: Electron velocity distribution functions as energy spectra (top) and velocity space contours (bottom) for fast (left), intermediate (middle) and slow (right) solar wind. Isodensity contours are in steps by a factor of 10. Note the core-halo structure and the strahl of suprathermal electrons in fast solar wind (from Marsch 2006, adapted from Pilipp et al. (1987))

events. The electrons also have a beamed pitch-angle distribution at lower energies < 18 keV (e.g. Lin 1990). From these three facts, it is often believed that such electrons propagate scatter-free from the Sun to the Earth (e.g. Wang et al. 2006). The observed correlation between the spectral indices of energetic electrons at the Sun from X-ray data and the Earth from in-situ data (Lin 1985; Krucker et al. 2007) is often viewed as an additional support for scatter-free transport.

Solar impulsive electron events detected in-situ generally display broken power-law energy distributions with lower energies having harder spectra. Figure 2.2 shows an example of this broken power-law distribution in energy space along with the time
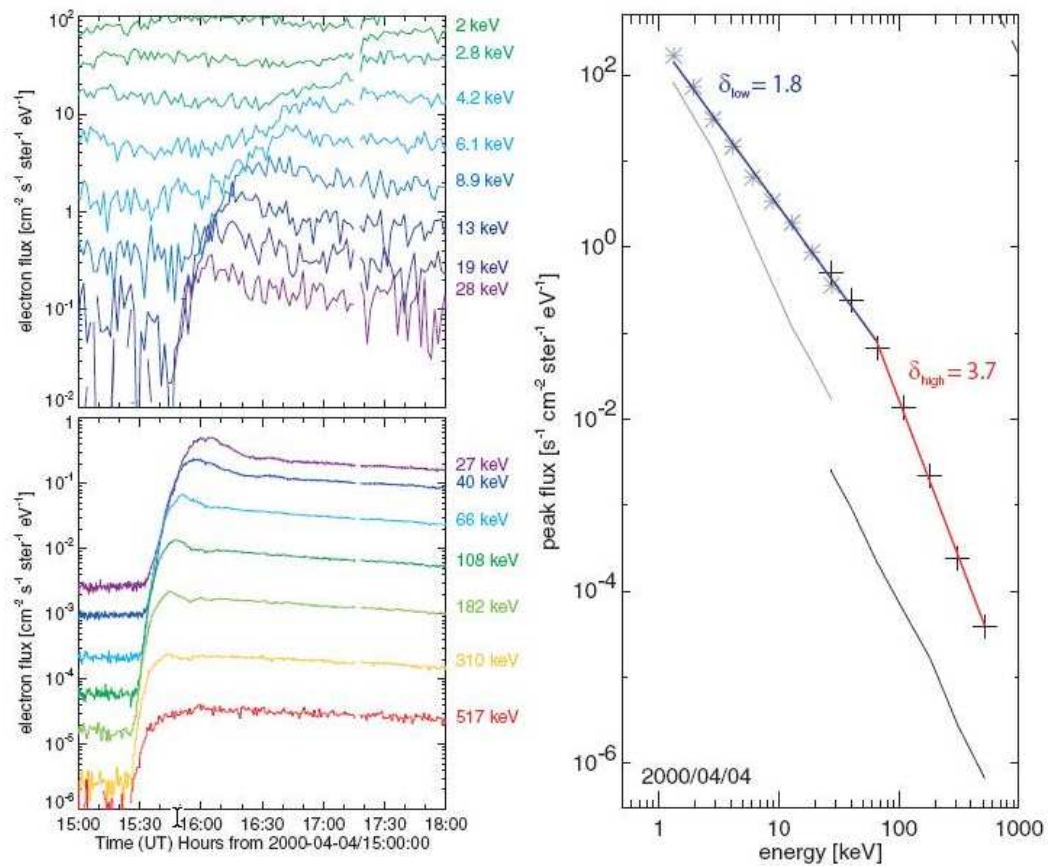
Figure 2.2: Example of a typical solar impulsive electron event observed from the keV range up to 500 keV. Left: time profiles at different energies as indicated. The top panel shows data from the electrostatic analyzer (EESA-H) and the bottom panel shows data from the SST. Note the much higher sensitivity of SST. Right: derived electron peak flux spectrum of the same event. EESA-H data are shown in grey (asterisk), while the SST measurements are given in black (crosses). The thin curves below give an estimate of the background emission. The red and blue curves are the power-law fits to the data, with a pronounced break around 60 keV (Krucker et al. 2009)

profiles of the same event. Broken power-law distributions were first observed by Wang et al. (1971). Their origin has remained ambiguous since then, being either a signature of the acceleration mechanism or a transport effect. A recent statistical survey was carried out by Krucker et al. (2009) on 62 impulsive events. They found

the average break energy was ≈ 60 keV with averaged power-law indices below and above the break of $\delta_{low} = 1.9 \pm 0.3$ and $\delta_{high} = 3.6 \pm 0.7$ respectively. The power-law indices have an average ratio $\delta_{low}/\delta_{high}$ of 0.54 with a standard deviation of 0.09. The power-law indices also correlate with a coefficient of 0.74.

Observationally, in-situ spacecraft are able to detect these electron beams at times related to observed type III emission from the Sun. Of these spacecraft, the WIND spacecraft is equipped with a 3-D Plasma and Energetic Particles instrument (Lin et al. 1995) for detailed analysis of electron distribution functions. The STEREO spacecraft are equipped with a Solar Electron Proton Telescope (SEPT) (Müller-Mellin et al. 2008) which is also able to detect electron energies between 20-400 keV. Previous spacecraft able to detect high energy electrons include the ISEE project consisting of three seperate spacecraft. Most noteable for high energy electron detection was the ISEE-3 spacecraft which was the first spacecraft to be placed at the L1 Lagrangian point. Electrons could be detected by a Berkeley built instrument (Anderson et al. 1978) sensitive to the range 2-1000 keV (see Lin 1985, for a review of energetic electron results from ISEE-3).

2.1.2 Solar electron beam onset times

Although this broad picture is often supported by observations, the detailed picture of electron transport and plasma radio emission is far from well-understood. This is largely due to electron beam propagation and radio emission being essentially a non-linear multi-scale problem, and is the subject of a large number of ongoing simulation efforts (e.g. Takakura & Shibahashi 1976; Magelssen & Smith 1977; Grognard 1982; Kontar 2001d; Li et al. 2006b). The type III radio emission can be used in conjunction with electron beam measurements to analyse the travel time of the energetic electrons. Studies have shown an energy dependent discrepancy where, despite the near time-of-flight dispersion, lower energy electrons appear to arive sooner than expected and higher energy electrons arrive later than expected (Lin et al. 1981; Krucker et al. 1999; Maia et al. 2001; Wang et al. 2006).
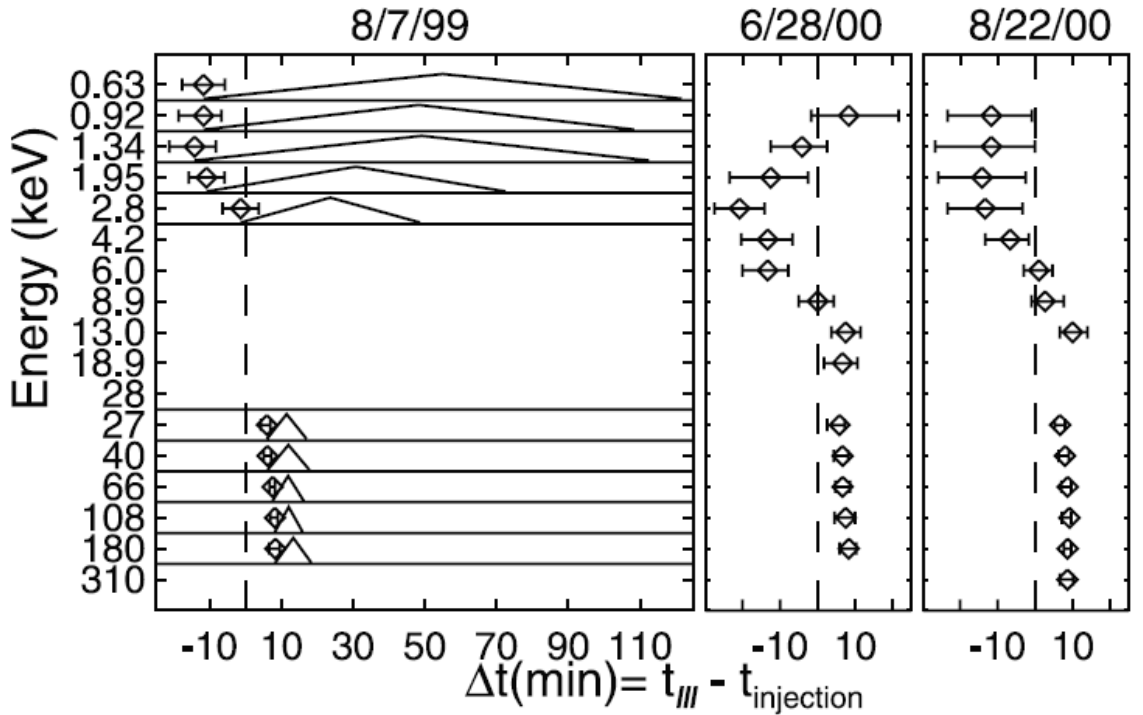
Figure 2.3: Comparison of the start times of inferred electron injections at different energies (diamonds) and the release time of type III burst (dash line) at the Sun for the three events. The electron delay (X-axis) is shown in min. For the 7 August 1999 event (left), the inferred injection profiles are shown by triangles. The injection analysis was not available at some channels due to a data gap or poor statistics (Wang et al. 2006).

Solar impulsive electron events can span a broad range of energies, from a few keV to hundreds of keV (Lin et al. 1996). Since the low energy electrons of a few keV should lose their energy collisionally in the low corona, these electrons are believed to be accelerated high in the corona (Lin et al. 1996). Recent time-of-injection analysis (Wang et al. 2006) assuming scatter free propagation of solar energetic electrons suggests the existence of two electron populations, one low energy beam injected before the start of the type III burst and one high energy beam injected after the type III burst. This conclusion is evident from the different arrival times of electrons at the Earth, observed in Figure 2.3.

One difficulty in assessing the electron onset times arises from the background

electron flux which can add a large observational uncertainty. The background electron intensity fluctuates in time and shows non-dispersive variation on different timescales (Kahler & Ragot 2006). It is thus very hard to make an accurate estimate of the mean background electron flux, which is required when considering electron beam onset times.

Another difficulty for electron onset times is the assumption that the path length remains fixed from the Sun to 1 AU. The path length is calculated assuming particles travelling along magnetic field lines described through the Parker spiral model. This gives lengths of around 1.2 AU (e.g. Ho et al. 2003; Wang et al. 2006). Constant path length assumes there is no significant pitch angle or any disturbances in the solar wind. The presence of EIT waves has been detected at similar times to some electron beams that were detected with a late onset time (Lin 2000). It is possible that such waves change the magnetic configuration of the inner heliosphere to something more complicated than the typical Parker spiral model, causing longer travel time for energetic electrons.

One further assumption is that particles do not change their dynamics while travelling from the Sun to 1 AU. If particles are accelerated or decelerated during transport their velocity will not be constant. Particles which arrive with a different velocity than they started with are not suitable candidates when using the simple formula $t_0 = t_A - L/v$ where t_0 is the injection time, t_A is the arrival time and L is the path length. Impulsive solar electrons are well correlated with type III radio bursts. If the electron beams are responsible for this radio emission, they are also inducing Langmuir waves. The induction of Langmuir waves converts electron beam kinetic energy density into wave energy density. The electrons thus do not travel with a constant velocity. To explore how this affects the travel time, the simulation of an electron beam from the Sun to the Earth has to be considered with the inclusion of energy transfer processes.

2.2   Electron propagation model

2.2.1   Electron beam dynamics

The transport of energetic electrons in the heliospheric plasma is governed by a variety of different processes (see Melrose 1990, for a review). To model high energy electron beams associated with type III emission we also have to take into account induced Langmuir waves from the bump-in-tail instability. In this work we consider solar energetic electrons propagating along magnetic field lines in the inner heliosphere and assume their transport can be described one-dimensionally ignoring electromagnetic effects (Takakura 1982). Under this assumption, the evolution of the electron distribution function $f(v, x, t)$ [electrons cm^{-4} s] and the spectral energy density of electron Langmuir waves $W(v, x, t)$ [ergs cm^{-2}] can be described self-consistently by the following kinetic equations (e.g. Kontar 2001a)

$$\frac{\partial f}{\partial t} + v\frac{\partial f}{\partial x} = \frac{4\pi^2 e^2}{m_e^2}\frac{\partial}{\partial v}\frac{W}{v}\frac{\partial f}{\partial v} \tag{2.1}$$

$$\frac{\partial W}{\partial t} + \frac{\partial \omega}{\partial k}\frac{\partial W}{\partial x} - \frac{\partial \omega_{pe}}{\partial x}\frac{\partial W}{\partial k} = (\gamma(v, x) - \gamma_c - \gamma_L)W \tag{2.2}$$

$W(v, x, t)$ plays the similar role for Langmuir waves as the electron distribution function does for particles. The dispersion relation of Langmuir waves is $\omega_L^2(k) = \omega_{pe}^2 + 3v_{Te}^2 k^2/2$, so the group velocity of Langmuir waves is $\partial \omega_L/\partial k = frac32v_{Te}^2/v$ in Equation (2.2) where $v_{Te} = \sqrt{k_B T_e/2m_e}$.

The first terms on the right hand sides of Equations (2.1,2.2) describe the resonant interaction, $\omega_{pe} = kv$ of electrons and Langmuir waves, first derived by Drummond & Pines (1962); Vedenov et al. (1962). The Langmuir wave growth rate is given by

$$\gamma(v, x) = \frac{\pi\omega_{pe}}{n_e}v^2\frac{\partial f}{\partial v}. \tag{2.3}$$

By itself, this growth rate gives the instability criteria of $\partial f/\partial v > 0$.

Landau damping

To take into account the background Maxwellian plasma we have the term $-\gamma_L W$ or the Landau damping term. This describes the resonant interaction of electrons and

Langmuir waves from the background plasma. Due to the negative velocity gradient in the tail of the Maxwellian distribution, this resonant interaction causes the background plasma to absorb Langmuir waves. More formally, assuming a Maxwellian plasma described by

$$f(v) = \frac{n_e}{\sqrt{2\pi}v_{Te}} \exp\left(-\frac{v^2}{2v_{Te}^2}\right) \tag{2.4}$$

the growth rate of Langmuir waves and hence the Landau damping is given by

$$
\begin{aligned}
-\gamma_L &= \frac{\pi\omega_{pe}}{n_e}v^2\frac{\partial}{\partial v}f(v) \\
&= -\sqrt{\frac{\pi}{2}}\omega_{pe}\left(\frac{v}{v_{Te}}\right)^3\exp\left(-\frac{v^2}{2v_{Te}^2}\right)
\end{aligned} \tag{2.5}
$$

where v denotes the Langmuir wave phase velocity. The strong Landau damping near v_{Te} means the background Maxwellian plasma reduces the level of Langmuir waves to zero[1]. This allows us to set a lower limit, $v_{min} > v_{Te}$ on the velocities modelled and only consider the background Maxwellian plasma through Landau damping and collisions.

Collisional damping

The collisional damping rate of Langmuir waves represents the loss of energy associated with the forced oscillation of electrons which experience a Coulomb collision. This can be explicitly written (e.g. Melrose 1980b) as

$$\gamma_c = \frac{1}{3}\left(\frac{2}{\pi}\right)^{0.5}\frac{4\pi n_e e^4}{m_e^2 v_{Te}^3}\frac{\pi}{\sqrt{3}}G(T_e\omega). \tag{2.6}$$

The last term $G(T_e, \omega)$ is the Gaunt factor[2] where T_e is the background electron temperature. Assuming that $\omega \ll T_e/\hbar$ (the energy of a Langmuir wave is substantially less that the kinetic energy of a thermal particle) and $\omega \le \omega_{pe}$ we can approximate $\frac{\pi}{\sqrt{3}}G(T_e,\omega)$ as the Coulomb logarithm $\ln\Lambda$. Explicitly we use the approximation of

---

[1]Strictly speaking the level of waves will not reduce to zero but will reduce to the thermal level. The thermal level is spontaneously generated from electron-electron Coulomb collisions. This will be modelled later.

[2]A quantum mechanical correction factor applied to the semi-classical Kramers formula for photon absorption

$\ln \Lambda = 29.7 - 0.5 \ln(n_e)$ which has a rough value of 20 in the corona and 26 at the Earth. The first set of constants $\frac{1}{3} \left(\frac{2}{\pi} \right)^{0.5} 4$ has an approximate value of 1. We can then express the collisional damping term as

$$\gamma_c \approx \frac{\pi n_e e^4}{m_e^2 v_{Te}^3} \ln \Lambda. \tag{2.7}$$

The dependency of the collisional damping on density makes it only important in the dense atmosphere of the low solar corona. It is thus necessary for the initial propagation and instability of the electron beam which starts deep within the corona. The collisional damping changes the instability criteria of the electron beam such that $\partial f / \partial v > \gamma_c$.

Background density gradient

The effect of the background electron number density gradient on Langmuir waves is governed by the last term on the left hand side of Equation 2.2. This can be expressed in velocity space through the resonant condition $\omega_{pe} = kv$ giving

$$-\frac{\partial \omega_{pe}}{\partial x} \frac{\partial W}{\partial k} = \frac{\partial \omega_{pe}}{\partial x} \frac{v^2}{\omega_{pe}} \frac{\partial W}{\partial v} = \frac{v^2}{L} \frac{\partial W}{\partial v}. \tag{2.8}$$

Similar to Kontar (2001a) we define the characteristic scale of plasma inhomogeneity, $L = \omega_{pe}(\partial \omega_{pe}/\partial x)^{-1} = 2n_e(\partial n_e/\partial x)^{-1}$. This value has to be larger than the wavelength of any Langmuir waves considered to remain within the Westzel-Kramers-Brillouin (WKB) approximation of geometrical optics. The term represents the changing refractive index of the background plasma. Langmuir waves shift in k-space (or phase velocity space) with a direction depending upon the sign of the density gradient. We consider a simplistic model of the inner heliosphere plasma that has only a decreasing density gradient[3]. This results in Langmuir waves shifting to lower phase velocities (higher values of k).

To show the effect of Langmuir waves shifting in velocity space due to density gradients a simplified version of Equations (2.1,2.2) was used which remained static in position space. The only terms used were the quasilinear terms and the velocity

---

[3]A more realistic model will be used in Chapter 3.

dispersion term giving the simplified equations.

$$\frac{\partial f}{\partial t} = \frac{4\pi^2 e^2}{m^2} \frac{\partial}{\partial v} \frac{W}{v} \frac{\partial f}{\partial v} \tag{2.9}$$

$$\frac{\partial W}{\partial t} - \frac{\partial \omega_{pe}}{\partial x} \frac{\partial W}{\partial k} = \frac{\pi \omega_{pe}}{n_e} W v^2 \frac{\partial f}{\partial v}. \tag{2.10}$$

An unstable $(df/dv > 0)$ initial electron beam distribution function was used to simulate wave growth as follows

$$f(v, t = 0) = \frac{2n_b v}{v_0^2}, \qquad v \leq v_0 \tag{2.11}$$

with the maximum beam velocity $v_0 = 10^{10}$ cm s^{-1} and beam density $n_b = 100$ cm^{-3}. The scale of plasma inhomogeneity $L = -1.29 \times 10^{10}$ cm, similar to coronal conditions. The resultant simulation was compared with the analytical form of the distribution function calculated from (Kontar 2001b). This can be seen in Figure 2.4. The plateau in the distribution function is formed early on, converging close to the analytical solution at time $t = 0.1$ $s \gg \tau_{ql}$ where τ_{ql} is the quasilinear interaction time. Comparing the simulation curves with the analytical curves, we can see they are in good agreement. The drift of Langmuir waves to smaller phase velocities due to the plasma inhomogeneity is clear.

2.2.2   Background plasma parameters

The background plasma is modelled using a heliospheric density model that originated from Parker (1958) and was modified by (Mann et al. 1999). The density is calculated by numerically integrating the equations for a stationary spherical symmetric solution for solar wind.

$$r^2 n(r) v(r) = C = const \tag{2.12}$$

$$\frac{v(r)^2}{v_c^2} - \ln\left(\frac{v(r)^2}{v_c^2}\right) = 4\ln\left(\frac{r}{r_c}\right) + 4\frac{r_c}{r} - 3 \tag{2.13}$$

where $v_c \equiv v(r_c) = (k_B T_e / \tilde{\mu} m_p)^{1/2}$, $r_c = GM_s/2v_c^2$, T_e is the electron temperature, M_s is the mass of the Sun. The constant appearing above is fixed by satellite measurements near the Earth's orbit (at $r = 1$ AU, $n_e = 6.59$ cm^{-3}) and equates to 6.3×10^{34} s^{-1}
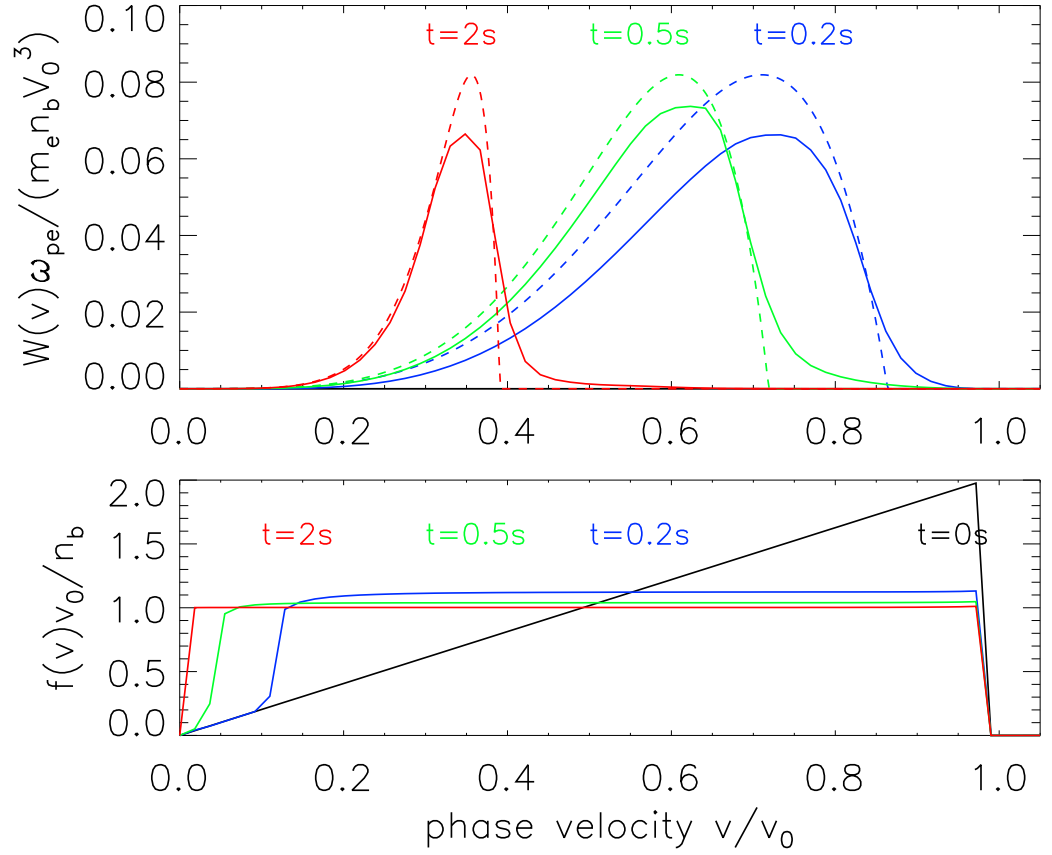
Figure 2.4: Converging solution of equation (2.11) to a stationary state with velocity dispersion. The numerical solution was obtained at four time moments, 0 s, 0.2 s, 0.5 s and 2 s. $v_0 = 10^{10}$ cm s^{-1}, $n_b = 100$ cm^{-3}, $L = -1.29 \times 10^{10}$ cm. Dashed curves correspond to the simplified analytical solution

(Mann et al. 1999). The model is static in time because the characteristic electron beam velocities are much larger than solar wind speeds. The temperature was kept constant at $T_e = 10^6$ K, giving a thermal velocity of $v_{Te} = 5.5 \times 10^8$ cm s^{-1}. It should be noted that the constant temperature allowed for the approximation to the Coulomb logarithm. A more accurate definition taking into account a changing temperature is $\ln \Lambda = \lambda_D k_B T_e / e^2$ where $\lambda_D = v_{Te} / \omega_{pe}$ is the plasma Debye length. However, this is not required. Landau damping affecting the beam is heavily dependent upon the
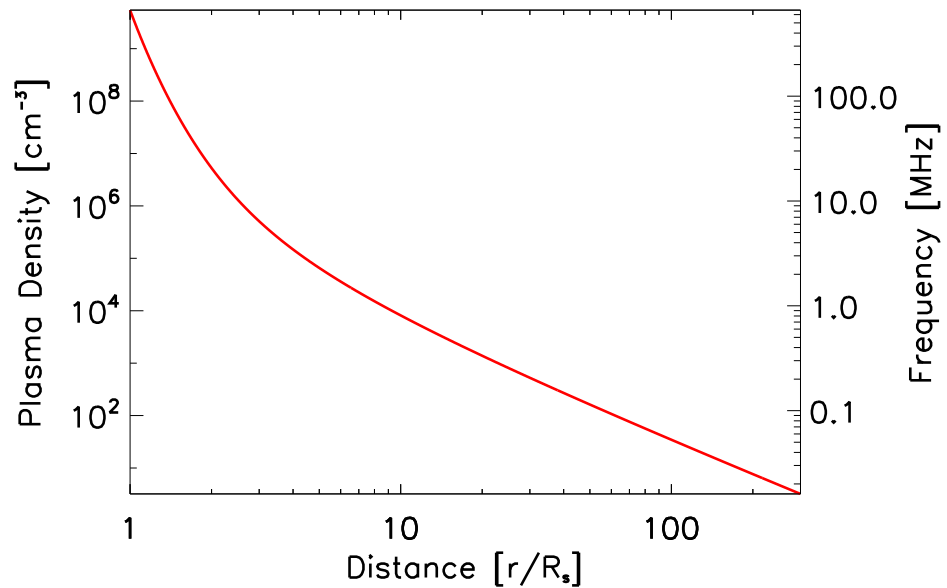
Figure 2.5: The Parker density model using the constant defined in Mann et al. (1999). The photosphere of the Sun corresponds to 1 R_s. The path length of an electron beam to the Earth corresponds to 263 R_s which is 1.2 AU.

temperature of the background plasma. By keeping temperature at a constant 1 MK we slightly overestimate the wave damping at low phase velocities. This is offset by the assumption that the background is a Maxwellian. In reality the background plasma is closer to a kappa distribution which would increase the thermal velocity and as such increase the level of Landau damping.

The initial spectral energy density of the Langmuir waves is assumed to be approximately at the thermal level (e.g. Kontar & Pécseli 2002) decribed by

$$W(v, x, t = 0) \approx k_B T_e / (2\pi^2 \lambda_D^2) \qquad (2.14)$$

where T_e is the background plasma temperature, k_B is Boltzmann constant and λ_D is the electron Debye length.

2.2.3 Initial electron beam distribution

The initial electron distribution function models the energetic electron beam accelerated in the solar corona. It is assumed to be a power-law in velocity (or energy) space. The power-law distribution assumption comes from both the derived electron spectrum associated with HXR inducing electron beams and in-situ observations of the peak flux and fluence spectra of electron beams at the Earth. It has a Gaussian profile in position space with a finite spatial size d at initial time $t = 0$ described by

$$f(v, x, t = 0) = g_o(v) \exp\left(-\frac{x^2}{d^2}\right) \tag{2.15}$$

where

$$g_0(v) = n_b \frac{(\alpha - 1)}{v_{min}} \left(\frac{v_{min}}{v}\right)^\alpha, \quad \alpha > 1 \tag{2.16}$$

is the initial electron distribution function normalized to n_b, the beam electron number density. v_{min} is the low velocity cutoff, and α is the spectral index of the initial electron beam. The injected electron flux density differential in energy $F_0(E, x, t)$ [electrons cm^{-2} eV^{-1} s^{-1}] is also a power law $F_0(E) \sim E^\delta$, where $\delta = \alpha/2$. The initial spatial size of the electron cloud was taken as $d = 5 \times 10^9$ cm, so the injection time of 5×10^9 cm s^{-1} electrons is one second, which is a typical duration of type III bursts near the starting frequencies (Dulk 1985). The size of the electron cloud is larger than what would be expected in a solar flare. However, it effectively simulates a time injection. The actual height of the electrons from the solar surface is not important here, just the density profile. As such, the large initial size does not significantly affect the results. A more realistic size is simulated in Chapter 3 and the effect of the initial size is analysed in Chapter 4.

The low velocity cutoff was taken equal to approximately twice the thermal electron velocity $v_{min} = 1.2 \times 10^9$ cm s^{-1}. The initial beam density n_b was varied between $10^{-3} < n_b < 1$ cm^{-3}. These densities are lower than those observationally predicted but were required for realistic simulation computational times. The initial beam spectral index $\delta = \alpha/2$. was varied from $2.5 \rightarrow 4.5$ where 3.5 is the approximate mean observational value (Krucker et al. 2009).

2.2.4   Numerical methods and code verification

The system of kinetic equations (2.1, 2.2) have been solved using explicit finite difference methods as described in Kontar (2001c). To solve the differential terms in velocity space for Equations (2.1) and (2.2) a first order upwind scheme was used. The upwind scheme is described by

$$f(v, t + \Delta t) = a\Delta t \frac{(f(v + \Delta v), t) - f(v, t))}{\Delta v}, \qquad a < 0 \tag{2.17}$$

$$f(v, t + \Delta t) = a\Delta t \frac{(f(v), t) - f(v - \Delta v, t))}{\Delta v}, \qquad a > 0 \tag{2.18}$$

A first order upwind scheme is fast to compute but suffers from numerical diffusion. The large computational demand of the code required a fast scheme. Moreover, the numerical diffusion from the upwind scheme is much smaller than the diffusion which occurs from the quasilinear terms and the background density gradient term.

 The numerical diffusion from the first order upwind scheme was not adequate for computing the differential term in position space. A more accurate scheme was required. Similar to Kontar (2001c) the van Leer monotonic transport finite difference method (van Leer 1974, 1977a,b) was used to model the spatial propagation of the electrons and Langmuir waves. Such a scheme substantially reduces the numerical diffusion on the distribution function which would otherwise cause an artificially reduced magnitude at distances far from the Sun.

 It is always important to confirm numerical code will output a correct answer given an appropriate input. All the different terms in Equations (2.1) and (2.2) were individually tested for correctness. This was achieved by inputting a function which had a analytical solution. The output from the code was then overplotted on the analytical solution to confirm the code was working properly. To test the quasilinear terms the input described by 1.8 was used with analytical solutions (1.9) and (1.10). Figure 1.5 shows how both the electron distribution function and Langmuir wave spectral energy density tend towards the analytical solution. For the term which considered the changing refractive index Equation 2.11 was used as an input where the analytical solutions are described in Kontar (2001b). Figure 2.4 shows how the analytical solution

is reached at times greater than the characteristic quasilinear time τ_{ql}. The propagation of the electron distribution function and the Langmuir wave energy density was checked using a Gaussian input described by Equation 2.15 with analytical solution $f(v, x, t) = g_0(v)exp(-(x - vt)^2/d^2)$ at time $t > t_0$.

Fortran code was used to simulate the electron beam and Langmuir wave evolution in time. All other computation (including the analytical verification of the code) was done using IDL. The Fortran code outputted relevant values to large data files which were then read in by IDL routines. All the graphs produced were created using IDL which required writing a suite of programs that could deal with manipulating the data into workable arrays and defining new parameters like the fluence of the electron beam. IDL was also used in the analysis of the results which involved computing artificial backgrounds, fitting power-laws to the data, making movies to observe the behaviour of key variables with time and checking for the conservation of key variables like the number of particles and the energy of both electrons and Langmuir waves.

To preserve the information about the initial Gaussian distribution the discretisation in position space Δx had to be smaller than the characteristic size of the Gaussian d. The initial size of Δx was thus of the order of 10^8 cm. The distance required for the electron beam to reach the Earth was 1.2 AU which is 2×10^{13} cm. If the spacing is constant, the simulations will take $\sim 10^5$ grid spaces to cover 1.2 AU, becoming computationally intractable.

To solve this issue Δx was allowed to vary with distance. The varying Δx uses the discretisation of velocity space as a bound on the maximum analytical information required. The finite size of each velocity step causes a spread in the characteristic size of the electron distribution function of approximate size:

$$f(v, x, t = 0)d \approx f(v, x, t)(d + t\Delta v) \tag{2.19}$$

for initial beam size d, velocity step size Δv and travel time t. As Δx is bound by d and we lose information about d over time, we can increase Δx further away from the Sun. The travel time t in Equation 2.19 is calculated using the time required for the maximum velocity of the electron beam v_{max} to travel distance Δx. We can find out

how much the discrete nature of velocity will have impacted d after n mesh points by calculating d_n with the recurrence relation

$$d_n = d_{n-1} + \Delta v \frac{\Delta x_{n-1}}{v_{max}} \tag{2.20}$$

and hence

$$\Delta x_n = 0.2 d_n \tag{2.21}$$

where d_0 is the initial characteristic size of the electron beam and Δx_0 is $0.2d_0$. This increasing size of Δx allows for a smaller number of points to cover the desired distance of 1.2 AU whilst keeping Δx small enough that any loss of information from the increasing step size is smaller than the information loss caused by discretisation in velocity space.

2.3 Propagation of electrons from the Sun

2.3.1 Initial wave growth

The initial power-law injection of the impulsive electron beam in the solar corona is stable to Langmuir wave growth at $t = 0$ at all points in space ($\partial f / \partial v < 0$). The propagation of electrons with a spectrum of velocities causes faster particles to race ahead of the slower electrons creating the instability $\partial f / \partial v > 0$. As mentioned previously, the inclusion of the energy losses which Langmuir waves undergo due to Coulomb collisions changes this instability criteria to $\partial f / \partial v > \gamma_c$. The collisional damping term is proportional to the background electron density so it is strong in the corona and weak near the Earth. Figure 2.6 shows how the collisional time, $1/\gamma_c \approx 4 \times 10^7/n_e$ (at $T_e = 10^6$ K), compares to the quasilinear time, $1/\gamma(v,x) \approx n_e/(\omega_{pe} n_b)$, for the highest and lowest beam densities used in the simulations. The collisional time increases as the electrons propagate out into the heliosphere such that at $x > 1$ R$_\mathrm{s}$ the quasilinear growth becomes the dominant process. We thus don't expect any Langmuir waves in the corona for the initial beam densities used. Type III emission
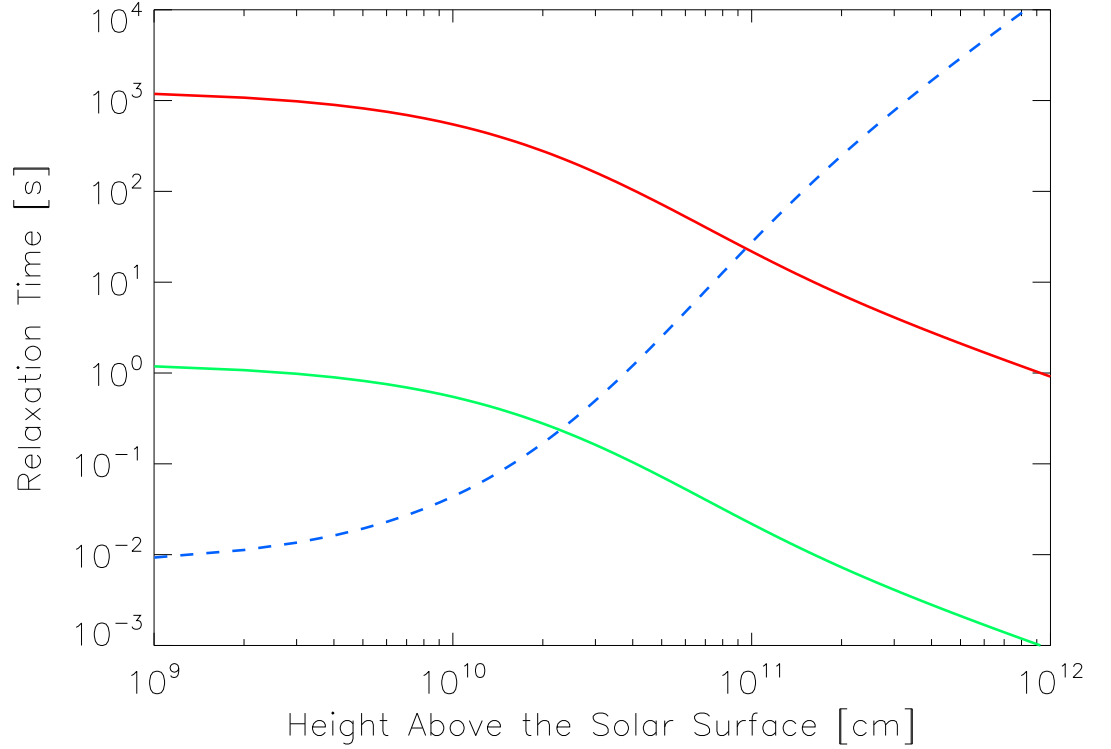
Figure 2.6: The quasilinear and collisional damping relaxation times in the corona. Two different beams with densities 1 (green) and 10^{-3} cm^{-3} (red) are shown. The collisional damping time is independent of initial beam density.

in the corona dictates that we should observe Langmuir wave growth. Initial beam densities to achieve this must therefore be higher than 10^2 cm^{-3}.

The collisional damping of waves is not the only term that discourages Langmuir wave growth in the corona. The growth factor of Langmuir waves $\gamma(v, x) \sim 1/\sqrt{n_e}$. As background electron density decreases with distance from the Sun the further the beam travels, the easier it will become to generate waves. Moreover, an electron beam has an initial instability distance it has to propagate before $\partial f/\partial v$ grows enough to induce Langmuir waves. Starting with an initial spatial Gaussian distribution with characteristic size $d = 5 \times 10^9$ cm means electrons are spread over a wide distance. The larger the initial spread in space of an electron distribution, the longer it will take the

fast electrons to outpace the slower ones. Beam instability distance will be covered in more detail in Chapter 4.

Another variable affecting $\gamma(v, x)$ is the velocity of electrons. The growth rate, $\gamma(v, x) \sim v^2$ meaning higher velocity electrons find it easier to resonantly generate waves. However, the beam starts as a power-law in velocity space such that $g_0(v) \sim v^{-\alpha}$ where $\alpha \geq 5$. The flux of electrons and hence the magnitude of $\partial f / \partial v$ decreases with velocity. As $\alpha > 2$, $\gamma(v, x)$ actually decreases with velocity. We thus expect Langmuir waves to be resonantly generated by electrons with smaller velocities first[4]. The higher velocity electrons will generate Langmuir waves closer to the Earth as n_e decreases. The lower the magnitude of α, the larger the ratio of high:low energy electrons, and the closer to the Sun we can expect high velocity (20 v/v_{Te}) electrons to induce Langmuir waves.

2.3.2   Beam-plasma structure

Using our model, the further electrons propagate from the Sun to the Earth the more Langmuir waves they induce. Figure 2.7 demonstrates the transport of an electron beam at three different times for a beam with $n_b = 0.1$, $\alpha = 7$. Figure 2.7 and subsequent figures in this chapter are taken from (Kontar & Reid 2009). After 15 s the beam was not able to induce any Langmuir waves. After 150 s there is a low level of Langmuir waves but only up to 10 v/v_{Te}. After 1500 s some electrons have reached the Earth, the level of waves is very high, and waves have been induced at much higher phase velocities.

A beam-plasma structure is also demonstrated in Figure 2.7. The electrons and Langmuir waves exist in the same areas of phase space. The group velocity of Langmuir waves $v_g \ll v$ so the wave energy is unable to travel at the same speed as the electrons. As mentioned in Section 1.2.4, electrons at the front of the beam induce Langmuir waves via $\partial f / \partial v > 0$ while electrons at the back of the beam absorb Langmuir waves via $\partial f / \partial v < 0$. This solution to Sturrock's dilemma allows the electron beam to travel

---

[4]Waves are not generated at velocities close to v_{Te}, due to Landau damping.
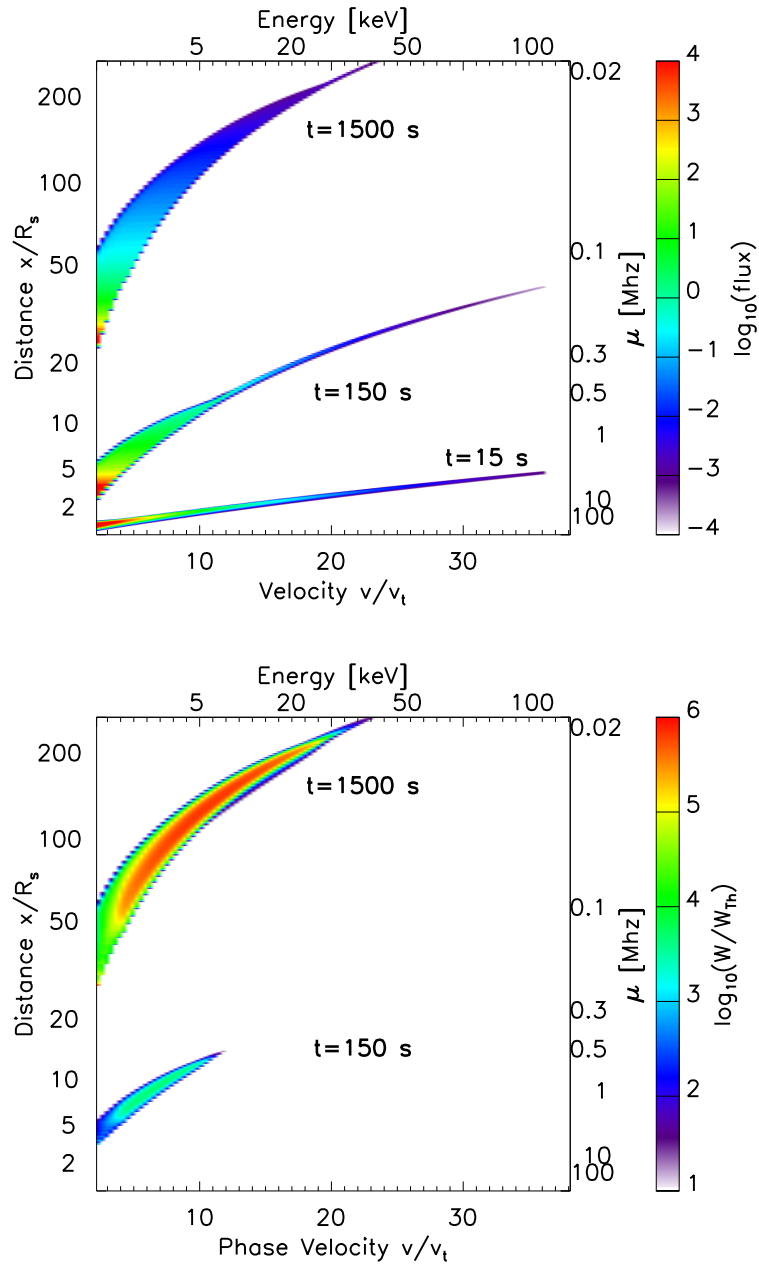
Figure 2.7: Colour coded contour plot at three separate times of the electron beam flux (top) and the spectral energy density (bottom). $n_b = 0.1$, $\alpha = 7$. Distance, velocity and spectral energy density are normalised by one solar radii, the thermal velocity and the thermal level of waves respectively. The beam becomes more unstable over time inducing more intense Langmuir waves at higher phase velocities.

from the Sun to distances of 1 AU and beyond.

Electrons diffusing in velocity space can be seen in Figure 2.7. Electrons with velocities that are able to induce a high level of Langmuir waves have a noticeably wider distribution in velocity space. This is especially visible at $t = 150$ s where the electrons have a thin distribution above 10 v/v_{Te} and a much wider distribution below. Generation of Langmuir waves plateaus the distribution such that $\partial f/\partial v \to 0$.

To examine the electron diffusion requires a one dimensional cut of the simulations in velocity space (Figure 2.8). The high energies > 30 keV do not have enough a large enough flux of electrons to induce waves and as such still have a thin distribution in velocity space. At energies < 30 keV a large magnitude of Langmuir waves is induced and the electron distribution takes the form of a broad plateau. It is important to emphasize the maximum energy of electrons able to induce Langmuir waves changes during propagation.

The background electron density gradient affects a distribution of Langmuir waves as demonstrated in Figure 2.4. A beam-plasma structure travelling from the Sun to the Earth is affected slightly differently than Figure 2.4 because it does not remain in any one spatial point but propagates through the density inhomogeneity. Moreover, the instability of the electron distribution function occurs over a narrower range of velocities. The shifting of Langmuir waves can be seen in the velocity slice of Figure 2.8. The Langmuir wave energy density is spread over a much wider range of phase velocities. Spreading is especially evident for the Langmuir waves induced by lower energy electrons.

2.4 Electron energetics at the Earth

2.4.1 Fluence spectra at 1AU

Traditionally *in-situ* measurements of energetic electrons (e.g. Lin et al. 1995) provide the flux density differential in energy $F(E, x, t) = f(v, x, t)/m_e$ [electrons cm^{-2} s^{-1} keV^{-1}] and the fluences (flux integrated over the duration of an event) [electrons cm^{-2}
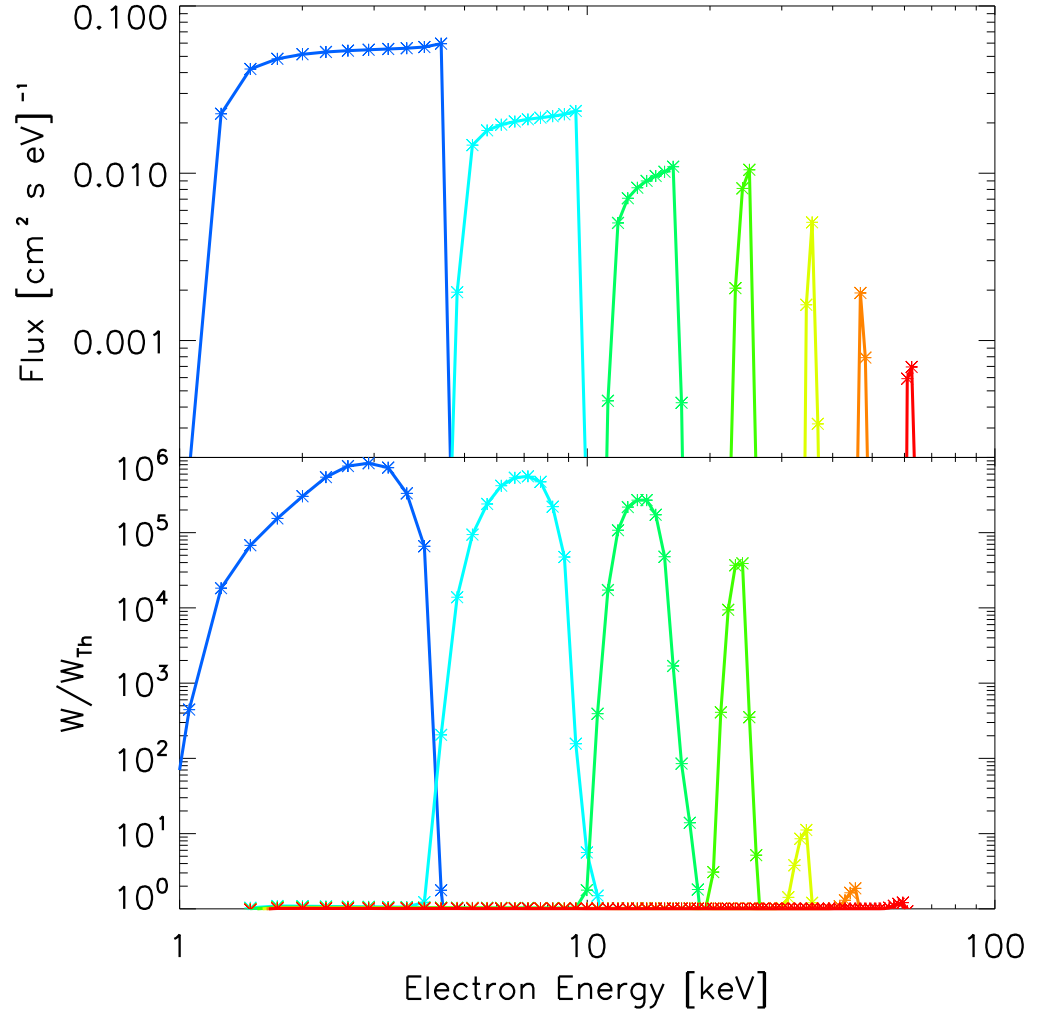
Figure 2.8: 1D velocity slice of electron beam flux and spectral energy density at 108 R_s from the initial electron beam location. $n_b = 0.1$, $\alpha = 7$. The electron flux (top) shows the diffusion of electrons in velocity space as waves are induced. $\partial f / \partial v \rightarrow 0$ tending the distribtion towards a plateau. Different curves are plotted at different times with the higher energy particles (red) at the earliest times.

keV^{-1}]. The injected electron fluence in our model $\int_{-\infty}^{\infty} f(v,x,t)/v \, dx$ can be calculated from equations (2.15, 2.16) and is presented in Figure 2.9. The corresponding energy

spectral index of the injected electron fluence at the Sun is $\delta = (\alpha+1)/2$. The resulting spectrum of solar energetic particles at the Earth is also presented in Figure 2.9. The spectrum of energetic particles above a break energy (roughly 35 keV in Figure 2.9) is identical to the spectrum of injected electrons so we can deduce these particles have propagated scatter-free (at least in our model). The particles below the break energy do not propagate freely but generate electron Langmuir waves which flatten the spectrum of energetic particles. The beam generated Langmuir waves drift in velocity-space toward lower phase velocities due to the solar wind density gradient (Kontar 2001d). This drift, caused by the decreasing ambient plasma gradient, takes waves out of resonance with the particles that generated them and so reduces the wave energy at a given point in phase space. Particles arriving later to this point in phase space are unable to restore the injected spectrum because they cannot absorb the same amount of energy previously lost to the waves. Waves not re-absorbed by the electron beam are inevitably removed from the system through Landau damping, being absorbed by the background solar wind. It is this energy loss of the electron beam which is the direct cause of the fluence broken power-law spectra observed near the Earth.

2.4.2 Break energies and spectral indices

Although the spectrum below the break is not exactly a power-law it resembles one closely. To compare the results with observations we fitted our simulated spectra with simple power-law fits (example shown in Figure 2.9). The spectral index below the break energy (δ_{low}) is always smaller than the spectral index above the break energy (δ_{high}) and correlates (Figure 2.10) with δ_{high} in a remarkably similar manner to that observed by Krucker et al. (2009). The range of δ_{low}, however, appears in a rather narrow range between 2 and 2.5 for a wide range of injected spectral indices between 3 and 5 (Figure 2.10). The actual value of δ_{low} is also dependent on the background plasma density and will be different should the heliospheric density model change.

The break energy ranges for all simulations are between 4 keV and 80 keV (Figure 2.11), with the exact break energy being heavily dependent on the initial spectral index
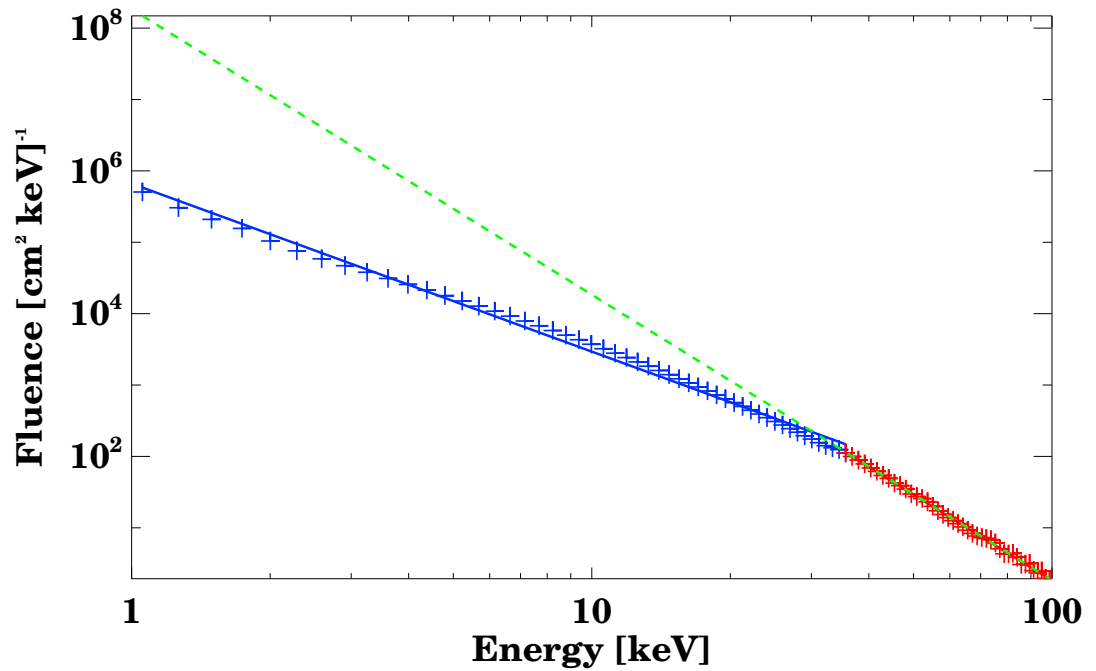
Figure 2.9: The spectrum (fluence [electrons cm^{-2} eV^{-1}]) of simulated solar flare energetic electrons at the Earth. The blue (red) line shows the power law fit to the spectrum below (above) the break energy. The green dashed line shows the initially injected fluence. The spectral index of injected electrons is 4. The spectral index below the break is 2.35

of the beam, δ_{high}, and the initial density of the beam. The density of beams influences the break energy, with higher density beams having higher break energies. Indeed, the larger the number of injected electrons, the faster the generation of Langmuir waves proceeds and hence the stronger the interaction between electrons and Langmuir waves. This also explains the dependence of break energy to the injected spectral index, with lower spectral indices having a larger population of higher energy electrons and hence having higher break energies. There is a positive correlation between the fluence at the break energy and the break energy itself (Figure 2.12) with higher break energies corresponding to lower fluence magnitudes.
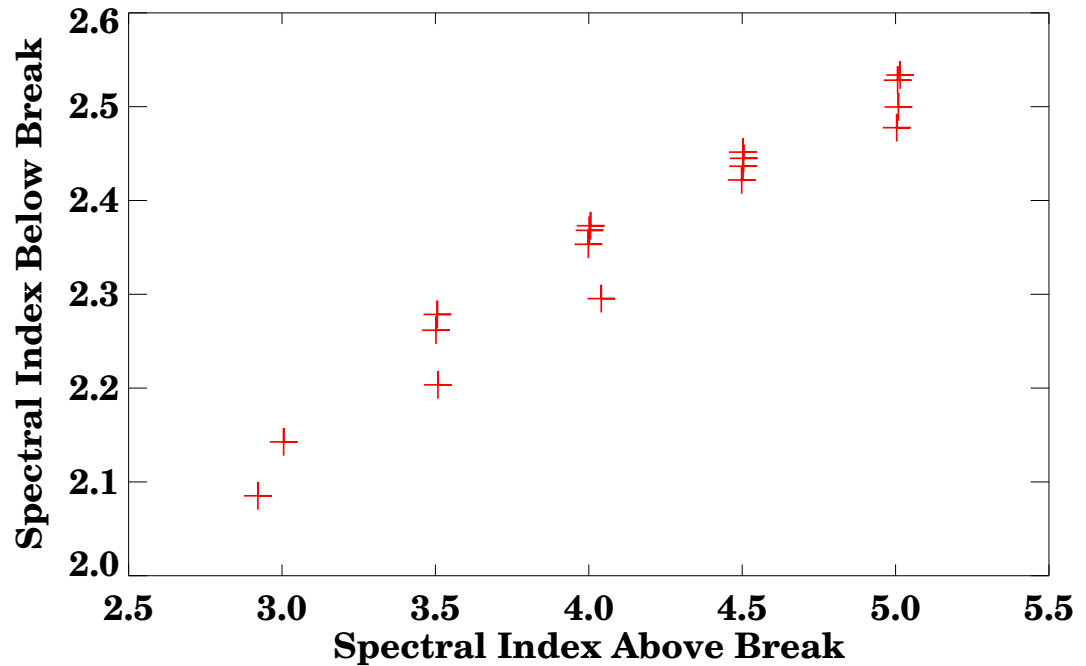
Figure 2.10: Spectral index below the break energy δ_{low} versus spectral index above the break energy.

2.4.3 Electron time-of-flight and apparent injection time

Particles arriving at the Earth (1.2 AU) show near time-of-flight dispersion (Figure 2.13), often observed by satellites in impulsive solar electron events (see Section 2.1.2). In our simulations only electrons above the break energy propagate freely and arrive on time whilst electrons below the break energy demonstrate early onset, i.e. seem as if they were injected earlier. Electrons below the break energy are losing and gaining energy during their transport via waves and hence do not propagate freely. Their time of arrival is also heavily dependent on the background plasma flux magnitude, with higher magnitudes obscuring the low flux of some high energy electrons which have relaxed to lower energies. The sawtooth structure appearing in low energy channels of Figure 2.13 is an unfortunate artefact of finite binning in the velocity space.

If we assume that the electrons arrive scatter-free, i.e. without any interaction with
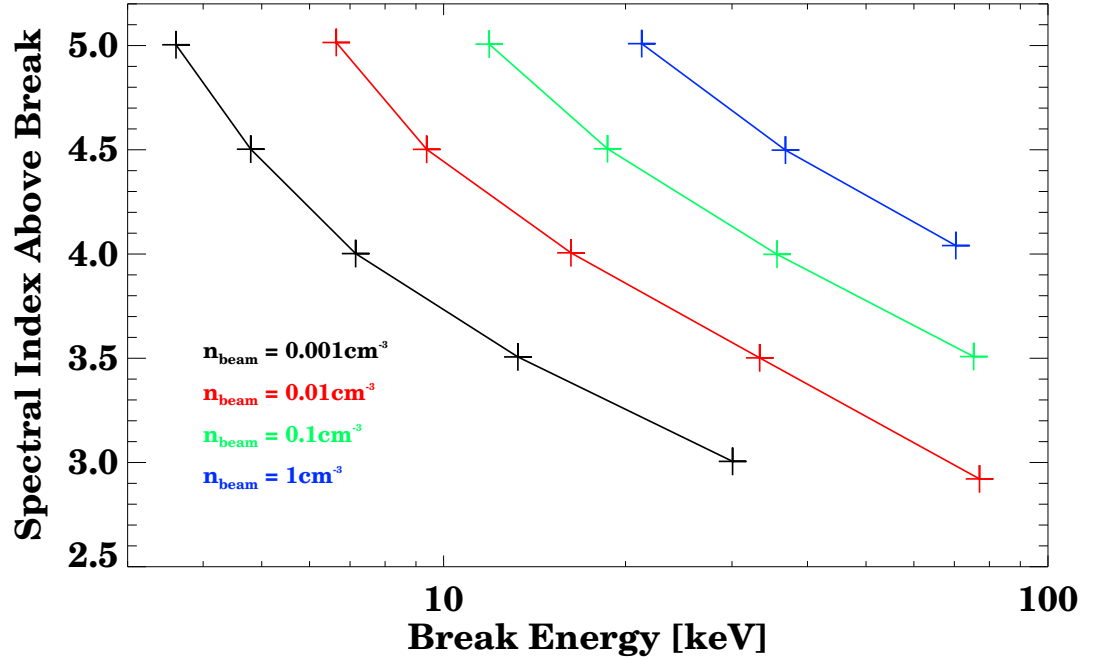
Figure 2.11: Spectral index above the break energy δ_{high} plotted against the energy at which the spectral break occurs. A variety of initial beam densities were used in the range 0.001 cm^{-3} $\leq n_b \leq 1$ cm^{-3}.

plasma, one can produce the apparent injection profile at the Sun, as Krucker et al. (1999); Wang et al. (2006) did for observations. These apparent injection profiles with simulated background added are presented in Figure 2.14. If the electrons propagate scatter-free they would require $10 - 20$ minutes earlier onset (t_{inj}) of low (3-12 keV) energy electron injection and a delayed maximum of the injection. As evident from the Figure (2.14), the onset of electron injection is also background dependent - the higher/lower background level would lead to later/earlier injection times for low energy electrons. An identical simulation was run with an electron beam not interacting with the background plasma and the results can be seen in Figure 2.14. There is clear agreement for injection times at high energies but this agreement deteriorates as the energy gets lower. This early injection time is a direct result of low-energy electron driven turbulence, which affects the propagation of electrons substantially. The low energy
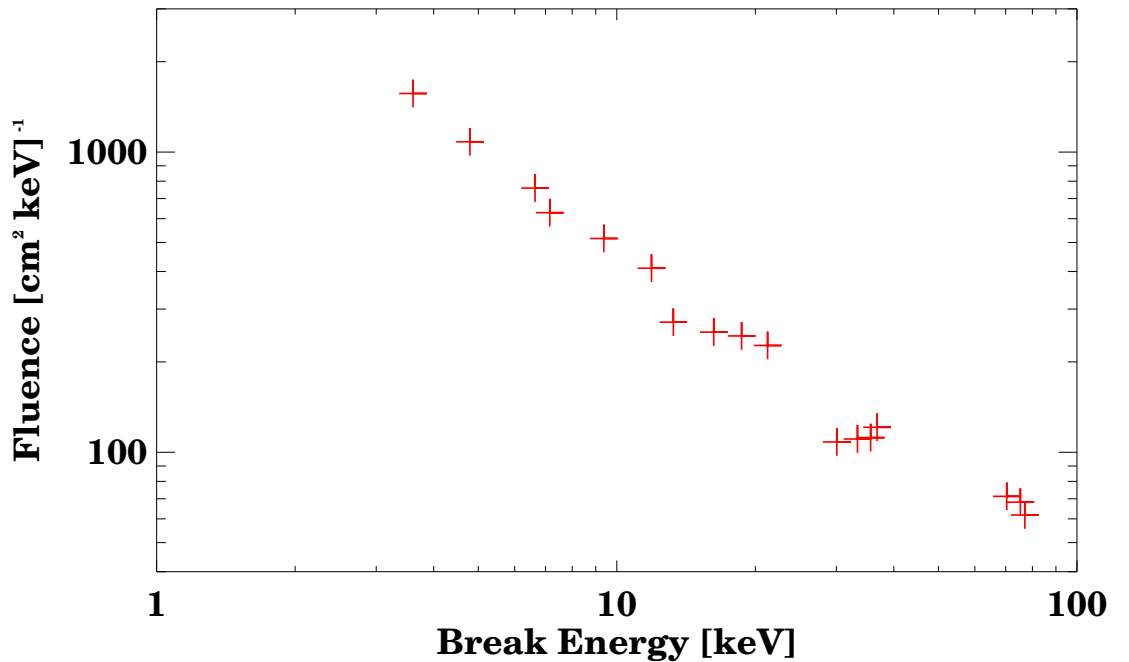
Figure 2.12: Fluence at the break energy versus break energy.

electrons can be observed not only via injection at the Sun but due to the in-flight deceleration of faster particles. The relaxation of the electron distribution function towards a flatter shape in velocity space $\partial f(v, x, t)/\partial v \sim 0$ means at a specific spatial location, some electrons have energies too low to have arrived by free propagation alone. Therefore, we believe that the similar injection profile obtained (Wang et al. 2006) should be interpreted as the direct evidence of electron plasma wave scattering in the heliosphere and not the indication of a separate acceleration mechanism.

2.5   Discussion and Conclusions

The generation and re-absorption of electron Langmuir waves by an electron beam in non-uniform plasma plays an important role in the electron transport and should be taken into account when in-situ electron measurements are analysed. The simulations presented here successfully reproduced the spectral and temporal characteristics of
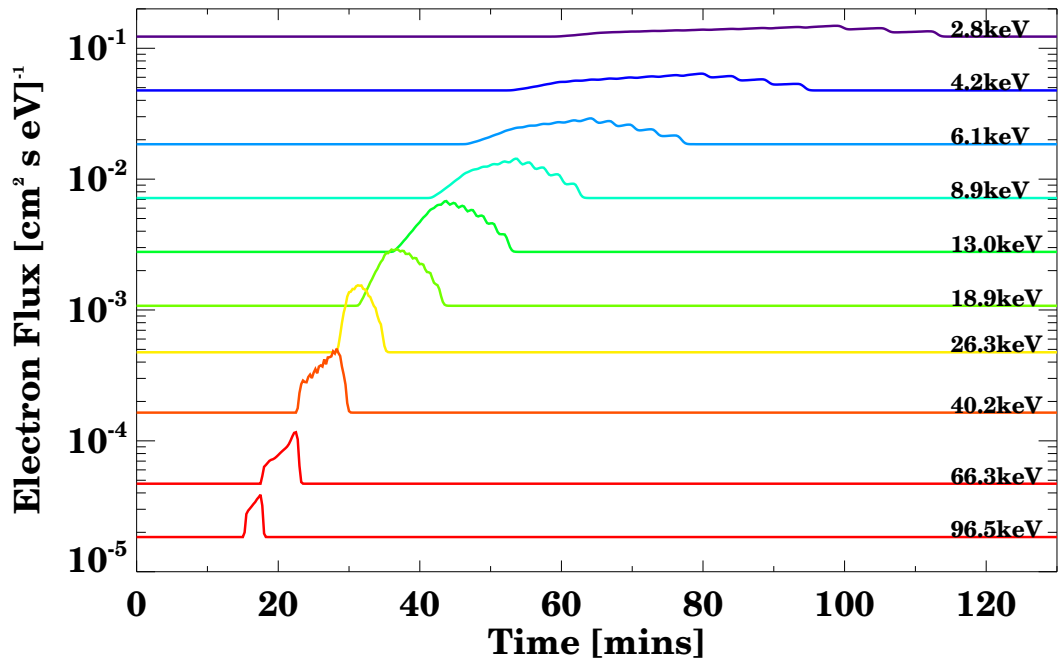
Figure 2.13: Simulated electron flux density time profiles of energetic electrons for wind/3DP energies. Electron flux density [electrons cm^{-2} s^{-1} eV^{-1}] as a function of time at 1.2 AU for 11 energy channels. The time $t = 0$ corresponds to the injection time at the Sun.

observed solar energetic electron events. The scattering of solar energetic particles by beam-driven electrostatic Langmuir waves leads to the appearance of a broken power-law in energy spectrum, and the apparent early injection of low energy electrons in the few keV range at the Sun.

These low energy electrons are originally injected with higher energies but have lost some energy to Langmuir waves in the background plasma and are therefore detected earlier than their energy at the spacecraft suggests. The apparent early start of low energy electron injection appears due to propagation effects and does not support the suggestion of a secondary beam postulated by Wang et al. (2006). The onsets of low energy electron data can be explained by propagation effects only.

The particle detectors in space normally measure electron flux density differential
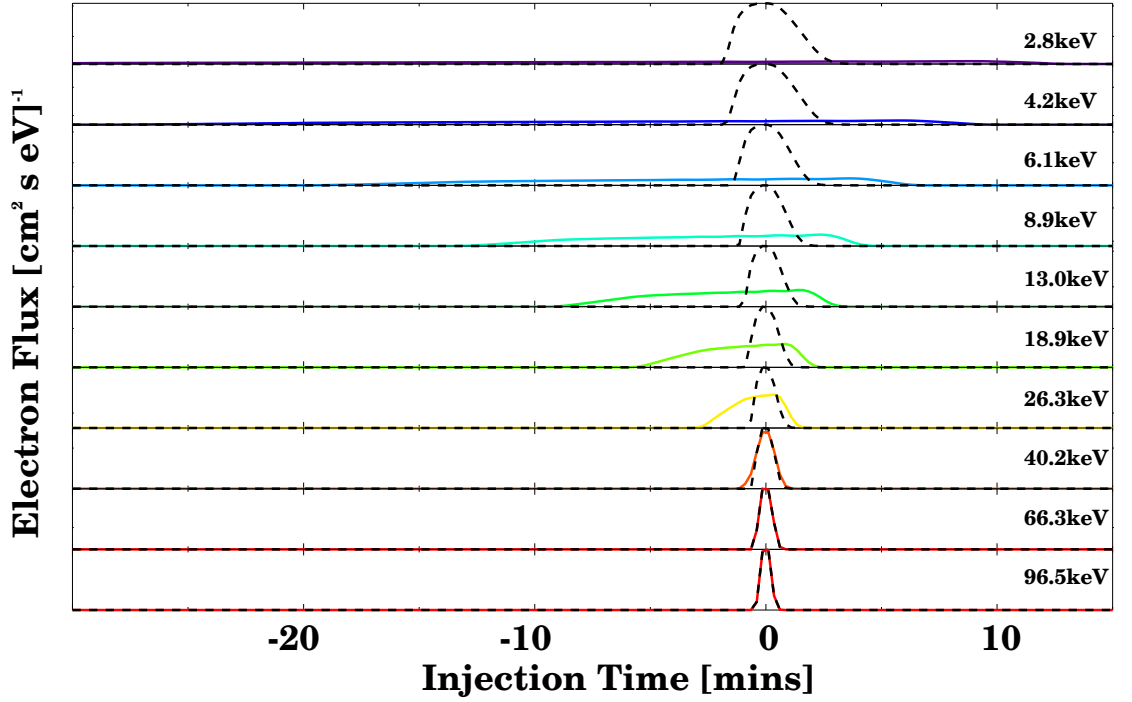
Figure 2.14: The apparent injection profile of electrons at the Sun assuming free streaming of all electrons. The true injection profile is overplotted with a dashed line.

in solid angle, while in our simulations we deal with one-dimensional distributions. To compare our simulated data with observations, one needs either to compute the reduced electron flux density integrated over the solid angle of the arriving electrons or assume the pitch-angle distribution in our simulations. For example, the 3-D Plasma and Energetic Particle (3DP) instrument on WIND (Lin et al. 1995) provides angular resolution of 22.5° and if solar energetic particles have an angular spread of 22.5°, the actual data from WIND needs to be multiplied by $\sim \pi(22.5/2)^2 = 0.11$.

The characteristic time of beam-plasma interaction via electron Langmuir waves is inversely proportional to the density of the energetic electrons. If the beam is dilute, electrons do not generate plasma turbulence and the spectrum of such electrons could be free from propagation effects. Such events are likely to be seen only at low energies. If the beam is dense enough to excite Langmuir waves, the initially injected power-law spectrum will be detected as a broken power-law. The break energy is dependent

on a number of parameters: spectral index of injected solar electrons, the density of the energetic electrons, and the heliospheric density model. Therefore, the correlation between break energy and fluence at the break energy should be made with care.

In addition, the heliospheric plasma has density perturbations on various scales that can affect the propagation of electrons (Melrose 1990; Kontar 2001c; Li et al. 2006b) and lead to a spiky structure of the Langmuir waves, often observed in the interplanetary space (Lin 1985). Therefore, additional simulations and in-situ measurements are needed to understand this complex non-linear system.

Another important process which should be included in the numerical simulations is radial expansion of magnetic field. Electrons guided by the magnetic field will diverge as the field radially diverges. Such behaviour will radially reduce the density of the electron beam. Modelling such a process will allow initial beam densities much higher than considered in this chapter. Higher beam densities should then correspond to Langmuir wave growth in the corona in line with expected results from type III observations. Moreover, the radial behaviour of the electron beam with respect to Langmuir wave growth will change.

Chapter 3

Electron beam and density turbulence

3.1 Motivation

In this chapter, we investigate the effects of background plasma density fluctuations on the generation and absorption of Langmuir waves from an energetic solar electron beam travelling from the Sun to the Earth. We demonstrate the dependence of Langmuir waves on the level of density fluctuations. We find high levels of density fluctuations damp Langmuir waves too much to be in accordance with detected type III radio emission. We also show how the level of density fluctuations has a direct effect on the spectral characteristics of the electron beam near the Earth.

3.1.1 Density turbulence in the inner heliosphere

The plasma of the solar corona and the solar wind is a non-uniform turbulent medium with density perturbations at various length scales. The structure of the solar wind density fluctuations has been analysed using scintillations of small-size radio sources (e.g. Hollweg 1970; Young 1971). Interplanetary scintillation is the temporal change of far away radio sources caused by density turbulence in the solar wind at spatial scales greater than 10-100 km (Coles & Harmon 1989; Manoharan et al. 1994). Scintillation

uses the intensity deviation $\delta I(t)$ of the instantaneous intensity $I(t)$ of the signal with the mean intensity $\langle I \rangle$ such that $\delta I(t) = I(t) - \langle I \rangle$. The statistical fluctuations of $\delta I(t)$ are used to probe the speed and density fluctuations of the solar wind integrated along the line of sight (e.g. Manoharan 2010). The turbulence spectrum can be obtained by taking the fourier transform of these fluctuations while the integral of this fourier transform is the r.m.s. intensity variations.

Interplanetary scintillation is used to probe density turbulence between the Sun and the Earth. At distances greater than 20 R_s the power density spectrum (turbulence spectrum) of the solar wind takes the form of a power-law with average spectral index near to the 5/3 Kolmogorov power spectrum. At distances less than 20 R_s the spectrum flattens to a spectral index nearer 1 (Woo & Armstrong 1979). This has been confirmed by other measurements (e.g. Coles & Harmon 1989; Coles et al. 1991; Manoharan 1993, 2010) which also found the power-law varied with the scale of the density turbulence. At very low frequencies $< 10^{-2}$ Hz the power-law has a Kolmogorov 5/3 profile. High frequencies > 1 Hz show the dissipative scale or inner scale (Coles 1978) where the spectrum steepens as the turbulence dissipates. In between these frequencies, the spectrum experiences a flattening. Frequency f is related to the size or wavelength λ of density inhomogeneities via the solar wind speed v_{sw} through $v_{sw} = f\lambda$. The frequencies arise because the inhomogeneous solar wind is blowing through the line of sight at speed v_{sw}. The solar wind speed varies from around 400 km s^{-1} in the slow solar wind to 700 km s^{-1} in the fast solar wind.

Scintillation techniques have also been used between the International Sun-Earth Explorer (ISEE) spacecraft ISEE2 and ISEE3 (Celnikier et al. 1987) to gain insight into the power spectrum of the solar wind at 1 AU. An example of one of the periods analysed can be seen in Figure 3.1. The Kolmogorov 5/3 power spectrum was found above 10^{-1} Hz, however, the spectral flattening was found below 10^{-1} Hz, in line with previous observations (Woo & Armstrong 1979)

In-situ measurements have been used to determine the density spectrum near the Earth and between 0.3 and 1 AU with *Helios* (Marsch & Tu 1990). The spectral slope at frequencies below 10^{-3} Hz were found to have a tendency to get smaller the closer
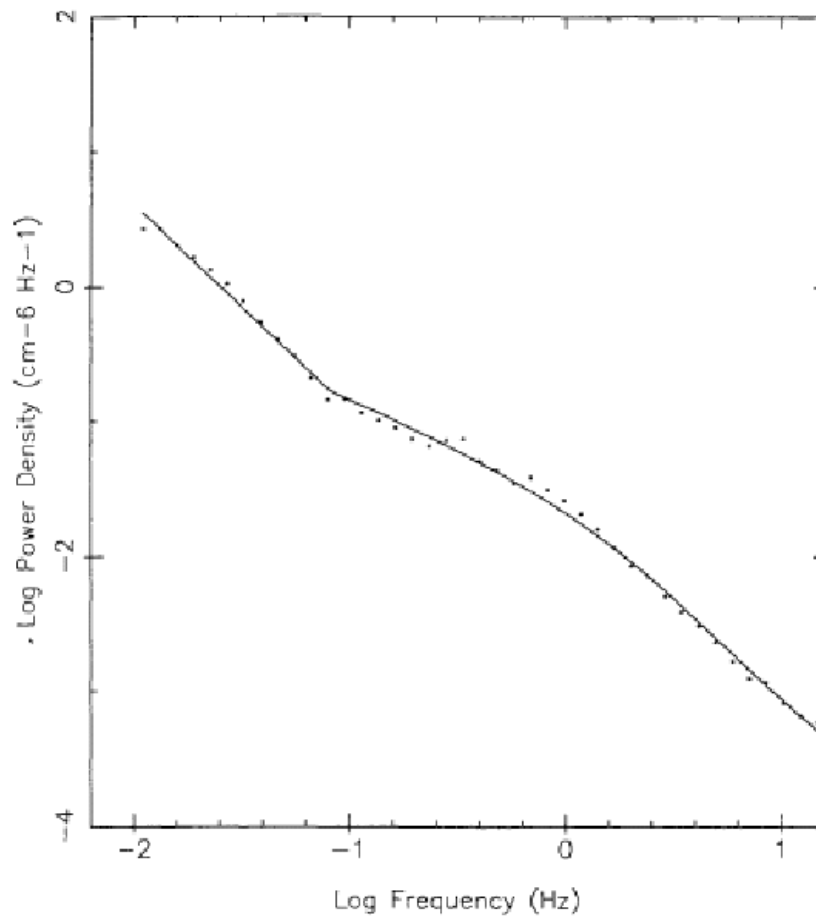
Figure 3.1: Log (spectral density) as a function of log (frequency) calculated using the maximum entropy technique; neighbouring frequencies have been averaged in such a way as to obtain a uniform distribution in log (frequency). The continuous line represents a least squares fit to the data assuming two power-laws, the higher frequency law being modified to take account of the line of sight averaging effect. (Celnikier et al. 1987).

the spacecraft got to the Sun in the fast solar wind. These results were further extended by Woo et al. (1995) using Ulysses remote sensing radio measurements for distances $< 40 \; R_s$ which predicted the decrease in r.m.s. deviation of the density turbulence in the fast solar wind at wavenumber $k = 1.4 \times 10^6 \; \text{km}^{-1}$. The results for the slow solar wind density turbulence (Marsch & Tu 1990; Woo et al. 1995) showed a constant
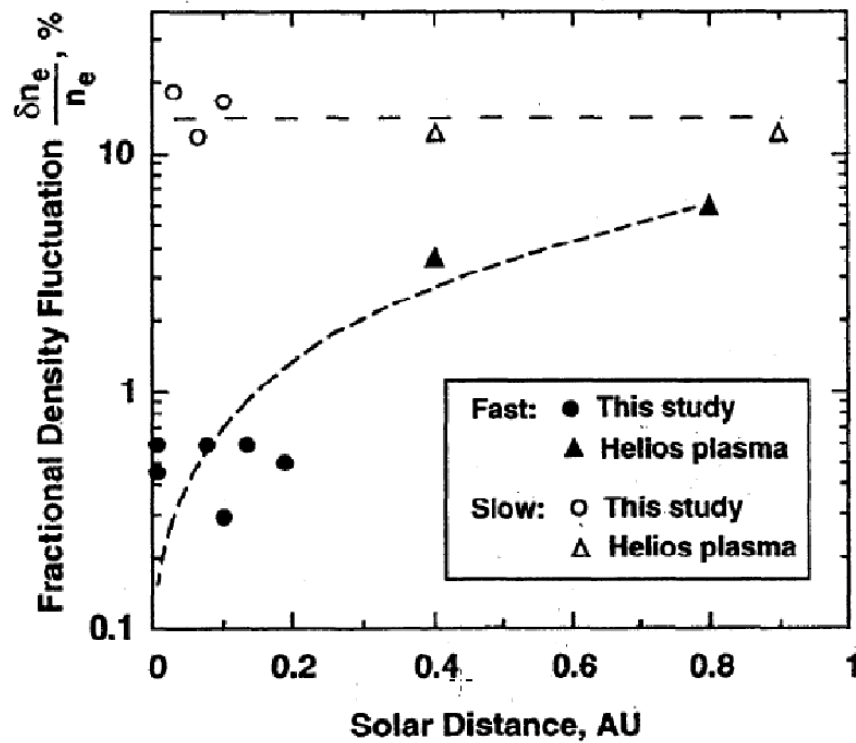
Figure 3.2: Fractional density fluctuations $\delta n_e/n_e$ for spatial wavenumber $k = 1.4 \times 10^6$ km^{-1}. Solid and hollow circles are Ulysses ranging measurements; solid and hollow triangles are Helios in-situ plasma measurements (Marsch & Tu 1990). Solid points are for fast wind and hollow points for slow wind. Dashed curve for the fast wind (far from the neutral line) is a quadratic fit to the data, while the dashed curve for the slow wind (near the neutral line) represents a constant (Woo et al. 1995).

level around 10 % which was also found in the later study from Spangler (2002). The results from Woo et al. (1995) are shown in Figure 3.2, giving an idea of how turbulent intensity can vary between the Sun and the Earth.

3.1.2 Density inhomogeneity and Langmuir waves

In-situ observations of Langmuir waves associated with type III radio bursts were first taken by Gurnett & Anderson (1976, 1977) using the Helios spacecraft at around
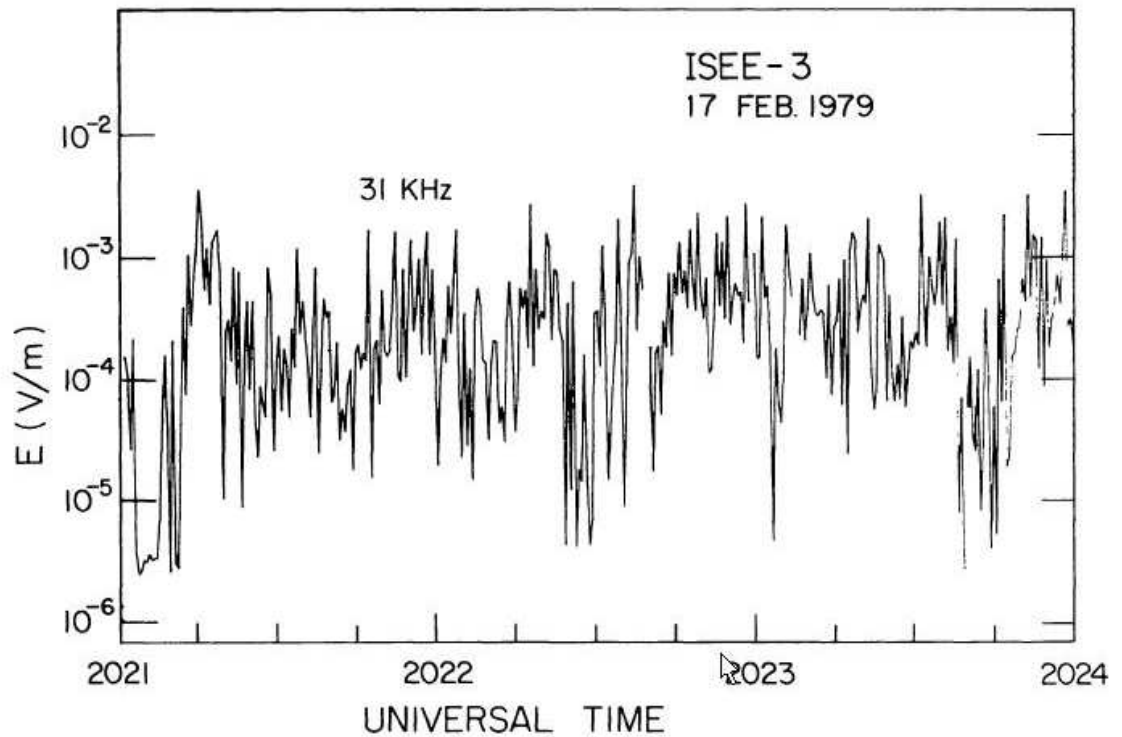
Figure 3.3: An expanded plot of the electric field in the 31 kHz channel with time resolution of 0.5 s near the maximum Langmuir wave intensity of an energetic electron beam observation. Note the extremely impulsive nature of the Langmuir waves. (Lin et al. 1981).

0.5 AU. They found that distribution of Langmuir waves is very clumpy in space. Observations at 1 AU came later using the ISEE-3 spacecraft (Lin et al. 1981). Figure 3.3 shows an example of Langmuir wave variation at 1 AU, revealing their rapidly changing time structure. The structure of the Langmuir waves suggests that it takes typically 1 s for a clump to pass the spacecraft implying 300-500 km scales for a solar wind speed of 300-500 km s^{-1}. There have been more recent observations of clumpy Langmuir waves that show similar properties (e.g. Kellogg et al. 2009).

To create this clumpy spectrum of Langmuir waves, there has to exist some process that damps the induction of Langmuir waves from an unstable electron beam.

It has been recognized (Ryutov 1969; Karpman & Istomin 1974) that beam-driven Langmuir waves can be effectively altered by even weak background density gradients. Density fluctuations are believed to suppress Langmuir wave growth (Smith & Sime 1979; Muschietti et al. 1985) and the popular belief is that they are responsible for the clumpy Langmuir wave distribution observed in-situ near the Earth. Therefore the effect of density fluctuations on beam-driven Langmuir waves responsible for type III radio bursts has been considered both numerically and analytically (e.g. Melrose et al. 1986; Robinson et al. 1992; Kontar 2001b).

The fluctuations, whilst changing the distribution of Langmuir waves significantly, have a rather weak modulating effect on the instantaneous distribution of electrons (Kontar 2001b). In the previous chapter, we have shown (Kontar & Reid 2009) that the electron beam-plasma interaction via Langmuir waves in the non-uniform solar corona leads to the appearance of a break energy in the observed spectrum at the Earth and can explain the observed apparent early injection of low-energy electrons. However, the net effect of density fluctuations in the solar wind on the electron spectrum detected near 1 AU has not been addressed before.

3.2 Electron Beam Transport Model

This chapter again focusses on the role of electron beam-driven electrostatic turbulence in the propagation and spectral evolution of energetic particles. The equations for evolving the electron beam through the inner heliosphere are similar to Equations (3.1, 3.2) but with more physical processes considered. The solar magnetic field expanding into the heliosphere quickly decreases with distance and provides adiabatic focussing for energetic electrons that ensures one dimensional (along expanding magnetic field lines) electron transport. This expansion of the magnetic field is simulated here with the distance of propagation now being described by r and not x. Thus the evolution of the electron distribution function $f(v, r, t)$ (the number density of energetic electrons is $n_b = \int f dv$ electrons cm^{-3}) and the spectral energy density of electron Langmuir waves $W(v, r, t)$ (the energy density of Langmuir waves is $\int W dk$ ergs cm^{-3}) in the

radially expanding magnetic field of the heliosphere can be described using the following equations of weak turbulence theory.

$$\frac{\partial f}{\partial t} + \frac{v}{(r+r_0)^2}\frac{\partial}{\partial r}(r+r_0)^2 f = \frac{4\pi^2 e^2}{m_e^2}\frac{\partial}{\partial v}\frac{W}{v}\frac{\partial f}{\partial v} + \frac{4\pi n_e e^4}{m_e^2}\ln\Lambda\frac{\partial}{\partial v}\frac{f}{v^2} \tag{3.1}$$

$$\frac{\partial W}{\partial t} + \frac{\partial\omega_L}{\partial k}\frac{\partial W}{\partial r} - \frac{\partial\omega_{pe}}{\partial r}\frac{\partial W}{\partial k} = \frac{\pi\omega_{pe}}{n_e}v^2 W\frac{\partial f}{\partial v} - (\gamma_c + \gamma_L)W + e^2\omega_{pe}(r)vf\ln\frac{v}{v_{Te}}. \tag{3.2}$$

Following Zheleznyakov & Zaitsev (1970); Takakura & Shibahashi (1976) we include collisional losses both for electrons and Langmuir waves. Similar to Equation (2.2) the collisional damping rate of Langmuir waves is described through γ_c (Section 2.2.1). The last term of Equation (3.1) accounts for electron collisional Coulomb losses in fully ionized hydrogen plasma (e.g. Emslie 1978). The electron Coulomb collisional term is proportional to background electron density n_e hence it will mainly affect the beam in the corona. Due to the Coulomb collisional v^{-3} dependence, the highest energy electrons > 50 keV will be minimally damped. Correspondingly, the lower energy electrons near the thermal velocity v_{Te} will experience a large damping rate before they leave the corona. The magnitude of the damping will depend upon the initial starting height of the electron beam.

The last term in Equation (3.2) is the spontaneous wave generation, which is similar to Zheleznyakov & Zaitsev (1970); Takakura & Shibahashi (1976); Hannah et al. (2009) but different from the terms used in Li et al. (2006b). The energy required for the spontaneous induction of Langmuir waves comes from the electron Coulomb collisional loss. The spontaneous generation of Langmuir waves is proportional to $f(v, r, t)$ and not to $W(v, r, t)$ so it will not grow larger when waves are induced through the bump-in-tail instability. It will be highest in the corona when the flux of electrons is the largest, more so where electrons have the lowest energies. We note that for large velocities ($v \gtrsim v_{Te}\sqrt{2\ln\Lambda}$) the energy loss of an electron to spontaneously generate Langmuir waves adopted by Li et al. (2006b) is greater than the electron collisional Coulomb losses in fully ionized hydrogen plasma (last term of Equation 3.1).

The second term on the left hand side of Equation (3.1) models magnetic field expansion from the solar corona into interplanetary space. This expansion in the corona is modelled through an expanding cone which has a radius d at the acceleration region and starts at length r_0 from the acceleration region. The 'origin' of the field cone $r_0 = 3 \times 10^9$ cm is chosen to have a cone expansion of 33.6^o. Such an expansion of an electron beam in the inner heliosphere is similar to observed values (Krucker et al. 2007) and similar to predicted type III source sizes (Steinberg et al. 1985). The heliospheric expansion conserves the total number of electrons such that for scatter-free propagation, $\int (r + r_0)^2 n(r) dr = $ const.

3.2.1 Electron beam initial conditions

The electron distribution function is modelled using an instantaneous electron injection which is Gaussian in space with a characteristic size d. This electron distribution has a power-law spectrum in velocity, and hence in energy, as often observed in solar flares (e.g. Brown & Kontar 2005). $f(v, r, t = 0)$ takes the form

$$f(v, r, t = 0) = \frac{n_b(\alpha - 1)}{v_{min}} \left(\frac{v_{min}}{v}\right)^{\alpha} \exp\left(-\frac{r^2}{d^2}\right). \tag{3.3}$$

The electron beam is normalised to the electron number density n_b. α represents the velocity spectral index where the spectral index in energy space $\delta = \alpha/2$. v_{min} represents the minimum velocity used for the electron beam.

The initial location of an electron beam ($r = 0$ in the above equations) for the subsequent simulations is taken at a background plasma frequency of 500 MHz which corresponds to the height of 3×10^9 cm^{-3} above the photosphere. This is often interpreted as the typical frequency/location for an electron beam acceleration site in the corona (Aschwanden et al. 1995a). The beam size was taken to be $d = 10^9$ cm.

The spectral index δ was set to 3.5, corresponding to typical spectral indices above the break energy of in-situ measured electron beams at the Earth (Krucker et al. 2009). Electron thermal velocity was taken to be $v_{Te} = 5.5 \times 10^8$ cm s^{-1}, which corresponds to Maxwellian plasma with a temperature of 1 MK. The beam velocities will range between 3.6 $v_{Te} \approx 2 \times 10^9$ cm s^{-1} and 2×10^{10} cm s^{-1}. Above the maximum velocity

relativistic effects become important. Langmuir waves created near thermal velocity are absorbed by the background Maxwellian through Landau damping so $3.6v_{Te}$ is an acceptable lower limit.

The initial electron beam density is taken to be 1.1×10^5 cm^{-3} which, together with $\delta = 3.5$, gives the total number of electrons above 50 keV of $1.2(\sqrt{\pi}d)^3 \approx 7 \times 10^{27}$. This is a relatively small event in relation to observed number of electrons above 50 keV (Krucker et al. 2007). The instantaneous injection of the electron beam restricts the total injected electrons to small event sizes to keep the flux of electrons around 100 keV near the Earth in line with typical values observed at 1 AU (Krucker et al. 2007, 2009). If we consider similar number densities at the peak of a temporal Gaussian injection of order 10^3 s, the total number of electrons rises to 10^{31}, in agreement with observations (Krucker et al. 2007).

Both the height and size of the electron beam are substantially smaller than previously simulated in Chapter 2. By modelling the radial expansion of the electron beam in the heliosphere the electron beam decreases its density as it propagates out through the heliosphere. The more realistic model allows for the high densities in the corona whilst giving realistic flux values near the Earth. Larger initial densities become numerically possible to simulate in a tractable amount of time. The size of the electron beam is thus able to be smaller whilst simulating more total electrons. A reduced initial electron beam size allows the beam to be injected into the corona at a lower height. The beam is now able to fit inside the corona and have densities which are comparable to real impulsive electron beams.

3.2.2 Background plasma parameters

The initial spectral energy density of the Langmuir waves is assumed to be at the thermal level

$$W(v, r, t = 0) = \frac{k_B T_e}{4\pi^2} \frac{\omega_{pe}(r)^2}{v^2} \log\left(\frac{v}{v_{Te}}\right) \tag{3.4}$$

where T_e is the background plasma temperature, k_B is Boltzmann constant and v_{Te} is the background electron thermal velocity. The thermal level is formed by setting

$dW/dt = 0$ for a Maxwellian distribution of electrons with temperature T_e and ignoring electron collisions in Equation (3.2). The major difference in this initial condition for the Langmuir waves over Section 2.2.2 is the dependence upon the phase velocity of waves. The magnitude of the thermal spectral energy density decreases as v increases for the velocity range we simulate. Lower thermal Langmuir wave magnitudes at higher velocities reduces the wave growth rate and the electron beam will have to travel slightly further before inducing a large magnitude of Langmuir waves.

The initial[1] background heliospheric plasma is modelled as a continuously decreasing background electron density. This is the same model in chapter 2, described through Equations (2.12, 2.13) and shown in Figure 2.5.

3.2.3   Numerical methods and code verification

The collisional term added in Equation (3.1) varies the distribution function in velocity space. It was thus solved using the upwind finite difference scheme mentioned in section 2.2.4. The first order collisional term was also checked against an analytical solution to see if an arbitrary distribution function would relax to a Maxwellian distribution. It conformed as well as a first order term would allow. It should be noted that the second order collisional term was not required because the background Maxwellian distribution was not modelled directly and $v_{min} \geq 2v_{Te}$.

The radial expansion of the magnetic field was able to be checked through the conservation of the number of particles (section 1.1.4). By removing all terms which caused a reduction in particle energy, the radial expansion could be checked against the analytical solution to see if particle number was conserved.

The number of particles which were considered in Chapter 2 was too low to be realistic of a type III producing electron beam. Such low numbers were required for numerical stability to provide computationally tractable code. The key term which is responsible for the numerical stability criteria in Equations (3.1) and (3.2) is the second order differential in Equation (3.1). The main variable (given adequate spatial,

---

[1]It will be perturbed later

temporal and velocity resolution) which constrains the time step required for numerical stability is the maximum magnitude of the Langmuir wave spectral energy density. A large number of particles induces a large magnitude of waves causing the simulation to be require more computational time.

The inclusion of a collisional term and a radial expansion term reduced the problem of generating a large magnitude of Langmuir waves by decreasing the number of particles in the system. Unfortunately this was not enough and computational time for realistic beam densities of around 10^4 cm^{-3} to reach the Earth was > 1 month. Further steps had to be taken to reduce this computational time to a reasonable magnitude.

A variable time step was introduced which monitors the maximum spectral energy density of Langmuir waves $W_{max}(t)$ in the simulation. A temporal constant t_{num} was initially calculated that is proportional to the quasilinear time at $t = 0, r = 0$ and the square of the velocity separation Δv^2. After every time step, Δt was calculated as $\Delta t = t_{num}/(16\pi W_{max}(t))$. The value of 16 ensured the time step was sufficiently below the value at which the simulations could become unstable.

The Fortran code was parallelised using MPI routines. To parallelise the code the spatial dimension of n_x points was split into n_p blocks where n_p was the number of processors being used. Each block consisted of $3 + n_x/n_p$ mesh points. Every processor was then able to computationally find the new values of f and W at $t + \Delta t$ for its block of points in parallel. After each timestep each processor would share information with the neighbouring processors about the first and last two rows of its block. This was required as for mesh point n the Van Leer finite difference method required knowledge of points n+1, n, n-1 and n-2. The parallelism allowed for a substantial computational speed up when used on the 16 core machines available.

The Fortran code implementing each term in Equations (3.1) and (3.2) were optimised to run faster. This involved calculating constants at the start of the program and saving them in memory rather than calculating them every timestep. Moreover, the command 'FORALL' was used when possible instead of 'DO' loops for its reduced runtime.

Whilst the quasilinear time and the maximum magnitude of the Langmuir wave

spectral energy density caused the timestep to be decreased, it did not have to be small for every term in Equations (3.1) and (3.2). Two separate timesteps were implemented, the quasilinear and the constant timestep. The quasilinear timestep was used to calculate the quasilinear term. The constant timestep (set at 2×10^{-3} s was then used to calculate all the other terms. Splitting the code this way not only allowed each timestep to be computed faster but meant the parallel computation between processors did not occur every quasilinear timestep when this timestep was very low (10^{-7} s at times). At initial points when the background electron density was high, the collisional damping of waves and spontaneous generation of waves had to be computed with a slightly lower timestep for stability.

All these new computational techniques allowed the code to finish in a timescale of the order of days when previously it would have taken weeks or months. Such methods allowed the exploration of electron beam and background electron density parameter space in a computationally tractable amount of time.

Further IDL routines had to be created for the analysis of the new data. Programs were written to compute the energy density of Langmuir waves and visualise it in an intuitive way. Additional programs were required to analytically test the new terms added in the chapter. Moreover, the density fluctuations used in this chapter were tested in IDL to make sure they created the correct power density spectrum in Fourier space.

3.3 Electron transport and density gradients

3.3.1 New transport model

As in Chapter 2 the initial electron distribution injected into the simulation is stable at $t = 0$ but once the electrons are allowed to propagate through space, the distribution quickly becomes unstable ($\partial f / \partial v > 0$) to Langmuir wave generation. As the growth rate of Langmuir waves is velocity dependent, the initial electron power-law distribution causes quasilinear relaxation to be important up to a certain velocity or corresponding

break energy. Above this energy electrons are too dilute to generate any Langmuir waves and travel scatter free (Section 2.4). Below this energy Langmuir waves are generated, relaxing the distribution function to a plateau in velocity space ($\partial f/\partial v \approx 0$) as energy from the electrons is transferred to the generated Langmuir waves. Such behaviour was seen in Section 2.4 near the Earth and observed in the resultant fluence spectrum.

The instability forms a beam-plasma structure (Mel'Nik 1995; Kontar et al. 1998), between the electron beam and the corresponding induced Langmuir waves seen in Figure 3.4. Figure 3.4 and subsequent figures in this chapter are taken from (Reid & Kontar 2010). High beam densities of 10^4 cm^{-3} now cause electrons to generate Langmuir waves in the corona. This increased initial beam density[2] relative to previous simulations increases the maximum velocity in the corona making wave-particle interactions important. In contrast to Figure 2.7 Langmuir waves are generated up to $25v/v_{Te}$ or 50 keV within the first 25 seconds. The corresponding broadening of the electron flux as electrons lose energy to Langmuir waves and diffuse down in velocity space can also be seen.

Another major difference between Figure 3.4 and previous simulations is the radial decrease in the maximum energy that undergoes significant wave-particle interactions. Radial expansion of the magnetic field, simulated through the second term in Equation (3.1), reduces the electron beam density during propagation from the Sun to the Earth. The Langmuir wave growth rate $\gamma(v,x) = \frac{\pi \omega_{pe}}{n_e} v^2 W \frac{\partial f}{\partial v}$ decreases faster from a smaller beam density than it increases from the radial decrease of background density n_e. The maximum velocity of electrons that induces Langmuir waves through the bump-in-tail instability decreases as the beam propagates towards the Earth. Consequently, the reduction in fluence around the break energy observed near the Earth occurs near the Sun. This result is in line with previous observations (e.g. Lin et al. 1981) near the Earth where Langmuir waves are detected with the onset of $\lesssim 10$ keV electrons.

The low level of wave energy density $\lesssim 10^2$ W/W$_{\text{Th}}$ above 25 v/v_{Te} is caused

---

[2]We shall see in Chapter 4 that reducing either the characteristic size of the electron beam or the electron beam spectral index greatly adds to this effect
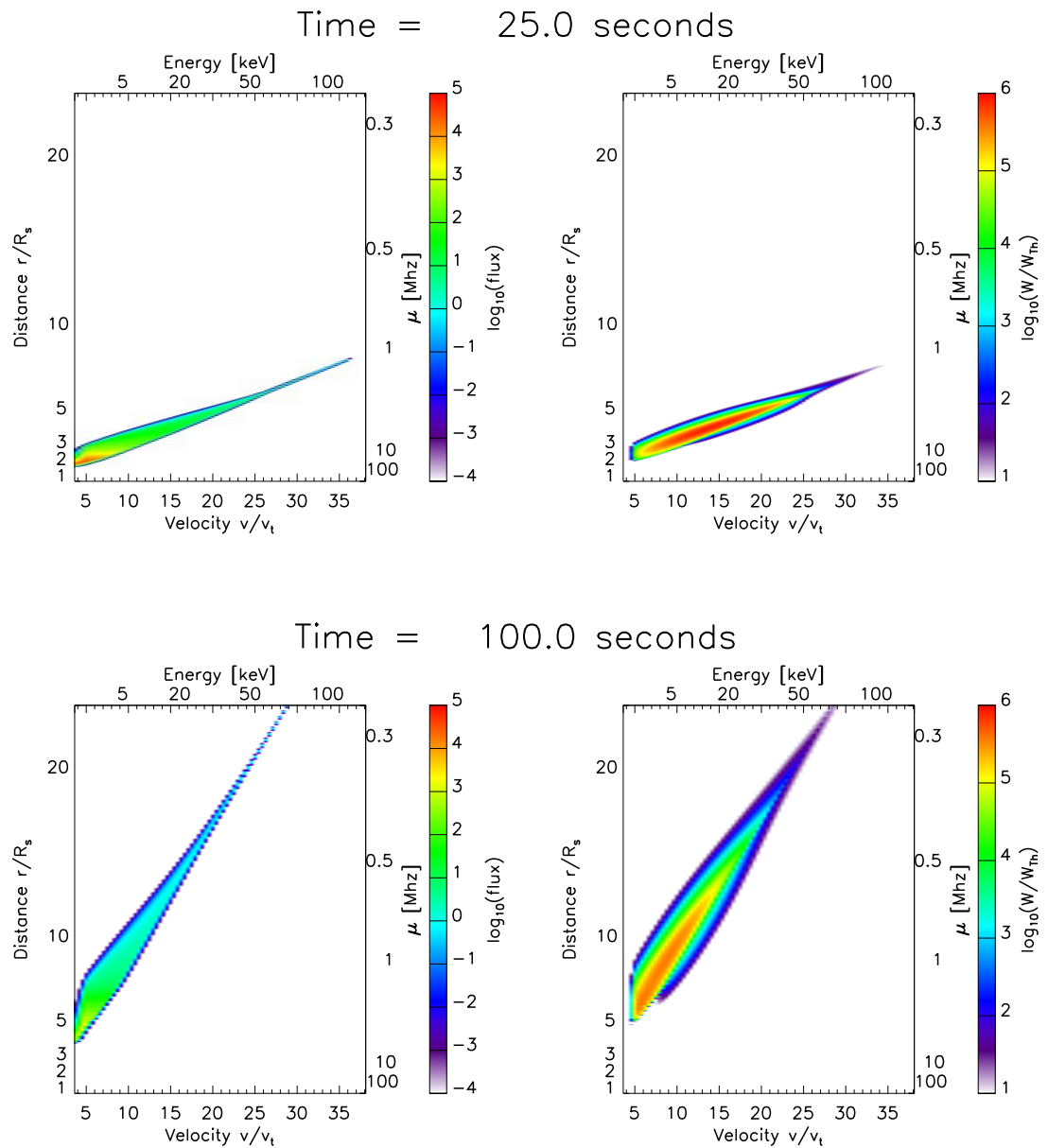
Figure 3.4: Colour coded plot of the electron flux $[\text{cm}^2 \text{ eV s}]^{-1}$ and spectral energy density (normalised by thermal level $W(v, r, t = 0)$) of Langmuir waves for two moments in time. Distance and velocity are normalised by solar radii and thermal velocity respectively. The background plasma density is unperturbed.

by spontaneous generation from high energy electrons and not by the bump-in-tail instability. As such, no diffusion of electrons in velocity space can be observed.

3.3.2   Sinusoidal background density fluctuations

Initially we considered a simplified model for the background electron density. The real inner heliosphere electron density is more complex, with fluctuations present at scales smaller than 1 AU. To explore density fluctuations, a simple perturbation of the background plasma is added to the previous heliospheric density model in the form of a sinusoid. The new background density

$$n_e(r) = n_{e0}(r)[1 + \Upsilon \sin(2\pi r/\lambda)] \qquad (3.5)$$

where Υ and λ are the amplitude and wavelength of the perturbation respectively and n_{e0} is the original unperturbed density. The initial value of the amplitude Υ is taken as 10^{-2} while the wavelength λ is taken as 10^{10} cm. These values create a perturbation which is within reasonable solar wind parameters (Celnikier et al. 1983).

Distributions close to the Sun

Close to the Sun the initial unperturbed radial decrease of background electron density plays the dominant role in density change. The small-scale fluctuations (from the sinusoid) are thus unable to generate any positive density gradients. The drift of waves in velocity space is always to lower phase velocities, as can be observed at the earlier time interval $t = 25$ s (Figure 3.5). The density fluctuations cause an increase or decrease in this drift of Langmuir waves to lower phase velocities. As the growth rate of Langmuir waves depends linearly upon the magnitude of Langmuir waves at any point in phase space, if the plasma inhomogeneity is too large then Langmuir wave production is suppressed (in line with Smith & Sime 1979; Muschietti et al. 1985; Kontar 2001b; Ledenev et al. 2004; Li et al. 2006b).

To compare the background plasma inhomogeneity with the level of Langmuir waves
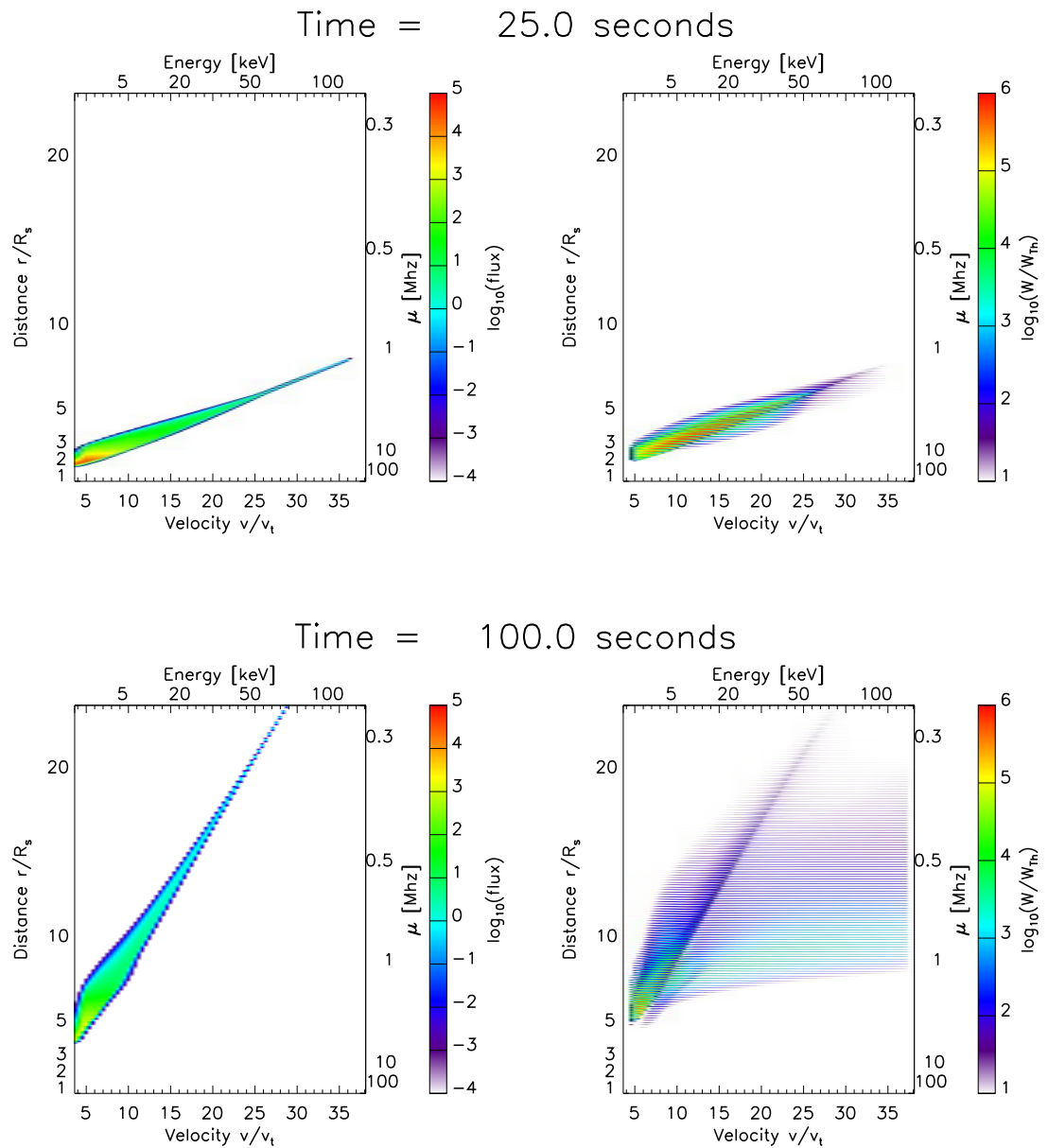
Figure 3.5: Colour coded plot of the electron flux $[\text{cm}^2 \text{ eV s}]^{-1}$ and spectral energy density (normalised by thermal level $W(v, r, t = 0)$) of Langmuir waves for two moments in time. Distance and velocity are normalised by solar radii and thermal velocity respectively. The background plasma density has been perturbed with a sine wave.

in any spatial location we consider the magnitude of wave energy density, found by

$$E_w(r,t) = \int_0^\infty W dk = \omega_{pe} \int_{v_{min}}^{v_{max}} \frac{W(v,r,t)}{v^2} dv. \tag{3.6}$$

The Langmuir wave energy density, $E_w(r,t)$, close to the Sun at time $t = 25$ s is displayed in Figure 3.6 with the corresponding scale of the background plasma inhomogeneity. The unperturbed case has been over plotted for comparison. Lines have been drawn to indicate the 10^{10} cm wavelength of sinusoid perturbation to the background plasma. Periodic oscillation of the background plasma is evident together with the corresponding periodic nature of the Langmuir wave energy density. The magnitude of $E_w(r,t)$ in the unperturbed case is generally larger than the perturbed case, showing clearly the reduction in wave growth when the background plasma is significantly perturbed. As we get further away from the Sun (5 R_s compared with 2 R_s) the initial unperturbed radial drop of density plays a less dominant role allowing small-scale fluctuations to become more important, seen in $|L|^{-1}$. With this increased role, the small-scale fluctuations increase the suppression of induced Langmuir wave energy density with respect to the unperturbed case.

Despite fluctuations suppressing Langmuir waves, the perturbed case displays Langmuir wave energy density greater than the unperturbed case at peaks in its oscillation. The bump-in-tail instability that induces Langmuir waves does not fully relax to thermal velocities in areas of space where Langmuir wave production is suppressed. Another striking feature of Figure 3.6 is the double peak and trough behaviour of $E_w(r,t)$ within one wavelength of background plasma fluctuation.

The distribution of $E_w(r,t)$ in space is substantially different at the latter time of $t = 100$ s, shown in Figure 3.6. There is a larger discrepancy in magnitude between the unperturbed and perturbed case. Moreover, the second peak of $E_w(r,t)$ within one wavelength clearly seen at $t = 25$ s is suppressed at the later time of $t = 100$ s. The one remaining pronounced peak does not stay co-spatial with the small-scale fluctuation wavelength but shifts backwards with respect to increasing distance from the Sun for this single point in time. Density fluctuations at distances $\approx 7R_s$ become influential enough over the radial density decrease to generate some positive background density
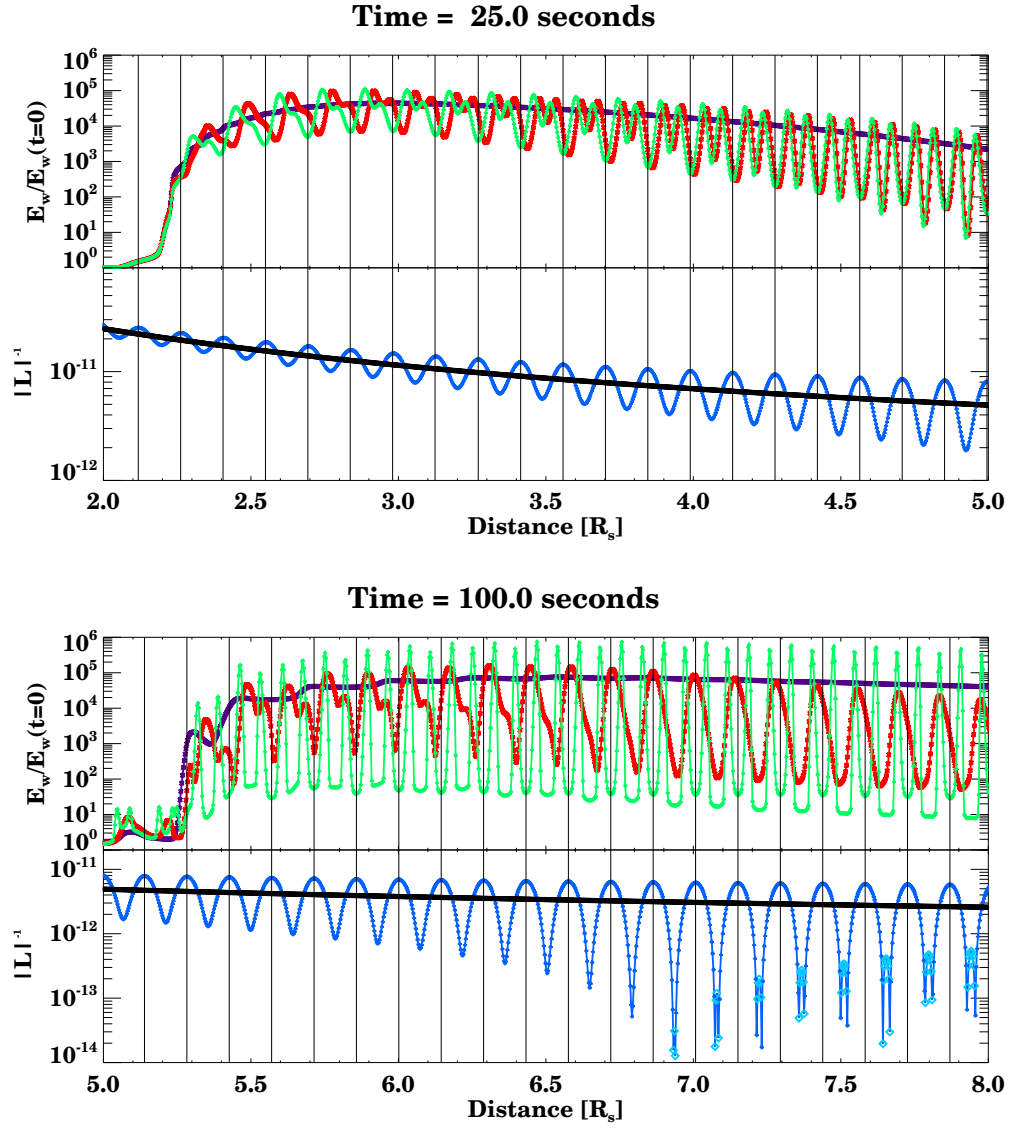
Figure 3.6: The Langmuir wave energy density $E_w(r)$ at two different times for background plasma which is unperturbed (purple), perturbed by a sine wave described by Equation 3.5 (red) and perturbed without implementing group velocity (green). The corresponding magnitude of plasma inhomogeneity $|L|^{-1}$ for unperturbed (black) and perturbed (blue) is plotted for comparison. The light blue diamonds are where the plasma inhomogeneity is positive in magnitude.

gradients. A positive gradient causes Langmuir waves to move to higher phase velocities and causes the streaking seen at $t = 100$ s in Figure 3.5. Despite the Langmuir wave distribution being substantially different, the electron flux remains almost unchanged, agreeing with the numerical results from Kontar (2001b).

The role of Langmuir wave group velocity

The group velocity of Langmuir waves $v_g \approx 3v_{Te}^2/v$ lies in the range $4 \times 10^7 \leq v_g \leq 4 \times 10^8$ cm s^{-1} which is small in magnitude compared to characteristic electron beam velocities. At $t = 25$ s (Figure 3.6) the removal of the group velocity term has minimal effect. Waves are moved in space by a small distance dependent upon the magnitude of the group velocity. The slower energetic electrons produce waves with higher group velocity and hence the wave energy density is displaced further.

At the later time of $t = 100$ s, $E_w(r, t)$ is substantially different when the group velocity term is not present, as seen in Figure 3.6. There is a clear double peak and trough behaviour within one background density fluctuation wavelength. Without any group velocity, waves are unable to travel from points in space where the background density structure favours wave growth to points where wave growth is suppressed. The simulation with no group velocity also has a higher magnitude of wave energy density at its peaks than both the other simulations.

The group velocity of Langmuir waves, despite being small, acts to move wave energy from points in space where Langmuir waves are strongly induced to points in space where they are suppressed. This has a spatial smoothing effect on the induced Langmuir wave energy density.

Amplitude of fluctuations

The amplitude Υ of the density fluctuations directly varies the background electron plasma density. The magnitude of this factor near the Earth can be found from observational results. It has been measured using the International Sun-Earth Explorer (ISEE) (Harvey et al. 1978) propagation experiment with scintillation techniques

(Celnikier et al. 1983) that the background electron plasma density near the Earth varies by about 10%. This would give the amplitude of $\Upsilon \leq 0.1$. Therefore we consider Υ in the range $10^{-3} \leq \Upsilon \leq 10^{-1}$. The wavelength of the perturbation remains at $\lambda = 10^{10}$ cm.

As Υ increases in magnitude, the oscillation in wave energy density increases. Similarly as Υ decreases in magnitude, the oscillations in wave energy density decrease such that as $\Upsilon \rightarrow 0$ the wave energy density tends to the state where no perturbations are present in the background electron plasma density. This can be seen in Figure 3.7 in the plasma inhomogeneity, $|L|^{-1}$. As Υ decreases to 10^{-3}, the plasma inhomogeneity does not vary as much and L remains negative for all r.

The variation of Υ in Figure 3.7 shows how the magnitude of the plasma inhomogeneity affects wave generation. If the fluctuations are too large, Langmuir waves drift in phase velocity too fast from the beam and are unable to build up. This suppression can clearly be seen when $\Upsilon = 10^{-1}$. Most spatial areas have large values of $|L|^{-1}$ and corresponding low values of wave energy density. Conversely, when $\Upsilon = 10^{-3}$, the small-scale fluctuations are small and wave energy density is able to build up to high magnitudes. This suppression agrees with previous theoretical (Melrose 1982; Melrose et al. 1986) and numerical work on Langmuir wave generation in non-uniform plasma (Kontar 2001b).

Wavelength of perturbations

The wavelength of density fluctuations λ has a strong effect on the local scale of plasma inhomogeneity, L, through dn_e/dr having one term inversely proportional to λ. Density fluctuations have been measured at a variety of different length scales from 10^{12} cm down to 10^6 cm (Neugebauer et al. 1978; Celnikier et al. 1987; Kellogg et al. 2009). We have varied λ in the range 10^9 cm $\leq \lambda \leq 10^{11}$ cm which is close to the range of fluctuations presented by Celnikier et al. (1987). The amplitude was set to $\Upsilon = 10^{-2}$, similar to the previous section for comparison reasons.

As λ increases in magnitude, the oscillation in density inhomogeneity decreases such

that as $\lambda \to \infty$, the wave energy density tends to the state where no perturbations are present in the background electron plasma density. This can be seen from Figure 3.8 in the case where $\lambda = 10^{11}$ cm and the density inhomogeneity is very smooth. Conversely, as λ decreases, the magnitude of L^{-1} increases while the sign of L^{-1} fluctuates rapidly.

We can see from Figure 3.8 that when λ is large, the induced Langmuir wave energy density resembles the unperturbed case. When λ is small, the large magnitude of L^{-1} causes waves to shift in velocity space faster. At any spatial point waves are present with a far greater range of phase velocities, however, their magnitude is much decreased. This means there exists a decreased level of Langmuir waves at points in phase space where the electron beam is present. The growth factor of Langmuir waves, responsible in the kinetic equations for converting electron beam energy to Langmuir wave energy, is proportional to the level of Langmuir waves. The decreased level of Langmuir waves in areas of phase space where the electron beam is present causes less energy to be transferred from electron beam to Langmuir wave and is the reason for the smaller wave energy density observed in Figure 3.8 when $\lambda = 10^9$ cm.

3.3.3 Power-law background density fluctuations

The power spectrum of density fluctuations observed in the solar wind density follows a simple, Kolmogorov type power law near the Earth with spectral index near to 5/3. A similar spectrum index of perturbations has been observed both with scintillation techniques (Celnikier et al. 1983, 1987) and with in-situ measurements (Neugebauer et al. 1978; Kellogg & Horbury 2005). The spectrum has been observed to steepen at small wavenumbers around 10^8 cm. To model small-scale density fluctuations many perturbations of the background plasma are introduced, so the density is

$$n_e(r) = n_{e0}(r) \left[1 + C \sum_{n=1}^{N} \lambda_n^{\beta/2} sin(2\pi r/\lambda_n + \phi_n) \right] \qquad (3.7)$$

for N perturbations where $n_{e0}(r)$ is the original unperturbed density. λ_n are the wavelengths of density perturbations with ϕ_n as their random phase. C is a constant which
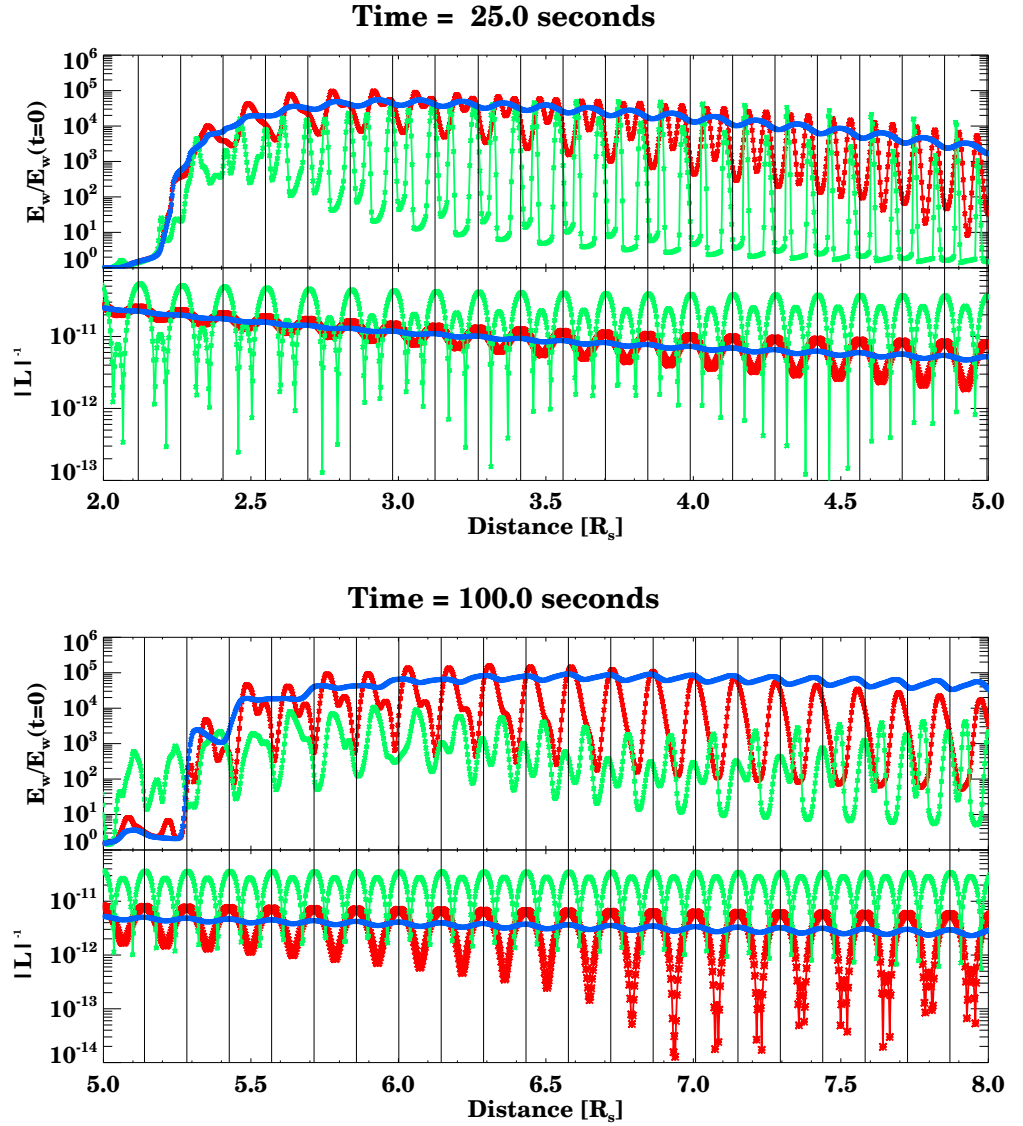
Figure 3.7: Wave energy density of Langmuir waves for $\Upsilon = 10^{-1}$ (green), 10^{-2} (red), 10^{-3} (blue). $\lambda = 10^{10}$ cm. The background plasma inhomogeneity $L(r)$ for each simulation in the appropriate colour is shown in lower panels.

normalises the density fluctuations given by

$$C = \sqrt{\frac{2\langle \Delta n_e(r)^2 \rangle}{\langle n_e(r) \rangle^2 \sum_{n=1}^{N} \lambda_n^{\beta}}} \tag{3.8}$$

where $\langle n_e(r) \rangle$ is the mean density. The root mean squared deviation of the density, $\sqrt{\langle \Delta n_e(r)^2 \rangle}$, from observational values near the Earth was taken to be 0.4 cm^{-3} or
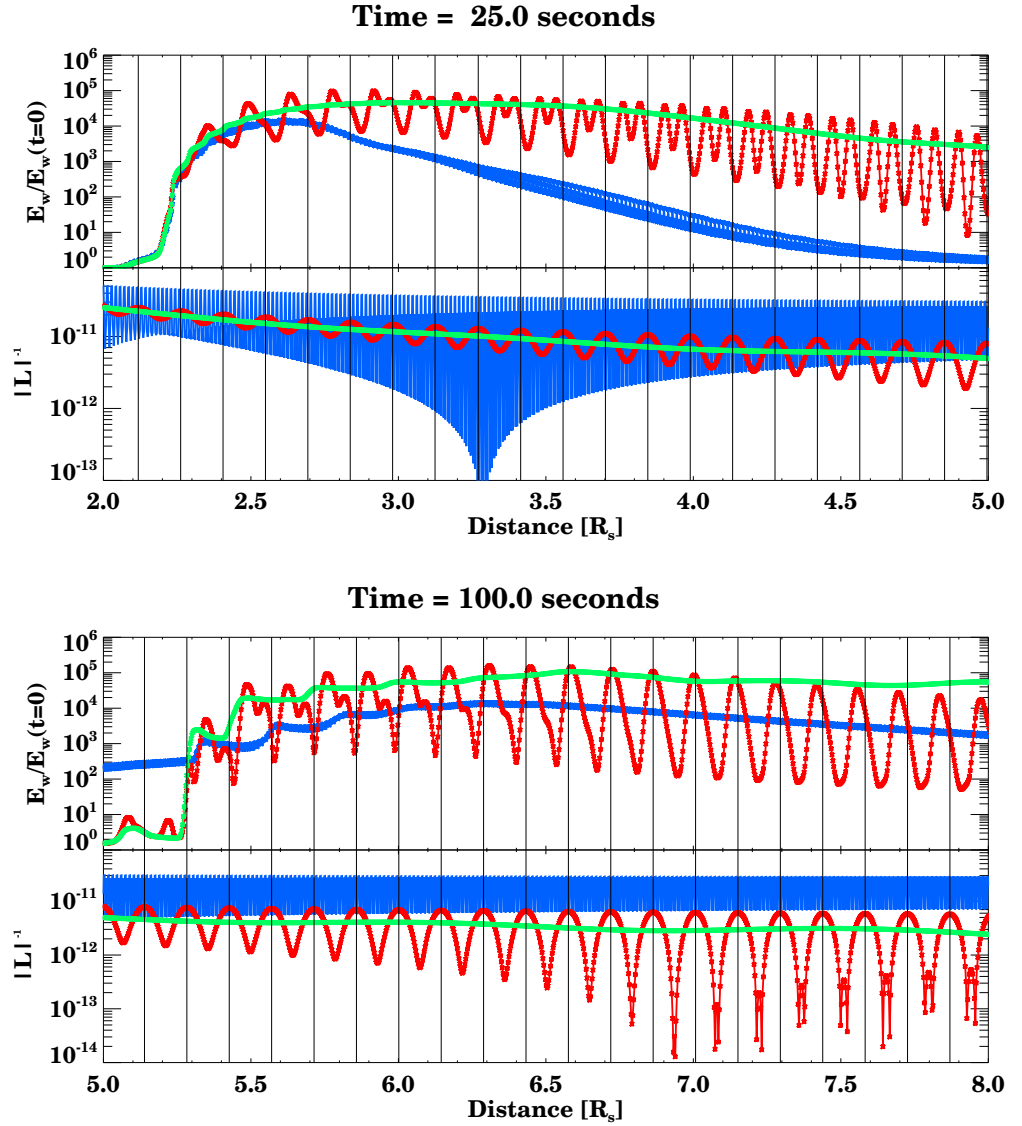
Figure 3.8: Wave energy density for $\lambda = 10^{11}$ cm(green), 10^{10} cm(red), 10^9 cm(blue). $\Upsilon = 10^{-2}$. The background plasma inhomogeneity $L(r)$ for each simulation in the appropriate colour is shown in lower panels.

10% of the mean density. The quantity $\sqrt{\frac{\langle \Delta n_e(r)^2 \rangle}{\langle n_e(r) \rangle^2}}$, the fractional density fluctuations, is a measure of the turbulent intensity of the background plasma. From Equation 3.8 this quantity is radially independent, giving a constant turbulent intensity from the

Sun to the Earth. We can then model the radial variation of turbulent intensity with

$$\sqrt{\frac{\langle \Delta n_e(r)^2 \rangle}{\langle n_e(r) \rangle^2}} = \left(\frac{n_{e0}(1AU)}{n_{e0}(r)} \right)^{\psi} \sqrt{\frac{\langle \Delta n_e(r_{1AU})^2 \rangle}{\langle n_e(r_{1AU}) \rangle^2}} \tag{3.9}$$

where $\psi \geq 0$ determines the degree at which the density fluctuations become less dominant from the Sun to the Earth (larger values of ψ correspond to turbulent intensity near the Sun). $\psi = 0$ corresponding to no radial variation. We do not consider $\psi \leq 0$ which corresponds to density fluctuations decreasing in intensity from the Sun to the Earth. For simplicity, we will reference the fractional density fluctuations as $\Delta n_e/n_e$. We considered the range of λ to be 10^7 cm $\leq \lambda \leq 10^{10}$ cm which is within the inertial range of solar wind turbulence. Larger values of λ have a minor effect and the amplitude of waves shorter than $\lambda \approx 10^7$ cm is small. The random phases $0 \leq \phi < 2\pi$ ensure the amplitudes of density fluctuations have a Gaussian distribution.

A constant level of $\Delta n_e/n_e$ throughout the inner heliosphere is found by setting $\psi = 0$. We set $\Delta n_e/n_e = 10\%$ which is within the observed range of values near the Earth (Celnikier et al. 1987). Figure 3.9 shows the density inhomogeneity and corresponding Langmuir wave energy density close to the Sun. The high level of inhomogeneity caused by the small-scale fluctuations greatly suppresses Langmuir wave spatial build-up compared to the unperturbed case. Suppression of Langmuir waves for $\Delta n_e/n_e = 10\%$ close to the Sun can prevent the high level of Langmuir waves required for type III solar radio emission. Such suppression is inconsistent with observations as type III emission is observed at frequencies > 100 MHz.

To vary the level of fluctuations from the Sun to the Earth, we set $\psi > 0$. Figure 3.9 shows the density inhomogeneity and corresponding Langmuir wave energy density close to the Sun with $\Delta n_e/n_e = 10\%$ at 1 AU and $\psi = 0.5$. Comparing the Langmuir wave energy density with the earlier simulations which assumed constant $\Delta n_e/n_e$, we can see a much larger magnitude of Langmuir wave energy density being induced from the electron beam. The reduced contribution from the small-scale fluctuations allows build up of Langmuir wave energy density. This high level of wave energy density is required to see the recorded brightness temperatures associated with type III radio emission. Moreover, the spatial spread of Langmuir waves is much less sporadic than

the produced level of wave energy density in the simulation with high level of fluctuations. The electron beam and Langmuir wave distribution can be seen in Figure 3.10. Langmuir waves are no longer perturbed in a periodic fashion but are pseudo-random in space. The pseudo-random nature of the spikes in Langmuir wave energy density leads to similar clumpy behaviour of Langmuir waves observed in-situ by spacecrafts (e.g. Gurnett & Anderson 1976).

3.4 Electron spectra near the Earth

The previous chapter (see also Kontar & Reid 2009) has shown the generation and absorption of Langmuir waves coupled with the effect of the background plasma inhomogeneity can change the electron beam energy distribution. A broken power-law in fluence spectrum can be formed from an initially single power-law distribution. The break at which the two power-laws connect is at the maximum velocity that electrons are able to induce significant levels of Langmuir waves above the thermal level via the bump-in-tail instability. The spectrum below the break is flattened during transport because the electron beam is unable to re-absorb all the energy transferred to Langmuir waves due to background plasma density gradients.

Introducing small-scale density fluctuations into the background plasma changes its properties and should consequently change the spectrum of the electron distribution function. Whilst changes in the electron spectrum are not visible on short scales (a few relaxation times), the fluence spectrum at the Earth shows a noticeable dependence upon the level of fluctuations introduced into the simulation. Figure 3.11 shows the fluence spectrum of the electron beam at the Earth for five different amplitudes of fluctuation within the range $10^{-3} \leq \Upsilon \leq 10^{-1}$. As shown earlier, the small-scale density fluctuations suppress the generation of Langmuir waves. This decreases the amount of energy transferred through resonant interaction from the electron beam to the Langmuir waves. With less total energy, a smaller amount of energy in Langmuir wave form can drift to higher or lower phase velocities and not be re-absorbed by the electron beam. The amount of deceleration the electron beam can undergo due to
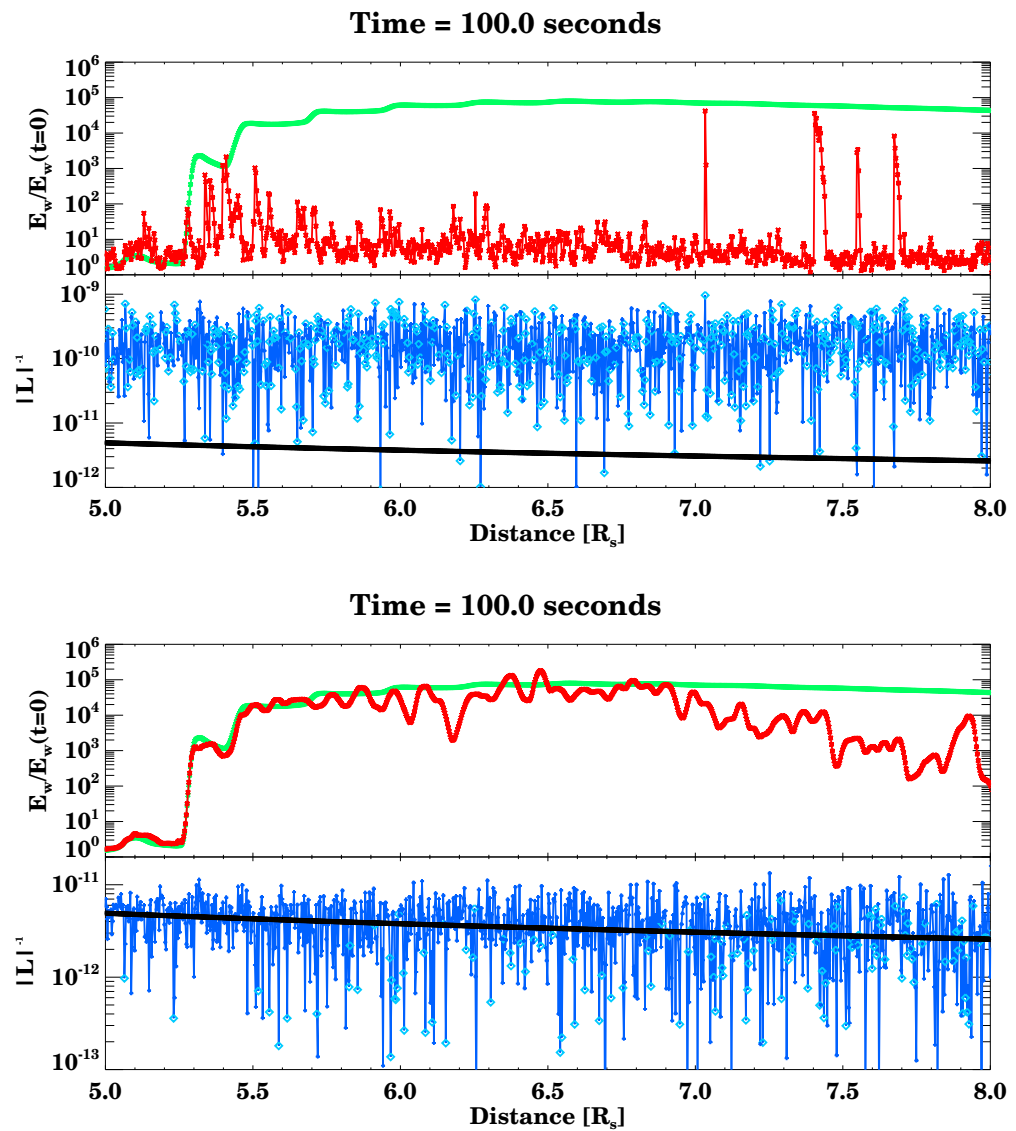
Figure 3.9: The Langmuir wave energy and corresponding plasma inhomogeneity when density fluctuations have a power law spectra in frequency space and $\Delta n_e/n_e = 10\%$ at the Earth Top: The fluctuations are constant from the Sun to the Earth ($\psi = 0$). Bottom: The fluctuations increase from the Sun to the Earth ($\psi = 0.5$). Both graphs are over plotted with the unperturbed case (green). The plasma inhomogeneity is plotted for unperturbed case (black) and perturbed case (blue) with light blue diamonds for positive values.
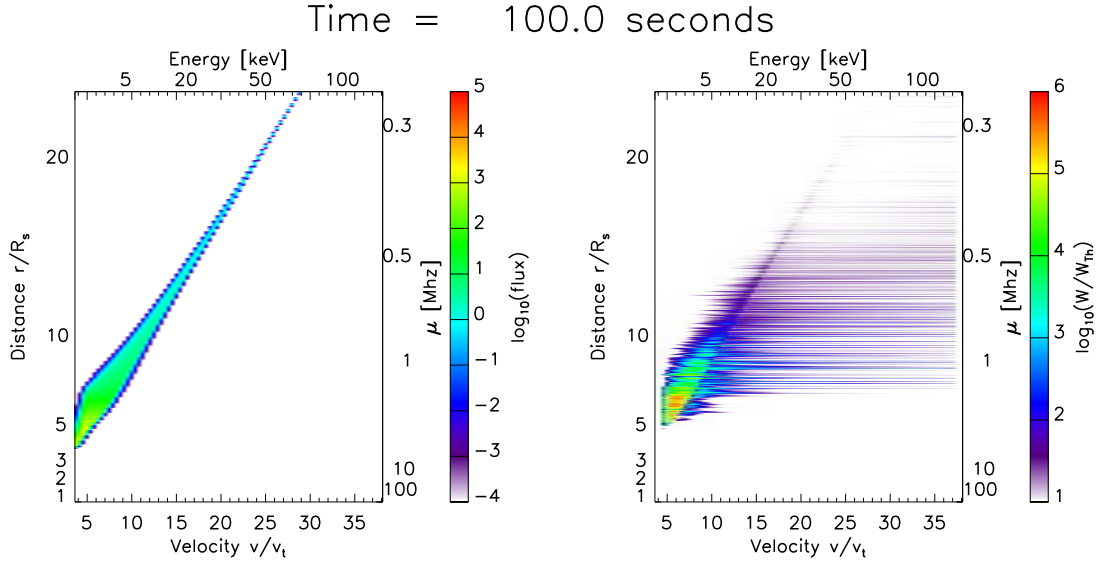
Figure 3.10: Colour coded plot of the electron flux $[\text{cm}^2 \text{ eV s}]^{-1}$ and spectral energy density (normalised by thermal level $W(v, r, t = 0)$) of Langmuir waves. Distance and velocity are normalised by solar radii and thermal velocity respectively. The small-scale fluctuations have a power law spectra in frequency space where the fluctuations increase from the Sun to the Earth with $\psi = 0.5$.

Langmuir waves drifting is decreased, causing a reduction in the flattening of the fluence electron spectrum. This means when Υ is larger, the fluence spectrum below the break energy has a higher spectral index (Figure 3.12). Similar behaviour is demonstrated by the fluence spectrum of the electron beam at the Earth for four different wavelengths of small-scale fluctuations within the range 10^8 cm $\leq \lambda \leq 10^{11}$ cm, shown in Figure 3.11. The same lack of wave generation for small λ reduces the deceleration the electron beam undergoes and hence reduces the flattening of the fluence spectrum (Figure 3.12).

The recent survey of in-situ measured impulsive solar energetic electron events (Krucker et al. 2009) suggests the break energies generally appear in the deca-keV range. Results from the numerical simulations in Chapter 2 are in line with this result. The improved numerical model presented in this chapter also displayed results
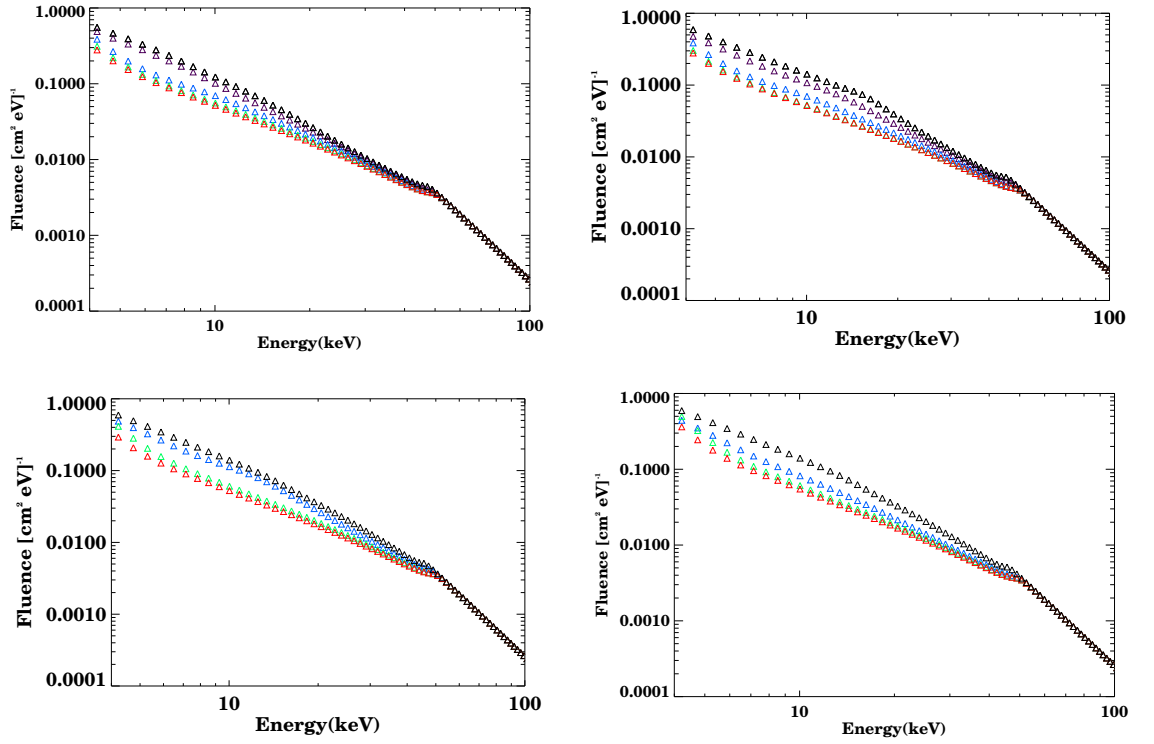
Figure 3.11: Fluence of the electron distribution function near the Earth. Top Left: Five simulations with $\Upsilon = 10^{-1}$ (black), $10^{-1.5}$ (purple), 10^{-2} (blue), $10^{-2.5}$ (green), and 10^{-3} (red). $\lambda = 10^{10}$ cm. Top Right: Five simulations with $\lambda = 10^{8}$ cm (black), 10^{9} cm (purple), 10^{10} cm (blue), 10^{11} cm (green) and unperturbed (red). $\Upsilon = 10^{-2}$. Bottom Left: Four simulations for multi-scale fluctuations with $\Delta n_e/n_e$ of 10 % (black), 1 % (blue), 0.1 % (green) and 0.01 % (red) of the mean background density. Bottom Right: Four simulations for multi-scale fluctuations which decrease in power close to the Sun for ψ of 0 (black), 0.3 (blue), 0.5 (green), 0.8 (red).

consistent with the Krucker et al. (2009) observation. Moreover, the break energy seems to be insensitive to the level of density fluctuations in the background plasma.

Despite the change in spectrum near the Earth, the electron distribution function does not share the same sensitivity to the structure of the background electron density as the Langmuir waves (See Figures 3.4 and 3.5). The simulation with perturbed plasma does however show small changes, most noticeably in the tail of the electron

distribution. A positive spatial gradient in background plasma causes Langmuir waves to drift to higher phase velocities. Drifting of waves in velocity space allows their energy to be re-absorbed by lower energy electrons at the tail of the beam such that electrons are accelerated to higher energies. It is the opposite effect of the negative density gradient taking Langmuir wave energy away from electrons and forming a broken power-law near the Earth. This acceleration of electrons causes the noticeable bump around $10 - 20$ keV in Figure 3.11, seen for simulations with higher spectral indices below the break energy. The bump becomes more prominent for small λ, high Υ or more generally when the background density fluctuations are more effective at moving wave energy to higher phase velocities.

Extending the density fluctuations to multi-wavelength model, a Kolmogorov type power-law is assumed where $(\Delta n_e/n_e)^2 \sim \lambda^{5/3}$ with $\Delta n_e/n_e$ remaining radially constant ($\psi = 0$). Figure 3.11 shows the fluence spectrum at the Earth for four different turbulent intensities $0.01\% \leq \Delta n_e/n_e \leq 10\%$. The larger $\Delta n_e/n_e$ is, the higher the spectral index below the break energy of the fluence spectra (Figure 3.12). The signature bump can be seen in the spectra around $10 - 20$ keV, again caused by the acceleration of electrons at the back of the beam due to Langmuir waves drifting to higher phase velocities.

The electron beam fluence spectra for density fluctuations $\Delta n_e/n_e$ changing with distance (reaching 10% at 1 AU) are displayed in Figure 3.11 for four different values of ψ within the range $0 \leq \psi \leq 0.8$. The decreased presence of fluctuations near the Sun ($\psi > 0$) increases the amount of induced Langmuir waves which decreases the spectral index below the break energy, shown in Figure 3.12. For all simulated values of $\psi > 0$ no bump in the fluence spectra is present. A reduced level of fluctuations near the Sun decreases positive density gradients which subsequently decreases the acceleration of electrons from re-absorption of Langmuir waves. A smoother increase in spectral index below the break energy for increasing ψ can thus be seen in Figure 3.12
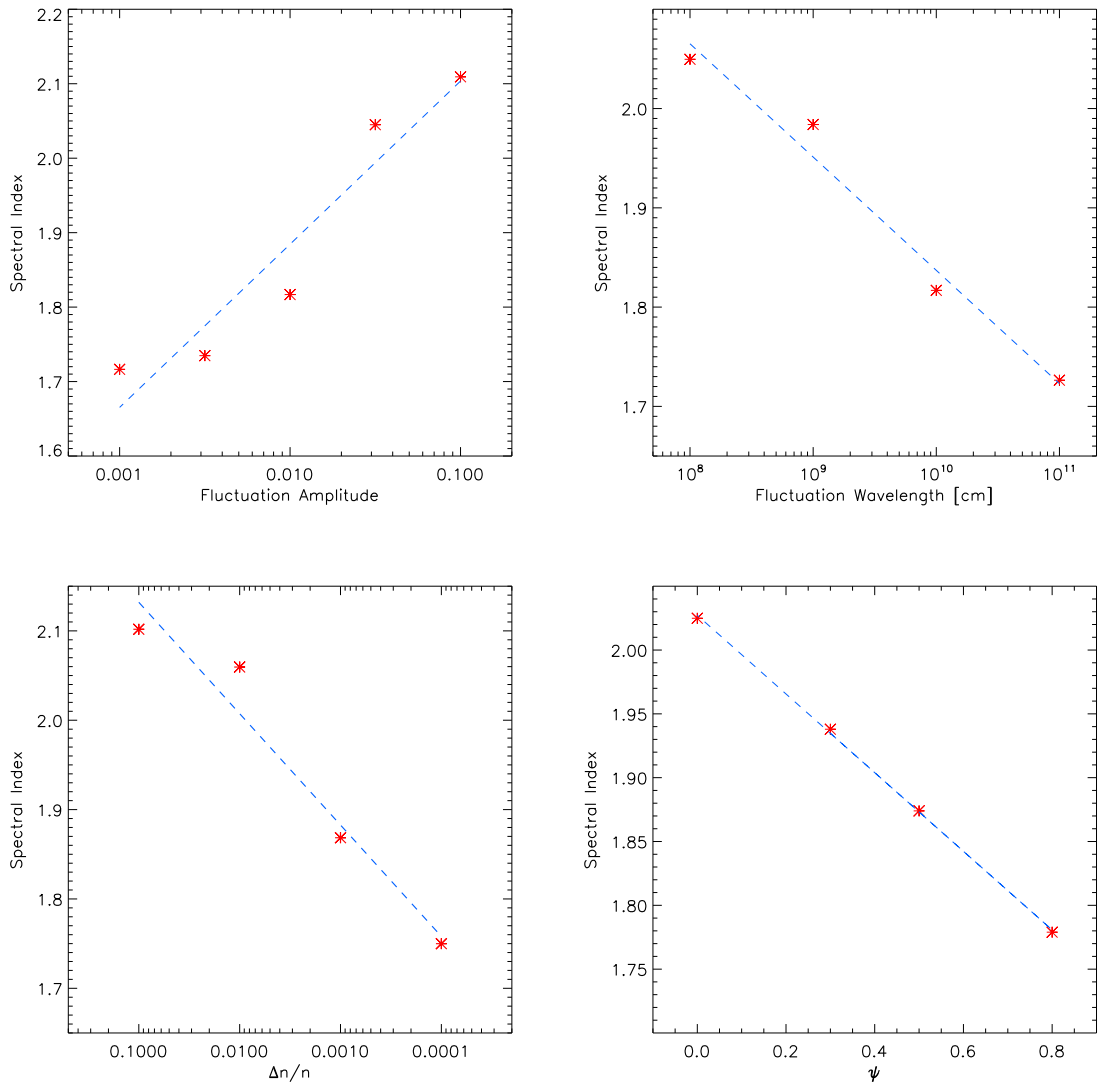
Figure 3.12: The spectral index of a power law fit between 4 and 40 keV for the fluence spectra of electrons near the Earth. Top Left: Spectral index versus the amplitude of density fluctuation. Top Right: Spectral index versus the wavelengths of density fluctuation. Bottom Left: Spectral index versus multi-scale level of fluctuations. Bottom Right: Spectral index versus ψ, the radial degree at which density fluctuations become less dominant.

3.5   Discussion and Conclusions

The simulations show that fine structure in the background solar wind electron density causes the generation of Langmuir waves from a non-thermal electron beam to be suppressed, with larger amplitudes and smaller length scales of density fluctuations having the largest effect. Increased suppression for larger amplitudes is similarly observed for higher levels of turbulence ($\Delta n_e/n_e$) with Kolmogorov type density fluctuations.

For high levels of turbulence near the Sun, $\Delta n_e/n_e = 10\%$, wave production by the electron beam becomes no longer sufficient for the generation of type III radio bursts. It is possible to induce more Langmuir waves by increasing the density of the electron beam. This solution requires at least two orders of magnitude more electrons than previously simulated, causing the beam to have around 1% of the density of the background plasma. Such high density electron beams become problematic when considering simultaneous HXR bursts assuming the upward electron beam has only 0.2% of the downward electron beam density, found above 50 keV in Krucker et al. (2007).

Increasing the level of Langmuir waves near the Sun without increasing beam density, the amplitude of density fluctuations can be reduced. We implemented a radial dependence with closer distances to the Sun having a decreased turbulent intensity. This is seen in observational scintillation techniques (Woo et al. 1995; Woo 1996) and *Helios* data (Marsch & Tu 1990) in the fast solar wind. The observed values for $\Delta n_e/n_e$ are as low as 0.3% at distances < 0.1 AU (Woo et al. 1995). A much higher magnitude of Langmuir wave energy density was achieved close to the Sun with smaller levels of fluctuations. Type III emission in the low corona thus requires low turbulence intensity or beam densities much higher than observational evidence predicts.

To estimate how density fluctuations might radially evolve, we varied the initial conditions of the simulations. We used a variety of different initial electron beam spectral indices (δ in Equation 3.3) and different radial dependence of density fluctuations (ψ in Equation 3.9). Using the resulting fluence spectra near the Earth for each simulation, we compared the spectral indices above and below the break energy (Figure 3.13).

The spectral index becomes smaller below the break energy for larger values of ψ. We have also overplotted the correlation of spectral indices above and below the break energy of peak flux measurements taken from a statistical survey (Krucker et al. 2009) of impulsive electron events detected by the three-dimensional Plasma and Energetic Particles experiment on the WIND spacecraft (Lin et al. 1995). A level of fluctuations with ψ around 0.25 would give a similar correlation to the observational line. We note, however, that the observational line presented from Krucker et al. (2009) fitted a large scatter of data points. The ratio of low:high spectral index for all simulated results presented in figure 3.13 lies between 0.42 and 0.58, which is within the narrow range presented in Krucker et al. (2009).

A variety of simulation variables can affect the energy of the spectral break at the Earth: the model of radial background density decrease, the density fluctuations, the initial spectral index of the beam, the number density of injected electrons, the spatial distribution of injected electrons, the temporal nature of the injection, and the initial coronal background density where the electrons are injected. The spectral index below the break energy of the resultant double power-law in fluence spectra near the Earth is increased when density fluctuations have a larger effect on the level of induced Langmuir waves. It is important to note, however, the spectra below the break energy is only approximately a power-law. The presence of density fluctuations causes fine structure to be present. A bump around 10-20 keV was found, caused by acceleration of electrons at the back of the beam through absorbed Langmuir waves. The onset of this bump appears to be close to the Sun where Langmuir wave energy density is high. The magnitude of this bump is reflected in the size of the spectral index error bars in Figure 3.13 with a larger bump corresponding to a larger error. With the prospect of Solar Orbiter and Solar Probe Plus, it will be very attractive to extend these studies further to understand the spectral evolution of the electron beam between the Sun and the Earth.
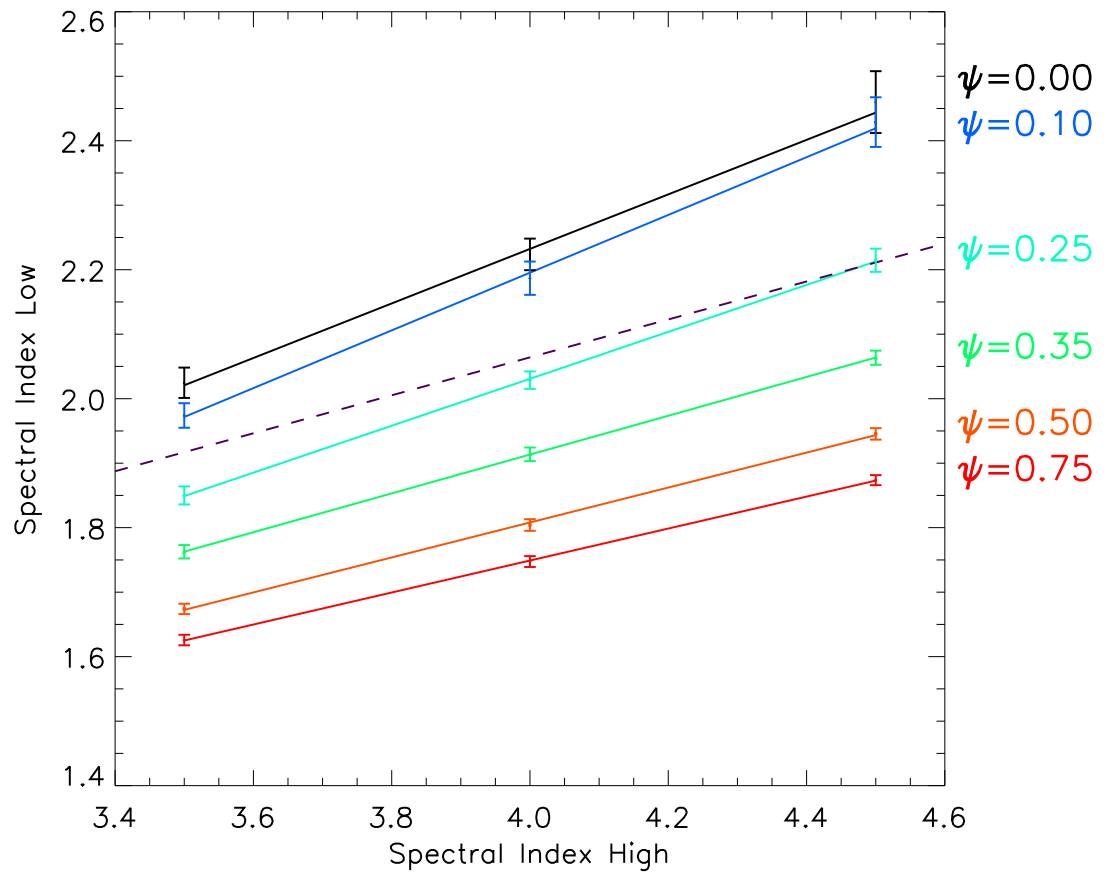
Figure 3.13: Comparison between the high and low spectral index of fluence spectra of electrons near the Earth. The dashed purple line is the best fit to the observational data of peak flux spectral indices (Krucker et al. 2009).

Chapter 4

Electron acceleration region diagnostics

4.1 Introduction

Accelerated electron beams are believed to be responsible for both hard X-ray (HXR) and coherent radio emission during solar flares. Despite this wealth of electromagnetic beam emission from accelerated electrons propagating in plasma, the location of the electron acceleration site and its spatial characteristics are poorly known.

This chapter shows how simultaneous radio and X-ray observations can be used to diagnose not only the location but the size of the acceleration region. It provides the first observational estimate of both the location and size of the acceleration region. Numerical simulations are used with these inputs to help validate the results and explore unknown electron beam parameters.

4.1.1 HXR emission

The 'standard model' in solar flares of HXR emission involves electron beams travelling downwards from the corona to the chromosphere with small pitch angles directed by the magnetic field. These electron beams emit HXR at two footpoints in the chromosphere near the photospheric footpoints of the flare magnetic topology (Figure 4.1). The
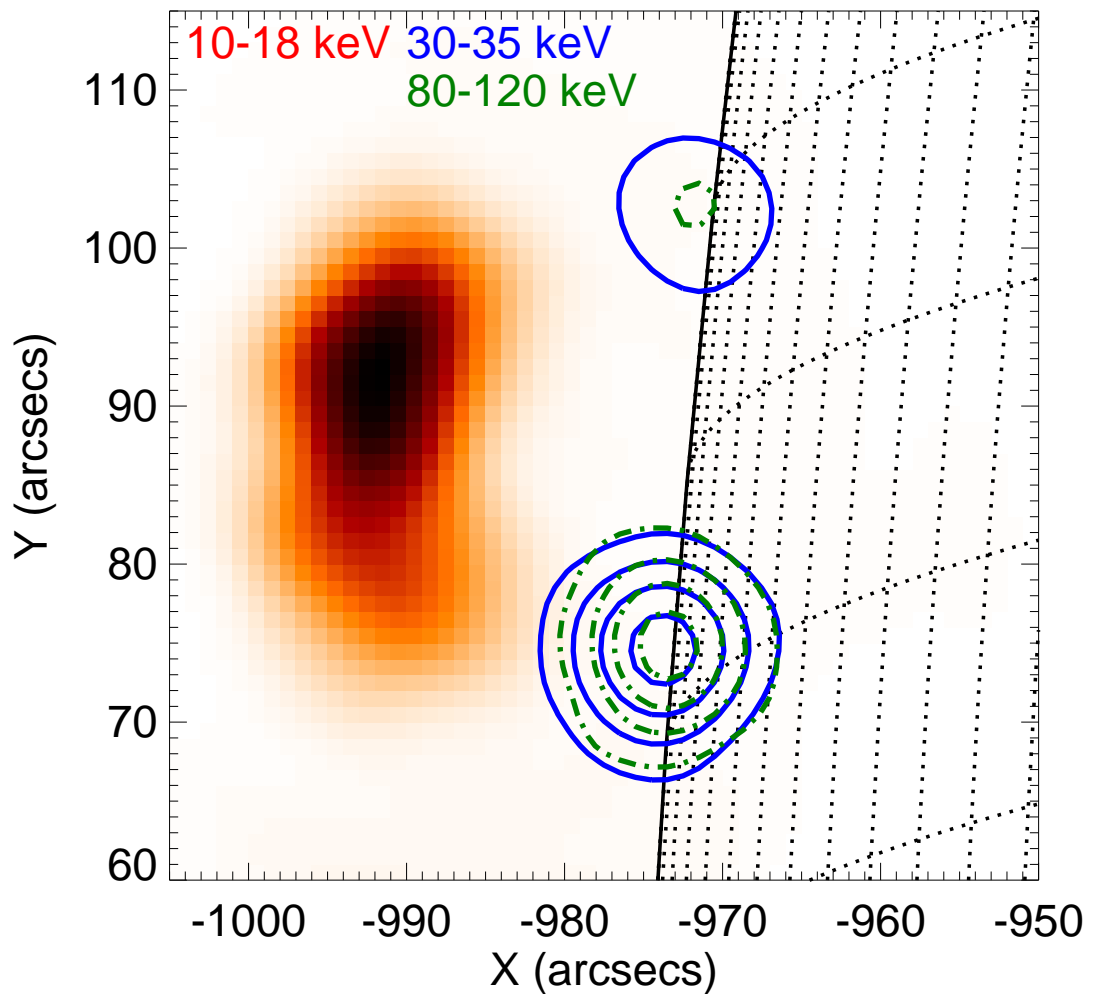
Figure 4.1: RHESSI X-ray images of the January 6, 2004 limb event. The contours show HXR emission integrated for the impulsive phase of the flare (06:22:20-06:23:00 UT) from the footpoints in 30-35 keV (solid blue line) and 80-120 keV (dot-dashed green lines). The background image shows subsequent softer thermal emission (06:24:00-06:24:40UT) in 10-18 keV.

electron beam loses most of its energy through heating the surrounding chromospheric plasma to tens of MK. The hot plasma generates a pressure gradient which forces the

heated plasma up into the corona where it fills the coronal part of the flare loops. The plasma then cools, emitting at soft X-ray (SXR) and EUV wavelengths. An interesting feature of the SXR emission in the majority of flares is that it can be approximated as the integral of the HXR flux over time, known as the Neupert effect (Neupert 1968).

The solar flare HXR spectrum $I(\epsilon)$ generally takes the form of a thermal distribution $I(\epsilon) \sim \exp(-\epsilon/k_B T_e)$ at photon energies $\epsilon \lesssim 20$ keV where T_e is the electron temperature with typical values around 2 MK. At larger photon energies $\epsilon \gtrsim 20 keV$ the HXR spectrum takes the form of a power-law $I(\epsilon) \sim \epsilon^{-\gamma}$ where γ is the spectral index of the power-law. These two distributions are categorised as the 'thermal' and 'non-thermal' component of HXR emission. An example of a flare induced HXR spectrum is given in Figure 4.2. The spectral index of the non-thermal component of the emission varies in time during a flare. It usually starts off large (soft), around 6 or 7, indicating a small ratio of high:low energy photons. As the impulsive phase of the flare progresses the spectral index gets smaller (harder), around 2-4, indicating an increase in the ratio of high:low energy photons. The onset of a harder spectrum is correlated with an increase in overall photon intensity. A softening of the spectrum occurs in the later part of the HXR burst coupled with a decrease in overall photon intensity. This trend is called soft-hard-soft (SHS) and is the generally observed HXR spectral trend in flares (e.g. Parks & Winckler 1969; Benz 1977; Fletcher & Hudson 2002; Grigis & Benz 2008). Possible reasons for the observed SHS spectra of HXR emission could be trapping of electrons in the acceleration region or a time variation in the efficiency of electron acceleration.

The non-thermal component of HXR emission is believed to be emitted by an electron beam streaming down from a coronal acceleration site. It is possible with certain assumptions to ascertain information regarding the electron beam from the HXR emission. Specifically using the thick target approximation (Brown 1971) it is possible to approximate, amongst other parameters, the spectral index of the inducing electron beam. The thick target approximation assumes an electron beam that is 'thermalized' as it streams into a high density plasma with HXR emission being produced via non-thermal bremsstrahlung (breaking radiation) emission. In a solar flare the primary
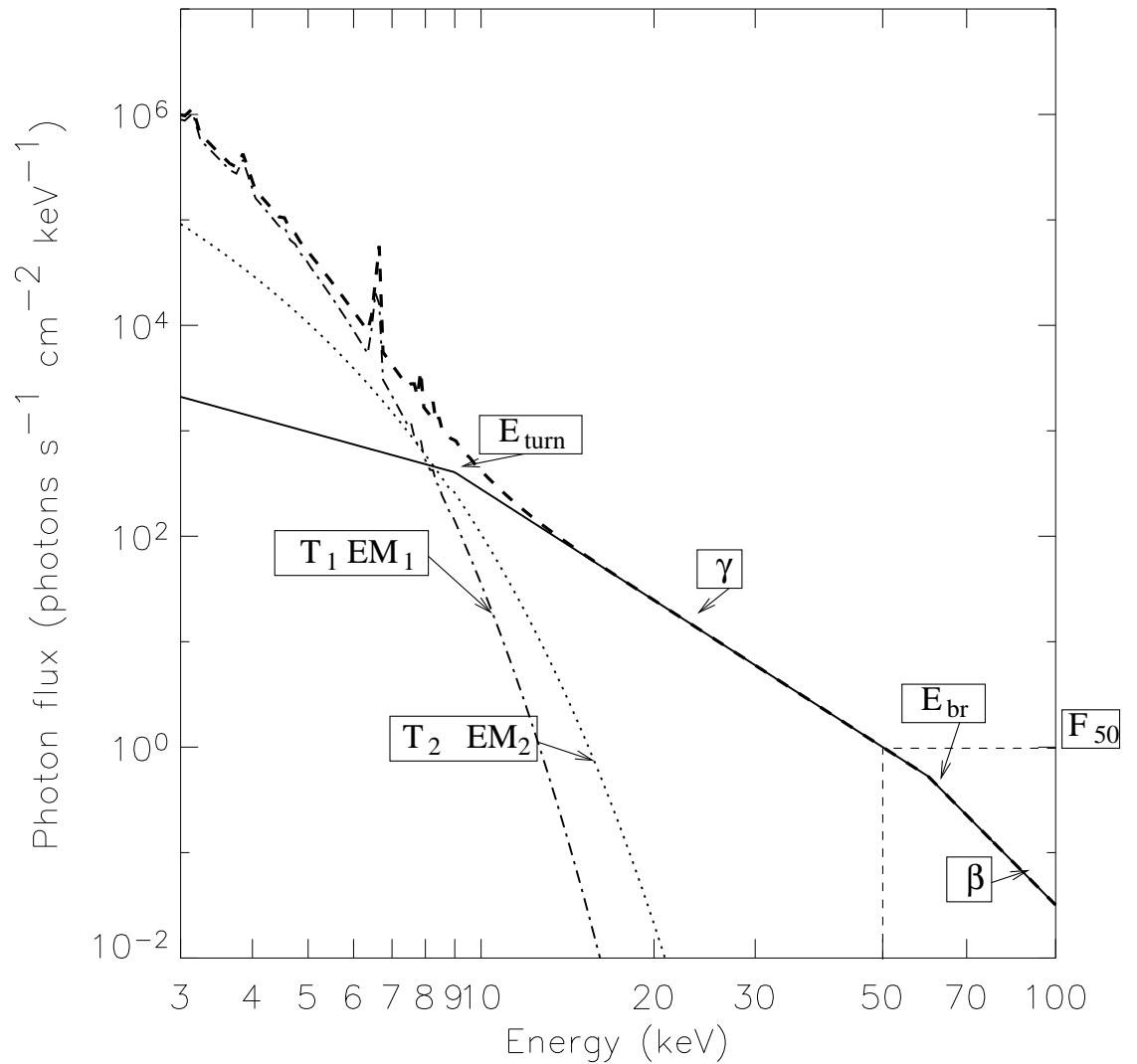
Figure 4.2: Example of a flare induced HXR spectrum. A non-thermal component (solid line) and two thermal components (dotted and dash-dotted) are shown. Boxed symbols show the many different free parameters which have to be chosen when forward-fitting the data (Battaglia et al. 2005)

source of HXRs are electrons undergoing free-free bremsstrahlung emission by collisions with particles. A detailed mathematical description of thick-target bremsstrahlung emission is beyond the scope of this thesis. Interested readers are directed towards

Tandberg-Hanssen & Emslie (1988) for a complete description. The key property of the collisions is that the electrons are deflected and hence emit photons with equal or less kinetic energy than their initial energy. For a given injected electron beam flux spectrum $F(E_0)$ the thick target approximation requires a mean (or target averaged) electron distribution $\bar{F}(E)$ which reflects the alteration of the injected distribution due to electron energy losses. For a given mean electron flux spectrum $\bar{F}(E)$, the observed HXR spectrum is given in the relation (e.g. Kontar et al. 2004).

$$I(\epsilon) = \frac{1}{4\pi R^2}\bar{n}_e V \int_\epsilon^\infty \bar{F}(E)Q(\epsilon, E)dE, \tag{4.1}$$

where R is the distance from the source to the observer, $\bar{n}_e$ is the mean density of the target, V is the emitting volume, and $Q(\epsilon, E)$ is the bremsstrahlung cross-section. Under the thick target approximation, the electron beam flux loses its energy only through Coulomb collisions. The collisional loss of electrons in a plasma is preferential for low energy electrons (see 3.2 for a description), changing the spectral index of $\bar{F}(E)$. The spectrum of photons, γ, thus becomes harder than the injected spectrum of electrons, δ, by the simple relation $\gamma = \delta - 1$. It is interesting to note the thin target approximation (Brown 1971) uses an opposite assumption that electron beam spectrum is not changed as the beam streams through a plasma. The resulting HXR spectrum in a thin target is $\gamma = \delta + 1$. An E^{-2} dependence of the Coulomb collisional cross-section causes a spectrum of photons two powers harder in a thick target over a thin target.

The detection of HXR spectra like Figure 4.2 shows an approximate power-law behaviour of HXRs above 20 keV. Similar to the power-law of interplanetary electrons at Earth shown in Chapter 3, power-law behaviour of the non-thermal component is an approximation. The usual method for finding electron beam spectra is known as forward fitting (Holman et al. 2003), where a power-law is approximated via a least squares fit to the HXR spectrum. The deduced spectral index given to the non-thermal distribution depends upon the other parameters required for forward fitting the HXR spectrum (most being listed in Figure 4.2) and they all affect . To avoid such ambiguities, advanced inversion techniques can be employed which infer the effective mean electron

source spectrum directly from the HXR spectra (Piana et al. 2003; Kontar et al. 2004; Brown et al. 2006). Inversion techniques are model independent and involve inverting Equation 4.1 to find $\bar{F}(E)$. Unfortunately inversion is particularly challenging as the noise present in even the most accurate photon spectra can become hugely amplified when trying to extract the electron flux spectrum. Regularization methods which apply physical constraints to the electron spectra (e.g. Craig & Brown 1986) can be used to avoid noise amplification and obtain a good estimate for $\bar{F}(E)$. Such techniques can lead to finding electron beam spectral indices which vary in both time and energy (e.g. Kontar & MacKinnon 2005).

4.1.2 HXR-Radio observations

Accelerated electron beams are believed to be responsible for both HXR and coherent radio emission during solar flares. Upward travelling electron beams propagate through the coronal plasma and sometimes escape into interplanetary space. Emission from such beams is often observed as coronal and interplanetary type III radio bursts. Electron beams travelling downwards with small pitch angles enter the dense plasma of the chromosphere and are generally seen through bremsstrahlung emission in HXR. Before entering the chromosphere, downward propagating electron beams may also produce reverse type III bursts. Despite this wealth of electromagnetic beam emission from accelerated electrons propagating in plasma, the location of the electron acceleration site and its spatial characteristics are poorly known.

Indirect evidence of electron acceleration sites first came from broad band radio spectral observations of pairs of type III and reverse type III bursts (e.g. Aschwanden et al. 1995a; Aschwanden & Benz 1997). The starting frequencies of these burst pairs are found between $220 - 910$ MHz, implying a range of electron densities in the acceleration region between $6 \times 10^8 - 10^{10}$ cm^{-3} for fundamental emission or $1.5 \times 10^8 - 3 \times 10^9$ cm^{-3} for harmonic emission. These densities are lower than ones observed in bright soft X-ray loops ($2 \times 10^{10} - 2 \times 10^{11}$ cm^{-3}) suggesting that the acceleration region lies above the soft X-ray loops, being located for example in a cusp reconnection site. HXR ob-

servations have also been independently used to provide insight into typical electron acceleration region heights above the photosphere. Through electron time-of-flight analysis using HXR emission in the range 20-200 keV (Aschwanden et al. 1998), height estimates have been found in the range 20-50 Mm. The spatial size of the acceleration region still remains largely unknown.

The simultaneous observation of HXR and metric/decimetric radio emission is commonplace during flares and the relationship between type III bursts and hard X-ray emissions has been studied for many years (see for example Pick & Vilmer 2008, for a review). The first studies performed by Kane (1972) found a good similarity between HXR and type III radio emission, suggesting the two emissions are produced by electrons originating from a common acceleration site. Many subsequent studies have specifically dealt with the association of coherent type III radio emission and HXR bursts, both statistically (e.g. Kane 1972, 1981; Hamilton et al. 1990; Aschwanden et al. 1995a; Arzner & Benz 2005) and for individual events (e.g. Kane et al. 1982; Benz et al. 1983; Dennis et al. 1984; Raoult et al. 1985; Aschwanden et al. 1995b; Raulin et al. 2000; Vilmer et al. 2002). A more recent statistical study of 201 flares above GOES class C5 (Benz et al. 2005) reports an 83% association rate with coherent radio emission, within the range between 4 GHz and 100 MHz. These results suggest that practically all flares with HXR GOES class $>$ C5 [1] are associated with some form of coherent radio emission.

An in depth statistical study was carried out between radio type III bursts and HXRs by (Kane 1981). The study reported that the X-ray/type III correlation increases systematically with the intensity of HXR and radio emission, the peak spectral hardness of HXR emission and the type III burst starting frequency. Hamilton et al. (1990) similarly reported the systematic increase of HXR/type III correlation with increasing emission intensity and to a lesser extent with spectral index of HXR emission. Hamilton et al. (1990) also reported a statistical correlation between the peak HXR and type III intensities. To produce a harder (smaller spectral index) HXR photon

---

[1] A flare categorisation model which classes flares based upon their peak SXR flux

spectrum requires a harder electron beam spectrum. A hard electron beam spectrum is an attractive attribute for type III producing electron beams as it makes it easier and faster for the bump-in-tail instability to occur. Faster instability onset ties in very well with the HXR/type III correlation increasing for bursts with a higher starting frequency.

A temporal correlation between HXR and radio pulses has been found statistically (Aschwanden et al. 1995a) where the average time delay between the HXR pulse and radio pulse starting frequency was ≤ 0.1 s. Temporal correlations have also been found in many individual event studies. Of these studies the results by Dennis et al. (1984) find a temporal correlation with a similar magnitude to the statistical study by Aschwanden et al. (1995a). This, together with previous correlations, suggests a common acceleration region with HXR producing electron beams having either slightly less distance to travel or slightly more energetic electrons responsible for the emission. The simultaneous analysis of HXR and type III radio bursts is thus an attractive diagnostic of flare associated electron acceleration.

A few previous studies have attempted to infer properties (both height and size) of the common electron acceleration region from simultaneous HXR and radio observations. Kane et al. (1982) used an inferred spectral index from HXR emission to estimate the minimum distance required for the type III producing electron beam to become unstable. With an assumed electron acceleration height of 20 Mm, an altitude of 100 Mm was deduced for the starting frequency, in good agreement with the spectral observations. Unfortunately the type III frequencies in this analysis were too high with respect to the Nançay radioheliograph frequencies for radio imaging at this time so it was not possible to confirm the starting height of the radio emission. Benz et al. (1983) also considered the minimum distance required for a type III producing electron beam to become unstable. By modelling both the HXR and radio producing electron beam as a Maxwellian they found a weak correlation between the type III starting frequency and the electron temperature derived from HXR observations above 26 keV. However, in the event considered a change in electron temperature cannot fully account for the initial change in type III starting frequency. The authors thus conclude that a

movement of the acceleration site occurred for this event.

In another study Aschwanden et al. (1995a) uses the assumption of a common acceleration region producing upward and downward electron beams to estimate acceleration times and infer acceleration region sizes. No frequency gap was observed between type III and reverse type III emission so their starting frequency separation distance was constrained by the detector resolution. Using an assumed density model, this distance was found to be < 2 Mm. The instability distance for the electron beam was then equated to twice this resolution. By using a similar analysis of Kane et al. (1982) with observed HXR spectral index, acceleration times are found with $\Delta t < 0.3 - 3$ ms. The size of the acceleration region is then inferred at 0.7 Mm. This constraint of acceleration site size and times is heavily dependent upon the assumption of bidirectional electron beams starting with a separation unresolved by the detector and thus should be treated with care.

Electron beams escaping into the inner heliosphere can also be detected in-situ near 1 AU and their numbers have been correlated to the number of HXR producing electrons (Krucker et al. 2007). A correlation is found between the spectral indices of both electron populations as well as between the numbers of HXR producing electrons and escaping electrons for prompt electron events. This again suggests that the X-ray producing electrons and the electrons moving upward in the corona originate from a common acceleration site. Furthermore, it is found that the number of escaping electrons is on average only 0.2% of the HXR-producing electrons above 50 keV.

4.2 Starting frequency of type III bursts

The aim of the following theory is to relate known observational variables from flares to unknown flare parameters. Specifically we will relate the starting frequency of type III bursts and the spectral index of the inducing electron beam to the height and size of a flare acceleration region. Initially let us consider the propagation of a flare accelerated

electron cloud with starting size d located at $r = 0$

$$f(v, r, t = 0) = g_0(v)exp(-|r|/d) \tag{4.2}$$

where $g_0(v)$ is the initial electron velocity distribution. Langmuir waves will be generated when their growth rate is larger than the collisional absorption by the background Maxwellian plasma

$$\gamma(v, r) = \frac{\pi \omega_{pe}}{n_e} v^2 \frac{\partial f}{\partial v} > \gamma_c, \qquad \gamma_c = \frac{\pi e^4 n_e}{m_e^2 v_{Te}^3} \ln \Lambda \tag{4.3}$$

where $\ln \Lambda$ is the Coulomb logarithm, taken near 20 for the parameters in the corona. ω_{pe}, n_e and v_{Te} are the background plasma frequency, density and thermal velocity respectively.

The initial velocity distribution of solar flare accelerated particles is normally a power-law $g_0(v) \sim v^{-\alpha}$. This distribution at $t = 0$ is stable and will not lead to generation of Langmuir waves. At later times $t > 0$ the propagation of particles leads to the formation of a positive slope in velocity space ($\partial f / \partial v > 0$). The distribution function changes in time due to the propagation (in the case of no energy losses)

$$f(v, r, t) = g_0(v)exp(-|r - vt|/d) \tag{4.4}$$

and the growth rate for Langmuir waves becomes

$$\gamma(v, r) = \frac{\pi \omega_{pe}}{n_e} v^2 f(v, r, t) \left(\frac{t}{d} - \frac{\alpha}{v} \right). \tag{4.5}$$

We can observe large Langmuir wave growth remotely via observations of type III radio emission. Langmuir wave growth should occur at the distance $\Delta r = h_{typeIII} - h_{acc}$ from the original location where $h_{typeIII}$ is a height corresponding to the starting frequency of type III bursts and h_{acc} is the acceleration region height. The distance Δr can be found by equating the growth rate for Langmuir waves given in Equation (4.5) with γ_c giving

$$\Delta r = d \left(\alpha + \frac{\gamma_c n_e}{\pi \omega_{pe}} (v g_0(v))^{-1} \right). \tag{4.6}$$

The quantity $v g_0(v) \approx n_b$ where n_b is the inducing electron beam density. By assuming a coronal background electron density of 10^9 cm^{-3}, a coronal electron temperature of

2 MK and a beam density of 10^4 cm^{-3} the second term $\gamma_c n_e/\pi \omega_{pe} n_b$ is around 10^{-3}. Thus the relation between the acceleration site properties and starting frequency is determined mostly by the spectral slope, giving the simple relation

$$h_{typeIII} = d\alpha + h_{acc} \tag{4.7}$$

The unknown parameters h_{acc} and d can be found from the known parameters α and $h_{typeIII}$. A key advantage of this relation lies with its lack of dependence on the poorly known electron beam number density necessary to produce type III emission. The method is similar to what was discussed in Kane et al. (1982). The key difference is that we consider an instantaneous injection at $t = 0$ with a spatially broad distribution function while Kane et al. (1982) considers a temporal injection from a point source.

4.3 Observations and data analysis

4.3.1 Observation instruments

The Ramaty High Energy Solar Spectroscopic Imager (RHESSI) (Lin et al. 2002) is designed to investigate energy release from accelerated particles in solar flares. It was the first spacecraft with high-resolution HXR imaging spectroscopy at a spatial resolution ≈ 2.3 arcsec and a full-Sun field of view. It boasts a spectral resolution $\approx 1 - 10$ keV FWHM over the energy range from 3 keV to 17 MeV. RHESSI was launched in February 2002 into a nearly circular 600 km altitude orbit around the Earth. The RHESSI spacecraft is used in this chapter to observe HXR emission emitted in the chromosphere from downward propagating electron beams. By assuming a common acceleration site for upward and downward electron beams, the HXR emission observed by RHESSI can serve to provide the spectral index for the above relation (Equation 4.7). RHESSI can also provide spatial information regarding the HXR emission.

The broadband radio spectrometer Phoenix-2 (Messmer et al. 1999) is designed to register the flare emission of the full Sun. Phoenix-2 is a redesign of the original Phoenix radio spectrometer (Benz et al. 1991), based at Bleien, Switzerland. The new

design has complete autonomous operation, a larger frequency range and more accurate results. In the frequency range of operation, 0.1 to 4.0 GHz, both modes of circular polarization are recorded continuously. The free choice of the number, bandwidth and frequency of the observed channels makes Phoenix-2 very flexible for both broadband surveys as well as specific studies at high temporal or spectral resolution. For observing the radio emission in the corona, the spectral information in this chapter was obtained by using Phoenix-2 data within the frequency range 160 - 700 MHz. This provides information regarding the starting frequency of the type III radio emission.

The Nançay Radioheliograph (NRH) (Kerdraon & Delouis 1997) was designed for fast imaging of solar radio emission. Observing frequencies may be chosen in the limits 150 - 450 MHz with simultaneous observations of up to 10 frequencies. The speed allows a maximum number of 200 images per second. The NRHs most recent design provides high time resolution 2D images of the solar corona using a digital correlator (Stokes I and V, 576 channels). The spatial information for type III radio emission is found by using the NRH in the frequency range of 164 - 432 MHz. The spatial radio information observed by the NRH allows one to be certain that the observed strong radio flux is emitted from the same location in the solar atmosphere to the HXR emission.

4.3.2   Event selection

We aimed our study at cases observed simultaneously with the NRH, Phoenix-2 and RHESSI. We started our selection from a list of events presented in previous observational analysis between coherent radio and HXR emissions (Arzner & Benz 2005; Grigis & Benz 2004; Benz et al. 2005). Of the 58 events considered, 10 were found to have coherent radio emission in the frequencies covered by the NRH observations. We selected one event which had a simple spatial configuration at all NRH radio wavelengths, clearly defined starting frequencies and a strong HXR flux. This event was chosen as an illustration of the method.

4.3.3   Observations in HXR and radio

The spatial overview of the April 15th flare is presented in Figure 4.3 using RHESSI, NRH and SOHO/EIT. The X-ray source was imaged using RHESSI in the energy range between 15 and 30 keV. The higher energies had too few photons to make a reasonable image above the background noise. The radio source was imaged using the NRH in frequency bands from 164 to 432 MHz and the size increases with decreasing frequency. This can provide an estimate regarding the radial magnetic field expansion locally in the corona. However, the decrease of spatial resolution with decreasing frequency using the NRH has to be considered. This decrease behaves as D/λ where D is the maximum antenna spatial separation and λ is the wavelength of the radio emission. The SOHO/EIT 195 image displays information about the overlying plasma configuration, conferring insight into the magnetic field structure where the flare originates. The temporal evolution of the flare is presented in Figure 4.4, using Phoenix-2, NRH and RHESSI data.

The spectral index of the X-ray emission, γ, was obtained using RHESSI spectral analysis of the photon flux $I(\epsilon) \sim \epsilon^{-\gamma}$. The photon spectral index γ was estimated using a power-law fit every 2 seconds (half-rotation of the spacecraft). The one sigma error associated with the power-law fit was used as the spectral index error estimates.

The starting frequency of the type III radio emission was determined from the Phoenix-2 data. We used Phoenix-2 data with a 1 sec temporal resolution. The mean value of the radio flux on the quiet 3 minute interval 08:56 UT to 08:59 UT was used to quantify the background level for each frequency channel. A threshold of twice this background level was then used at every moment in time to determine the starting frequency of the radio emission. We then averaged the starting frequency over the 2 second RHESSI interval. The mean width of the radio channels between 100 and 700 MHz was 9.2 MHz so we took 10 MHz as the one sigma error on the starting frequency.

The combined determination of starting frequencies and spectral indices was done on two time periods between 08:51:20 → 08:51:36 UT and 08:52:38 → 08:53:00 UT. Both periods have a HXR non-thermal spectral index below 7.5 at all points in time.
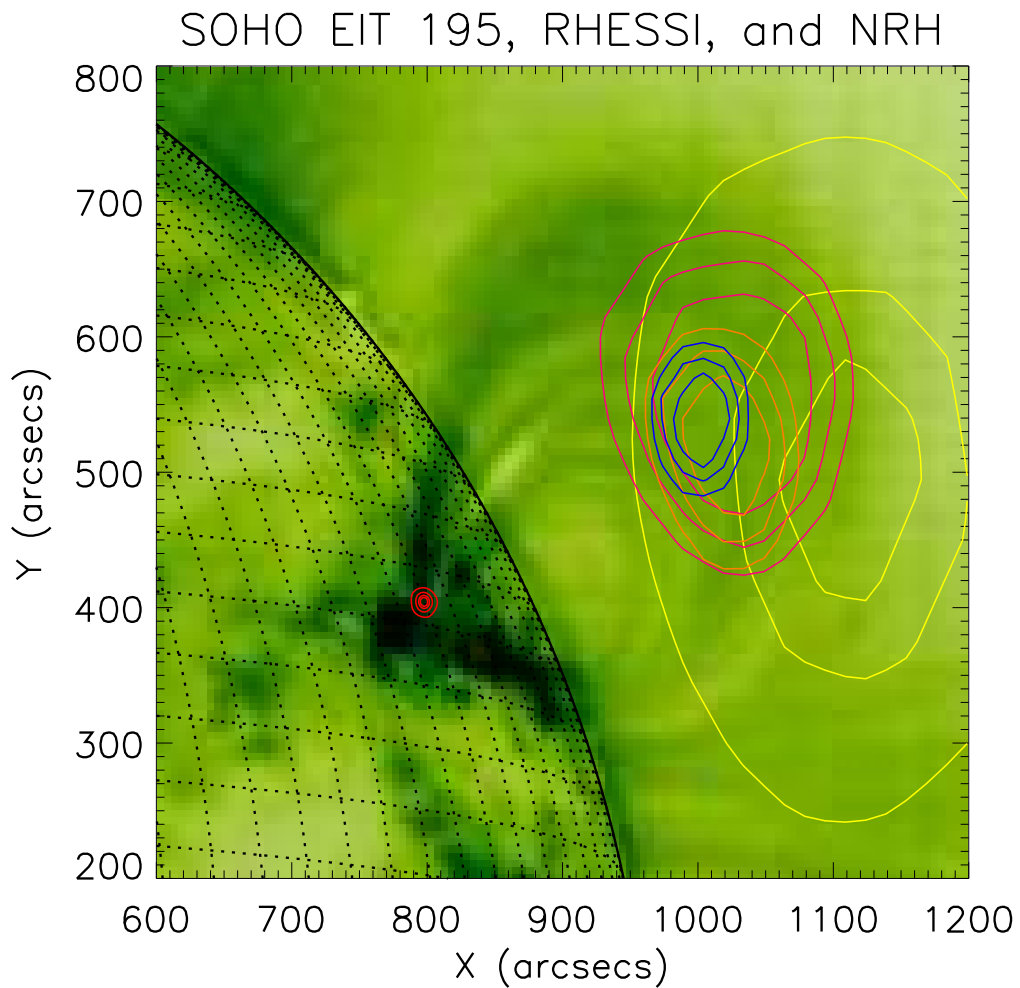
Figure 4.3: The morphology of the April 15, 2002 solar flare. Background is SOHO/EIT 195 image. The small red contour lines at the base of the plasma loops on the left correspond to HXR photons imaged by RHESSI in the 15-30 keV range. The large contours on the right hand side correspond to NRH radio images at frequencies 432 MHz (blue), 327 MHz (orange), 236 MHz (pink), 164 MHz (yellow).
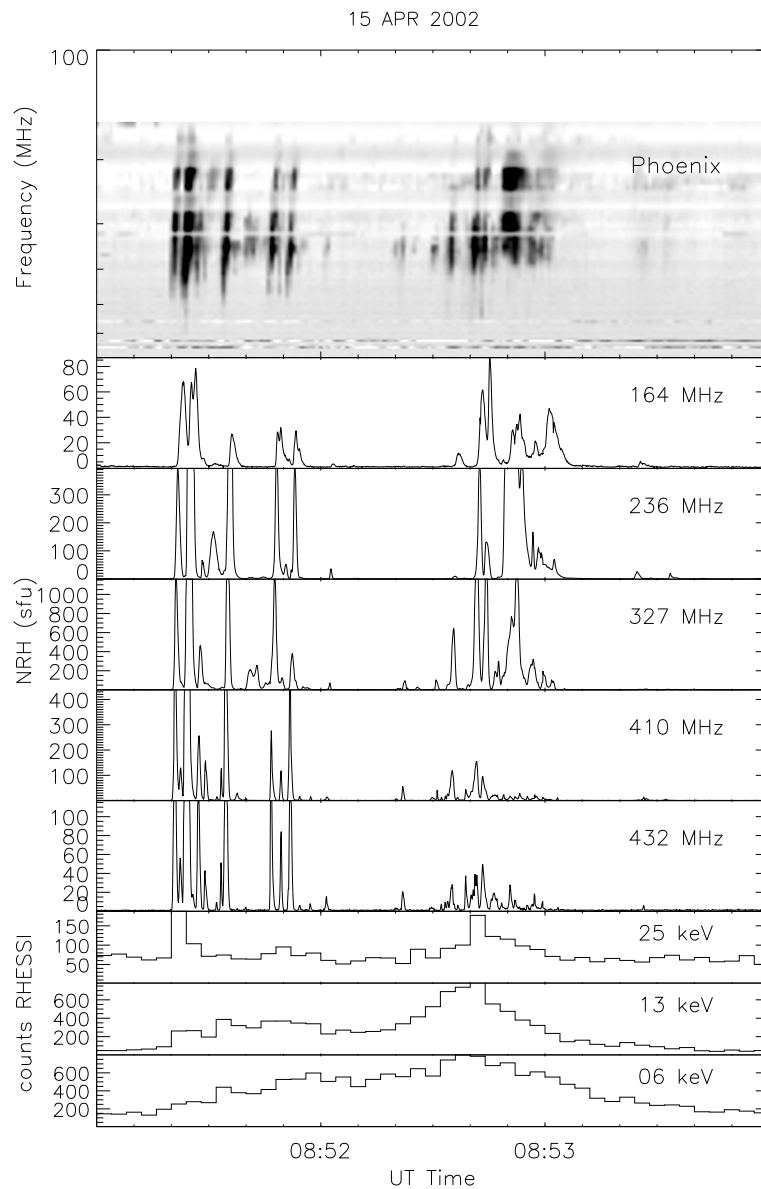
Figure 4.4: Time evolution of the radio and HXR fluxes for the April 15, 2002 solar flare between 08:51 and 08:54 UT. The top panel is the Phoenix-2 radiospectrometer data on a log scale between the frequencies 160 and 700 MHz. The middle panel is the Nançay radioheliograph flux time profiles observed at 5 discrete frequencies from 164 to 432 MHz. The bottom panel are the RHESSI HXR counts/second at the three energy ranges 6-12, 12-25 and 25-50 keV.

Moreover, throughout both periods there is significant radio emission above the threshold frequency.

The temporal evolution of γ and the type III starting frequency is overplotted on the Phoenix-2 data in Figure 4.5 for the time periods defined above. The photon spectral index displays an anti-correlation with the type III starting frequency. A clearer visualisation of this anti-correlation can be seen when both observables are plotted against each other (Figure 4.6). They have a Pearson correlation coefficient of -0.65 due to the starting frequency decreasing as the spectral index increases. This correlation suggests that the two variables are related by a linear fit.

4.3.4 Electron acceleration region parameters

To infer the characteristics of the coronal acceleration region from Equation (4.7) we must use some assumptions to obtain $h_{typeIII}$ and α from the type III starting frequency and γ. To relate the starting height of the type III emission $h_{typeIII}$ to the starting frequency we have used the exponential density model derived in Paesold et al. (2001) which assumes second harmonic emission for a reference height of around 1.5 R_s for 160 MHz emission. To obtain the electron beam spectral index in velocity space from the photon spectral index in energy space, the thick target model (Brown 1971; Brown et al. 2006) was assumed. The electron beam spectral index α can then be calculated from the photon spectral index γ through the simple relationship $\alpha = 2(\gamma + 1)$. The effect of photosphere albedo is ignored as the flare is located close to the limb (Kontar & Jeffrey 2010).

A positive correlation between the electron beam velocity spectral index and the starting height is observed with a Pearson correlation coefficient of 0.62 (Figure 4.7). To investigate the correlation and obtain estimates of the acceleration region properties a linear fit was applied to the data. The routine *mpfitexy* (Markwardt 2009) was used to obtain a fit to the data including observational error (Figure 4.7). Using Equation (4.7) the linear fit infers the acceleration region height and size values of $h_{acc} = 52 \pm 21$ Mm and $d = 10.5 \pm 1.6$ Mm respectively. The larger percentage error of the height in
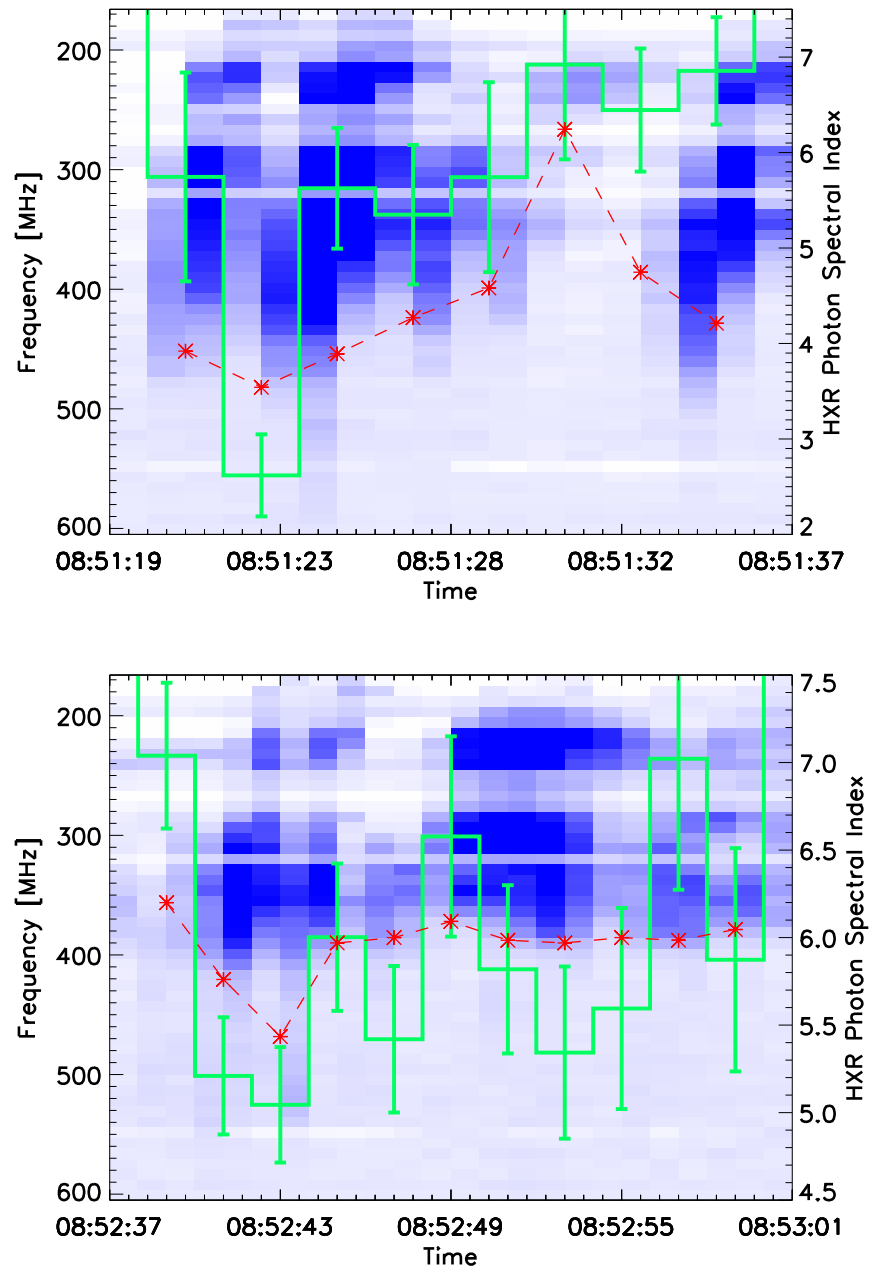
Figure 4.5: HXR spectral index and frequency spectra of the type III burst for two different time periods in the April 15, 2002 event. The starting frequencies are plotted as red stars connected by dashed lines. The HXR spectral indices are plotted as 2 second green bars with error bars in the middle of their integration time.
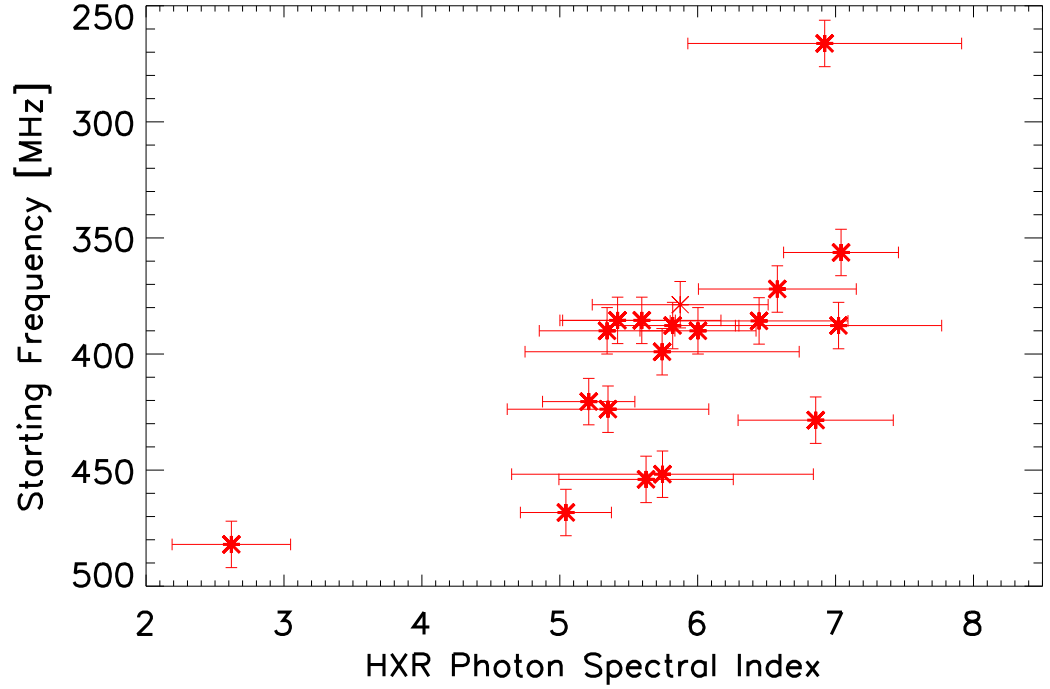
Figure 4.6: Scatter plot of the HXR photon spectral index vs. the starting frequencies of the type III burst. The one sigma observational errors on both spectral index and starting frequency are shown.

relation to the size can be observed in the extremes of the fit shown in Figure 4.7. If this linear relationship is statistically significant the slope has to be greater than zero. We can test the null hypothesis that the slope is zero using the Students t-statistic (e.g. Press et al. 1992). A t-score of 6.56 is found with 19 degrees of freedom. Using a confidence level of 0.01 we can comfortably reject the null hypothesis and say the linear relation is statistically significant.

The radio threshold frequency used to constrain the starting frequencies had a minor effect on the results if changed within reasonable parameters. Different levels ($1.5-2.5\times$ background level) changed the acceleration region properties by around $5-10$ %. Higher threshold frequencies caused higher h_{acc} and lower d with the converse being true. Threshold frequencies < 1.5 or $> 2.5\times$ background level caused unrealis-
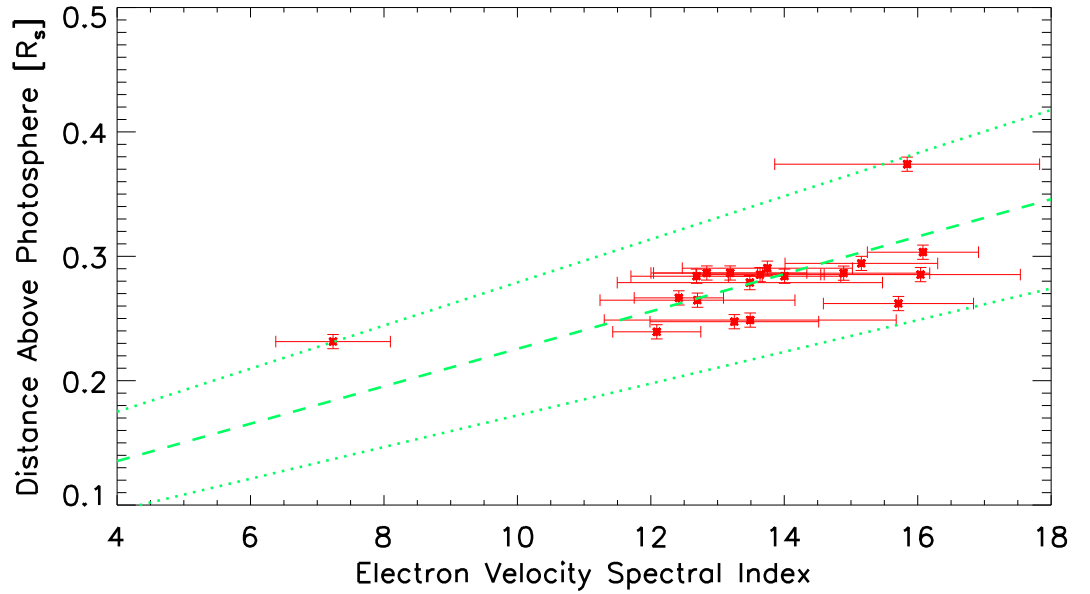
Figure 4.7: Scatter plot of electron beam spectral index in velocity space, α, calculated from the HXR photon spectral index vs. the distance above the photosphere associated with the starting frequencies of the type III burst. The one sigma observational errors on both spectral index and height are shown. The green dashed line is a linear fit to the data including observational error with the green dotted lines showing the extremes of the fit.

tic acceleration region parameters as starting frequencies were either not detected or were detected at high frequencies not corresponding to the visually observed type III emission.

4.4 Beam-plasma numerical simulations

To explore the predictions for acceleration height and size we use numerical simulations of electron beams and induced Langmuir waves in the solar corona. The simulations allow us to validate the observational deductions given the known initial conditions. Moreover, it allows us to explore some of the unknown parameters such as beam density

and the level of Langmuir waves required for radio emission.

4.4.1   Electron beam dynamics

The evolution of accelerated electrons can be considered self-consistently using weak turbulence theory where we have also taken into account binary collisions of energetic electrons with the surrounding plasma. The approach is the same as Chapter 3 explained in Section 3.2 where we consider the time evolution of an electron distribution function $f(v, r, t)$ and the induced Langmuir wave spectral energy density $W(v, r, t)$. For chapter self-consistency, the equations modelling the one-dimensional propagation of the electron beam are

$$\frac{\partial f}{\partial t} + \frac{v}{(r + r_0)^2} \frac{\partial}{\partial r}(r + r_0)^2 f = \frac{4\pi^2 e^2}{m^2} \frac{\partial}{\partial v} \frac{W}{v} \frac{\partial f}{\partial v} + \frac{4\pi n_e e^4}{m_e^2} \ln \Lambda \frac{\partial}{\partial v} \frac{f}{v^2} \tag{4.8}$$

$$\frac{\partial W}{\partial t} + \frac{\partial \omega_L}{\partial k} \frac{\partial W}{\partial r} - \frac{\partial \omega_{pe}}{\partial r} \frac{\partial W}{\partial k} = \frac{\pi \omega_{pe}}{n_e} v^2 W \frac{\partial f}{\partial v} - (\gamma_c + \gamma_L) W + e^2 \omega_{pe}(r) v f \ln \frac{v}{v_{Te}}. \tag{4.9}$$

The background plasma is assumed to be a Maxwellian distribution with thermal velocity v_{Te}, density n_e and plasma frequency ω_{pe}. For a complete description of all the terms in Equations (4.8), (4.9) refer to Section 3.2. The initial spatial distribution of the particles is different from Chapter 3, taking the form of a tent distribution rather than a Gaussian distribution

$$f(v, r, t = 0) = g_0(v) exp\left(\frac{-|r|}{d}\right), \qquad g_0(v) = \frac{n_b(\alpha - 1)}{v_{min}} \left(\frac{v_{min}}{v}\right)^\alpha \tag{4.10}$$

with acceleration region size d, electron beam density n_b and spectral index α. The thermal spectral energy density of Langmuir waves is described by

$$W_{Th}(v, r, t = 0) = \frac{k_B T_e}{4\pi^2} \frac{\omega_{pe}(r)^2}{v^2} \log\left(\frac{v}{v_{Te}}\right). \tag{4.11}$$

This is the expression for the thermal level of a Maxwellian plasma when collisions are weak.

4.4.2   Observational constraints

The values derived from the observations in the previous section constrain some of the key input parameters for the simulations. The starting height, $h_{acc} = 52$ Mm which corresponds to a background density of $n_e = 3 \times 10^9$ cm^{-3} using the exponential density model given in Paesold et al. (2001). This gives a plasma frequency of 500 MHz relating to second harmonic emission of 1000 MHz. The characteristic beam size $d = 10.5$ Mm. The HXR spectral index γ is found from the RHESSI observations (Figure 4.7) which allows us to constrain the electron velocity spectral index as $6 \leq \alpha \leq 16$.

The NRH images of the type III radio emission allow us to observe how the radio source increases with decreasing frequency. Such an observation can provide information regarding the magnetic field expansion. The size of the radio emission at 237 MHz is approximately twice the size of the radio emission at 432 MHz taken at 30% of emission level. This was measured around the two peak times of emission at 08:51:21 UT and 08:52:42 UT. However, the wavelength λ is approximately twice as large at 237 MHz compared to 432 MHz and so the angular resolution of the NRH is increased by two. Moreover, scattering by density inhomogeneities will increases the apparent size of the coronal radio source more at higher wavelengths (Bastian 1994). We thus in the present case *cannot* observationally resolve any significant radial expansion of the magnetic field. Such a scenario is equivalent to type III producing electron beams propagating along thin coronal structures as observed in Trottet et al. (e.g. 1982); Pick et al. (e.g. 2009), or having very small radial expansion of the magnetic field in the low corona. The expansion is much smaller than what would be expected for the inner heliosphere, where the magnetic field expands as a cone with an angle around 40° (e.g. Steinberg et al. 1985).

The density of electron beams responsible for type III emission is believed to be small with Krucker et al. (2007) finding them 0.2% of the density of the downward propagating electron beams responsible for HXR emission above 50 keV. With an initial background density of 3×10^9 cm^{-3} providing the upper limit to the downward propagating electron beam, the upward propagating electron beam was injected with

a density of $n_b = 10^4$ cm^{-3} above 11 keV. However, observations show time dependent intensities of HXR photons which is related to the density of the inducing beam. Such results could indicate the potential need to consider a changing beam density. We note that Equation (4.7) is independent of the density of the electron beam. The starting frequencies found from the upwardly propagating electron beam should thus be insensitive to rather large changes in beam density.

4.4.3   Numerical results

A high level of Langmuir waves is required to induce type III emission. We can estimate the starting height, $h_{typeIII}$, from the simulations through the ratio of Langmuir wave spectral energy density to its initial thermal level $W(v, r, t)/W_{Th}(v, r, t = 0)$ or W/W_{Th}. The first point in phase space when W/W_{Th} exceeds a certain level can give us insight into how electron beams with different spectral indices become unstable.

The numerical results are presented in Figure 4.8 for a variety of different W/W_{Th} levels. By assuming Langmuir waves produce radio emission when they reach a certain level of W/W_{Th}, we can treat the curves in Figure 4.8 in a similar manner to the observational results. By applying a linear fit to each curve, we can obtain an estimate of the initial simulated acceleration region height and size using Equation (4.7). As we know the actual initial simulated values for h_{acc} and d, these estimates allow us to check how accurate the method is for obtaining good estimates. Such a fit also provides a numerical check for the simplified analytical relation Equation (4.7) represents. We find the closest fit to the simulated h_{acc} and d comes from the line where $W/W_{Th} = 10^5$ giving $h_{acc} = 43.5 \pm 5$ Mm and $d = 12.4 \pm 0.6$ Mm. These variables are within 20% and 15% of the original numerical values respectively.

The results in Figure 4.8 show a small variation between the heights corresponding to $10^3 < W/W_{Th} < 10^6$. Provided there are enough electrons to generate sufficient Langmuir waves for radio emission, a change in the beam density has minimal effect on the starting height $h_{typeIII}$. Increasing or decreasing the beam density by one order of magnitude changed the inducing height of $W/W_{Th} = 10^5$ by at most 14 % when
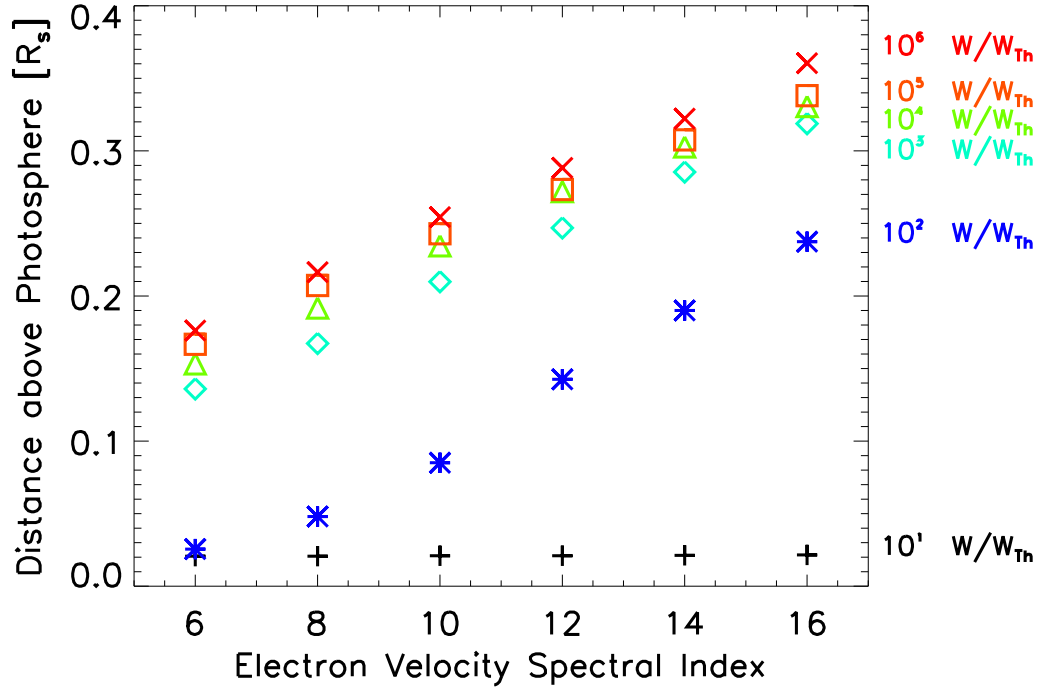
Figure 4.8: Heights corresponding to high levels of Langmuir waves from an unstable beam with density 10^4 cm^{-3}. Symbols and colours correspond to different levels of Langmuir wave growth. Low levels (10 W/W_{Th}) correspond to spontaneous emission of waves. High levels correspond to beam-plasma instability.

$\alpha = 6$ with a mean over all spectral indices of 3 %. Changing the beam density will only vary the level of Langmuir waves which are produced upon the electron beam becoming unstable. This result confirms the density independence of Equation (4.7) where instability of the electron beam is mainly dependent upon the spectral index and size of the electron cloud.

The ratio $W(v, r, t)/W_{Th}(v, r, t = 0)$ also provides information regarding the Langmuir wave phase velocities and onset times when the waves exceeds certain thresholds. As electrons resonantly interact with Langmuir waves, the phase velocity of the Langmuir waves conveys information regarding velocities of the inducing electrons. The phase velocities corresponding to the points in Figure 4.8 get smaller as the electron

spectral index increases (softer spectrum). An example of the velocity variation is presented in Figure 4.9 for the level $W/W_{Th} = 10^5$. Similarly the time required for the beam to induce Langmuir waves at a certain level increases for larger spectral index (Figure 4.9). Beams with larger spectral indices (with the same beam density) have less high energy electrons. We thus expect Langmuir wave emission to be induced by lower energy electrons which take longer to become unstable.

We can explore how the inclusion of an expanding magnetic field would change the simulation results. By ignoring the increase in radio source size at lower frequencies from NRH resolution and scattering we can assume the doubling of size between 432 and 237 MHz is because of a radially expanding magnetic field. Using the assumed density model the magnetic field would then expand as a cone with an angle of $\theta = 6^o$. By then assuming an acceleration site size which is as wide as it is long, we can constrain r_0 in Equation 4.8 to be 30 Mm below the solar surface. Running the simulations and using the same method described above gives estimations of h_{acc} and d which are 12% and 40% of their original values. The expanding magnetic field causes the electron beam to induce a high level of Langmuir waves further away from the acceleration site. The frequencies corresponding to these heights do not agree as well with the observed starting frequencies of the type III bursts.

The results in Figure 4.8 show a small variation between heights corresponding to $10^3 < W/W_{Th} < 10^6$. Changing the beam density will only vary the level of Langmuir waves produced upon the electron beam becoming unstable. Provided there are enough electrons to generate sufficient Langmuir waves for radio emission, a change in the beam density has minimal effect on the starting height $h_{typeIII}$. The level of Langmuir waves induced for different beam densities is shown in Figure 4.10. Changing the beam density by one order of magnitude changes the instability height of the electron beam minimally. The heights corresponding to $W/W_{Th} = 10^4$ change by at most 12 % when $\alpha = 6$ with a mean over all spectral indices of 4 %. This result confirms the density independence of Equation (4.7) where instability of the electron beam is mainly dependent upon the spectral index and size of the electron cloud. It should be emphasized that a certain number density of electrons is required to obtain arbitrarily
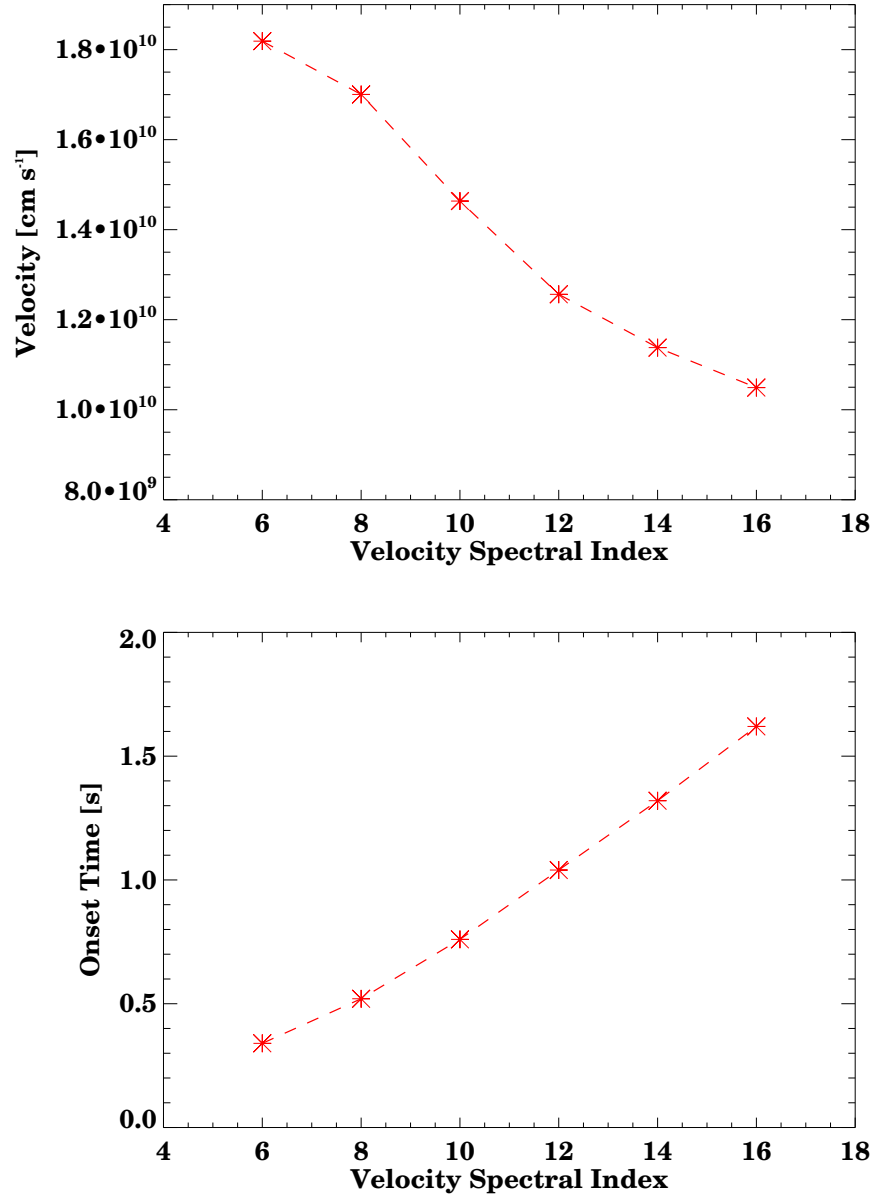
Figure 4.9: Top: electron velocity spectral index plotted against the first phase velocity at which Langmuir waves exceed the threshold $W/W_{Th} = 10^5$. Bottom: electron velocity spectral index plotted against the onset time required for the electron beam to induce Langmuir waves exceeding the threshold $W/W_{Th} = 10^5$.

large amplitudes of Langmuir waves. Simulations with $n_b = 10^3$ cm^{-3} were unable to produce Langmuir wave levels of 10^6 W/W_{Th}. It is only the distance before the electron

beam becomes unstable to Langmuir wave growth that is mostly unaffected by beam density.

4.5 Discussion and conclusions

We used simultaneous observations of radio and hard X-ray emission during a solar flare to gain insight about the acceleration region of energetic electrons. With a simple model we have shown through an analytical relation how the starting height of type III emission and the spectral index of the electron beam can be related to the height and vertical extent of an acceleration region. By combining HXR spectral information with the starting frequencies of the type III bursts, we have derived for our event an estimate on the acceleration site height and size of $h_{acc} = 52 \pm 21$ Mm and $d = 10.5 \pm 1.6$ Mm respectively. We have also used self-consistent numerical simulations of an electron beam which can induce Langmuir waves in a background coronal plasma. The simulations checked our predicted acceleration region values and allowed us to explore unknown parameters of the electron beam and Langmuir wave distributions.

The value found for h_{acc} agrees with values in the range 20 - 50 Mm, deduced from electron time-of-flight analysis for HXR emission (Aschwanden 2002). This scenario indicates an acceleration region in the corona well above where SXR are imaged. The error on h_{acc} is quite large but within the 95 % range of 2-sigma the acceleration region remains within the corona. The value found for d is roughly an order of magnitude higher than previously found before in Aschwanden et al. (1995a). Assuming the relation in Equation (4.7) the acceleration size in Aschwanden et al. (1995a) would not be able to produce significantly varying starting frequency of type III emission given a static acceleration site. Such a small acceleration site predicted by Aschwanden et al. (1995a) may be relevant for type III radio bursts when very little or no evolution of the starting frequency can be observed.

Using the estimates for h_{acc} and d we ran self-consistent numerical simulations of an electron beam able to resonantly induce Langmuir waves in the background coronal plasma. We analysed the distance required for a large magnitude of Langmuir waves
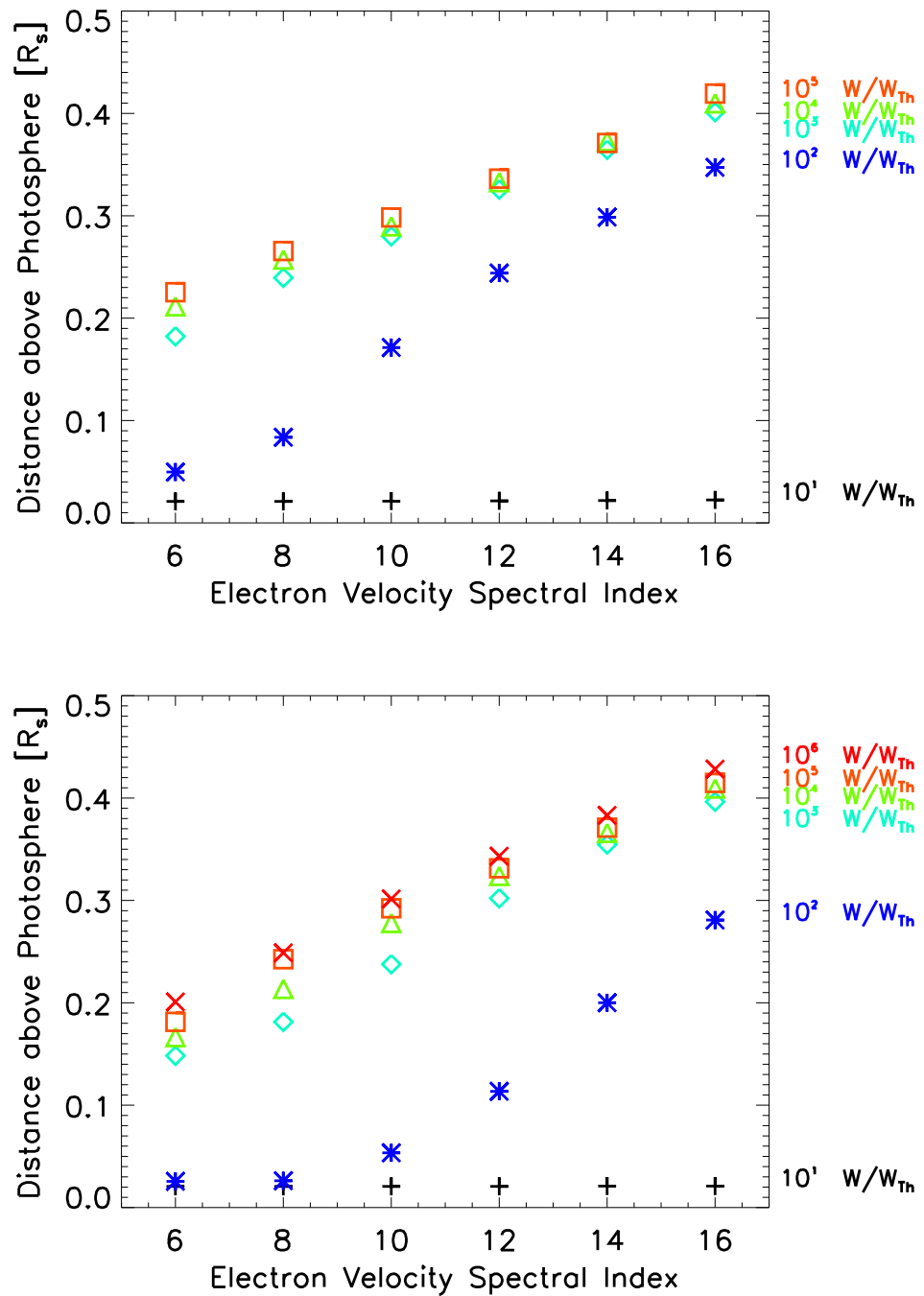
Figure 4.10: Heights corresponding to high levels of Langmuir waves from an unstable beam starting at a minimum altitude of 0.075 R_s with density 10^3 cm^{-3} (top) and 10^5 cm^{-3} (bottom). The heights of Langmuir wave growth are very similar.

to be induced through beam instability for a variety of initial beam spectral indices. A linear fit to the initial beam spectral index and the height associated with large Langmuir wave production gave a good estimation of the initial acceleration region height (within 20%) and the initial acceleration region size (within 15%) . The result fits with the analytical predictions from Equation (4.7) and hence the relation is a powerful diagnostic tool for flare acceleration site properties. In line with the analytical equation the electron beam instability criteria was significantly dependent upon α and d and almost independent on the beam density, which was confirmed by numerical simulations. The simulations also gave an estimate of $W/W_{Th} \geq 10^5$ as the magnitude of Langmuir waves required to produce coherent radio emission. The discrepancies found in the acceleration region properties are due to additional terms present in the numerical simulations which were not present for the simple analytical expression.

It is also possible to explore how a different assumed initial electron beam distribution in space will affect our results. Initially in Equation 4.2 we assumed a tent distribution for the electrons in space. We now consider an initial electron beam distribution which is Gaussian distributed in space such that

$$f(v, r, t = 0) = g_0(v)exp(-r^2/d^2). \tag{4.12}$$

The instability criteria for this distribution was already discussed in Mel'Nik & Kontar (1999) and, assuming small collisional damping, gives the relation

$$h_{typeIII} = 2d\sqrt{\alpha} + h_{acc}. \tag{4.13}$$

The dependence of $h_{typeIII}$ on the square root of the spectral index originates from the r^2 in the exponential for the electron distribution function. Unfortunately the observational errors on electron beam spectral index were too large to discriminate between the two models (Eq (4.2) and Eq (4.12)). Even without observational error estimates such a fit to the data gives $h_{acc} = 33 \pm 51$ Mm and $d = 22 \pm 7$ Mm which is not defined. More detailed observations are thus needed to discriminate between different initial electron distributions in space.

Another assumption we considered was a static acceleration site during the entire event. Kane & Raoult (1981) considered a moving acceleration site which decreased

in altitude to explain why a type III burst's starting frequency increased with time. Assuming the magnetic nature of reconnection, any source movement would typically be at the Alfven velocity. At heights around 100 Mm, this is typically around 1 Mm s^{-1} (Arregui et al. 2007). The Alfven velocity is too slow to account for the varying starting frequencies of the type III emission observed in the April 15th flare considered. Moreover, the acceleration region would have to move upwards and downwards to account for the evolution of the starting frequencies. Our results do not rule out the acceleration region moving in altitude but this will probably not be the dominant process for determining dynamic type III starting frequencies on a time scale of seconds.

Flares associated with the same active region responsible for the 08:51 UT flare on the April 15th 2002 have been analysed previously. Sui & Holman (2003) found a coronal HXR source above the loop-top HXR source during another flare around 23:00 UT on the same day. The high coronal HXR source was initially detected at an altitude of 25 Mm and moved with a speed of 0.3 Mm s^{-1} up to an altitude of 40 Mm as the HXR flux increases. Moreover, the higher energy photons (16-20 keV) are detected at lower altitudes than the low energy photons (6-8 keV). This is indicative of an electron beam streaming down from a high acceleration region with high energy electrons having a larger stopping distance than low energy electrons. Such a scenario fits with the derived high acceleration region $h_{acc} \approx 50$ Mm we found in this study. A similar result was found for other high coronal sources (Liu et al. 2008, 2009) where high energy photons are imaged at lower altitudes than lower energy photons.

In conclusion, we stress that simultaneous HXR and radio observations are a tool to estimate the otherwise unmeasurable sizes of the acceleration site. The results from our first trial of the relation given by Equation 4.7 suggest that this size can be ≈ 10 Mm located at height ≈ 50 Mm, occupying a substantial fraction of the corona. The size is larger than the HXR sources which are typically observed with RHESSI and in the range between a few Mm up to a few tens of Mm (Emslie et al. 2003). Future studies should have a higher flux of HXR to better constrain the deduced electron beam spectral index.

Chapter 5

Conclusions and future work

The motivation for this thesis was to understand better the transport of energetic keV electrons as they propagate from the Sun to the Earth. In Chapter 2 we investigated the approximate broken power-law fluence spectra of electron beams at the Earth. Chapter 3 saw our model being improved to simulate realistic beam densities by taking into account electron-electron Coulomb collisions and the radial expansion of the inner heliosphere magnetic field. Chapter 3 also took background electron density fluctuations into account and analysed their effect on the resultant spectral indices of electron beam broken power-law fluence spectra at the Earth. Chapter 4 investigated the initial instability of solar electron beams. Using a combination of observational data and numerical simulations, Chapter 4 predicted both acceleration region heights and sizes. Whilst all chapters provided necessary conclusions and future considerations this chapter will provide some further insight into related type III radio emission properties and other possible future work.

5.1 Type III frequency drift rate

Numerical simulations of electron beams propagating from the Sun to the Earth provide sample distributions of the Langmuir wave energy density. As Langmuir waves are required to generate the coherent type III radio waves, we can use the Langmuir

wave distribution as a proxy value for the type III temporal evolution. Such an approximation provides some insight into type III frequency drift rate.

The spatial position of the maximum Langmuir wave energy density at every point in time can be used as an initial estimation of the frequency drift rate. To illustrate this we can use the data from the simulation in Section 3.3 with an unperturbed background electron density gradient. Figure 5.1 includes the background plasma frequency where the maximum Langmuir wave energy density was found at every point in time. A power-law fit to the green curve in Figure 5.1 is also displayed for frequency f in MHz vs time t in seconds, giving the relation $f = 230t^{-1.09}$. Evolution of the maximum in Langmuir wave energy density resembles a power-law very closely as the errors are very small. Extending the comparison to distance vs time we find a power-law fit to the data giving $x = 43t^{0.96}$ where x is in Mm and t is in seconds. Assuming a constant speed as x is nearly proportional to t, we get a velocity of 43 Mm s^{-1} which is very close to the minimum velocity in the simulations. Such a result can be explained by considering Equation 3.6 for the wave energy density. We observe that waves with low phase velocities have the highest energy. This, coupled with the increased number of electrons at low velocities leads to the majority of the energy contributing to Langmuir wave energy density coming from low phase velocity Langmuir waves. Such Langmuir waves are not the most efficient at producing second harmonic radio emission (see Section 1.3). Moreover, the peak of Langmuir wave energy density may not necessarily translate to the peak in radio wave intensity.

An alternative approximation of the drift rate of type III radio bursts is the initial onset of a high level of Langmuir wave energy density above the thermal level. Such an approximation is similar to the observational method for estimating type III drift frequency used by Alvarez & Haddock (1973) (referenced now as AH73). Figure 5.1 displays the observational result from AH73 who used the initial onset time of type III radio emission at specific frequencies (Section 1.4.2). The observational result gives the frequency vs time relation of $f = 240t^{-1.19}$. We can again use the data from Section 3.3 and the result from Chapter 4 regarding an expected threshold of 10^5 W/W_{Th} for type III emission onset. Figure 5.1 includes the background plasma frequency in MHz
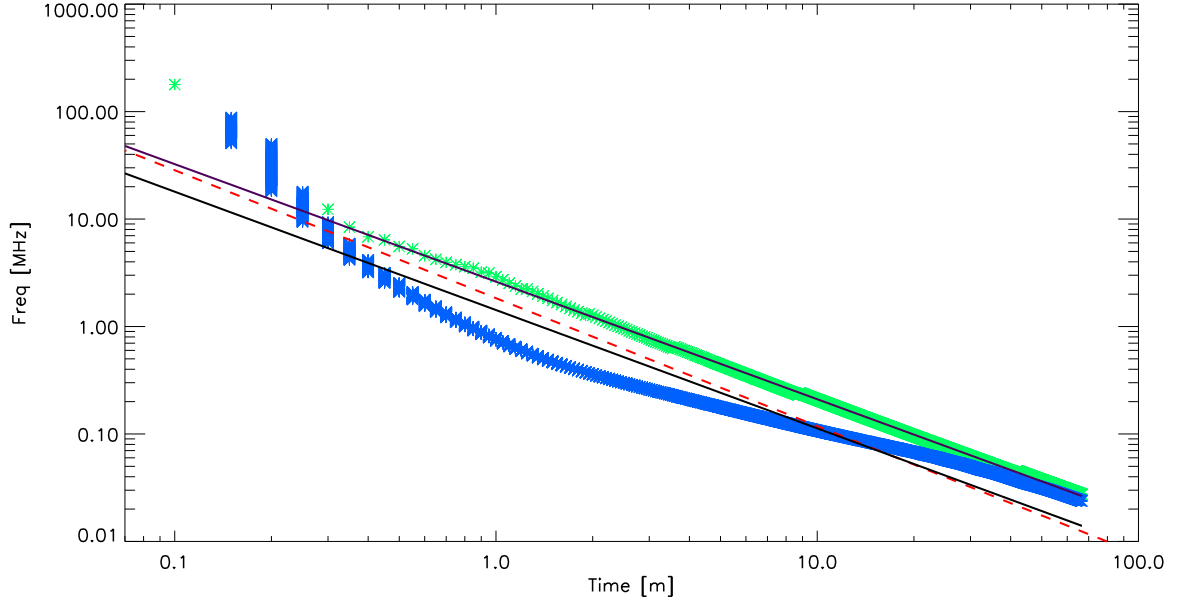
Figure 5.1: Background plasma frequency vs time of the maximum Langmuir wave energy density $E_w(r,t)/E_w(r,t=0)$ (green) and the onset of 10^5 $E_w(r,t)/E_w(r,t-0)$ (blue). Power-law fit to the data are also shown in purple and black respectively. The red dashed line is the frequency vs onset time observational fit from Alvarez & Haddock (1973) between 550 MHz and 74 KHz. The banding at early times on the blue curve is an artefact of low temporal resolution.

where Langmuir wave energy density initially reaches this threshold at every point in time. A power-law fit has also been displayed giving the relation $f = 129t^{-1.1}$ over the frequencies 89 MHz to 25 kHz. The simulation time of 80 minutes led to data only being written every 5 simulated seconds. A consequence of saving data every 5 seconds is the discrete nature of the blue curve in Figure 5.1 at early times. The observational result from AH73 very closely resembles the power-law fit to the simulated data. We note the simulation curve does not resemble a straight line in log space and thus probably does not correspond to a constant velocity. One sigma errors of the power-law fit on the simulation data are actually lower than the errors on the data presented by AH73 and significantly lower than the errors on the other data which AH73 extrapolate their

fit to.

It is apparent that estimating the drift frequency of type III radio bursts as a power-law is an approximation of a more complex, frequency dependent relation. Moreover, Melrose (1980c) reports a different power-law relation in the corona to the one from AH73. From the insight obtained in Chapter 3 regarding beam evolution, the result is not surprising. Electron kinetic energies contributing to the beam-plasma structure (BPS) responsible for type III emission vary throughout Sun-Earth propagation. The maximum electron energy is high (around 50 keV) in the corona and much lower (around 5 keV) at the Earth. We thus expect a reduction in the velocity which the BPS travels through the heliosphere. Figure 5.1 displays such properties with the maximum velocity of the BPS being reached after 1 minute and then decreasing during the rest of its travel to velocities near the minimum simulated.

5.2   Electron distribution function

A new NASA spacecraft, Solar Probe Plus (SPP) is planned for launch around 2016. Its mission will be to fly close to the Sun (roughly 9 R_s) and take in-situ measurements of the inner heliosphere. An ESA spacecraft Solar Orbiter (SO) is also planned for launch at similar dates and will fly to around 0.2 AU while taking similar in-situ particle observations. Measurements like these have already been taken by the Helios spacecrafts but SPP and SO will be going much closer to the Sun and have state-of-the-art particle detection instruments. For this reason the prediction of how electron beams evolve in the inner heliosphere is particularly topical. These probes will collect crucial in-situ data to test our theory and understanding of electron transport mechanisms in several year's time.

The next evolution of this work will be to predict the spectral and energetic evolution of an electron beam-plasma structure as it leaves the Sun and travels towards Earth. For the beam-plasma structure to more closely resemble real solar electron

beams, the injection will have a temporal component of the form

$$f(v, x, t) = g_o(v) \exp\left(\frac{-x^2}{d^2}\right) \frac{1}{2\sqrt{\pi(\tau_1 + \tau_2)}} \exp\left(\frac{-(t - t_0)^2}{\tau^2}\right) \qquad (5.1)$$

where $\tau = \tau_1$ in the rise time $t < t_0$ and $\tau = \tau_2$ in the decay time $t \geq t_0$. τ_1 and τ_2 represent the rise and decay characteristic times with $\tau_1 < \tau_2$. Observational values for τ_1 and τ_2 can be obtained from HXR measurements of solar flares to give an accurate representation of electron beam release from the corona.

A consequence of an electron beam generating a break in the electron spectra during transport is the reduction in beam energy. Energy is transferred to Langmuir waves during transport. While the electrons are able to re-absorb some of this energy, part of the energy is lost to the background plasma through Landau damping (see Section 2.4). Another goal of this work will be to find how the energy in both the beam-plasma structure and the lost energy through Landau damping are a function of distance and time. The predicted bulk of the energy loss will be close to the Sun as this is the location where an electron beam generates the highest intensity of Langmuir waves.

The evolution of the spectral break is also interesting as the break is not simply formed instantly when the beam leaves the solar corona. Instead the electron beam forms a plateau in velocity space during intense production of Langmuir waves. This plateau dissipates with distance as the high energy electrons become too rarefied to continue wave-particle interactions. Moreover, the inner heliosphere turbulence restricts the growth of Langmuir waves and alters how the spectral of the electron beam evolves with distance (Reid & Kontar 2010).

5.3   Type III rise and decay rates

It was reported in section 1.4.2 that observationally type III emission takes the form of a Gaussian total rise time t_e followed by a power-law e-folding decay time t_d. We find numerically the energy density of Langmuir waves displays a Gaussian total rise time but does not display a power-law decay time. Moreover, we find numerically that Langmuir wave energy density decays rather abruptly compared to the onset

time in contradiction to observations. Such a contradiction could be linked to the lack of a temporal injection of electrons. The abrupt decrease of Langmuir waves energy density at any point in space is directly related to the electron beam moving away and re-absorbing Langmuir wave energy. Extending the electron beam in space through a prolonged temporal injection would spread the Langmuir wave energy density in time. Some Langmuir waves are unable to be re-absorbed by the electron beam when background electron density turbulence is considered. They do not, however, correspond to a large magnitude of Langmuir wave energy density. Further study is required to see if such Langmuir waves could be responsible for the decay time of type III emission.

5.4   Radio X-ray further study

The work done in Chapter 3 was successful in determining a reasonable estimate for not only the acceleration region height but also its characteristic size. Unfortunately the errors on the HXR data available were large, leading to substantial errors on the results. In spite of this, the results seemed to correspond with the data when the observational errors were not taken into account.

I propose to take this aspect forward in the near future and create a new study on a variety of different solar flare events where the HXR and the radio emission is correlated in time. Such events will hopefully have more intense HXR emission and also be extended temporally. Better observation data obtained from such flares should not only provide better estimates but will provide more than one observational prediction of flare acceleration region properties.

It should also be possible to verify these new results by using numerical simulations. The results of such simulations will also help us to understand better the initial electron beam dynamics in the corona. Depending on the quality of the observational results, it may also be prudent to extend the numerical simulations to take into account an entire event. Modelling such an event would require either a series of discrete bursts with different spectral indices or a time injected electron beam with an initial spectral

index that evolves in time.

Another candidate for considering the starting frequency of radio bursts are type III-L bursts (Cane et al. 2002; MacDowall et al. 2009). Such radio bursts happen late in comparison to HXR emission. They also have the property of starting at lower frequencies, around 1 MHz. Their starting frequency could be related to either the temporal, spatial or energetics of the electron beam acceleration or it could be a property of the high coronal plasma.

5.5   Type III frequency ranges

As reviewed in Chapter 1, type III bursts can extend to the kHz frequencies, becoming interplanetary (IP) bursts. The properties of such bursts provide further insight into inducing electron beams that are able to support Langmuir wave growth at distances of 1 AU or greater. This avenue of research can be generalised to find the stopping frequency of type III radio bursts. The stopping frequency not only determines why bursts become interplanetary but also determines at what distance in the inner heliosphere radio emission will cease.

Properties of the background electron density and the electron beam can be responsible for the observed stopping frequency of type III radio bursts. A lack of electron beam density will stop the production of Langmuir waves. From Chapter 3 the coronal and inner heliospheric magnetic field expansion properties contribute to the rarefication of the electron beam during transport. Accelerated electron beams without enough initial density may be able to briefly generate Langmuir waves in the corona but stop when the electron beam expands in space. Another candidate contributing to stopping frequency is the local background electron plasma turbulence. It has been observed (e.g. Buttighoffer et al. 1995) that electrons can stream into the heliosphere via channels in the solar wind which have low levels of background turbulence. Such low levels would provide favourable conditions for Langmuir waves to be induced at distances ≥ 1 AU and hence produce IP bursts. As shown in Chapter 4 the spectral index of the electron beam has a huge influence on the starting frequency of radio bursts. The

spectral index will also contribute to the stopping frequency as it determines the spectral distribution of electrons. Not enough electrons at velocities $\geq 2\ v_{Te}$ will cause a lack of Langmuir waves through Landau damping from the background plasma.

5.6 Closing statement

In summary, the work described in this thesis illustrates that modelling the transport of electrons from the Sun to the Earth and beyond is a complex problem involving non-linear, interacting electromagnetic systems. Through the use of simulations, a better understanding of some aspects of the generation and transport has been obtained. The wide variety of phenomena exhibited by solar radio bursts and observed electron fluence measurements show that the complexity of the electron beam transport has not yet been fully modelled.

Bibliography

Alvarez, H. & Haddock, F. T. 1973, Solar Physics, 29, 197

Anderson, K. A., Lin, R. P., Potter, D. W., & Heetderks, H. D. 1978, IEEE Transactions on Geoscience Electronics, 16, 153

Arnoldy, R. L., Kane, S. R., & Winckler, J. R. 1968, Astrophysical Journal, 151, 711

Arregui, I., Andries, J., Van Doorsselaere, T., Goossens, M., & Poedts, S. 2007, Astronomy and Astrophysics, 463, 333

Arzner, K. & Benz, A. O. 2005, Solar Physics, 231, 117

Aschwanden, M. J. 2002, Space Science Reviews, 101, 1

Aschwanden, M. J. & Benz, A. O. 1997, Astrophysical Journal, 480, 825

Aschwanden, M. J., Benz, A. O., Dennis, B. R., & Schwartz, R. A. 1995a, Astrophysical Journal, 455, 347

Aschwanden, M. J., Montello, M. L., Dennis, B. R., & Benz, A. O. 1995b, Astrophysical Journal, 440, 394

Aschwanden, M. J., Schwartz, R. A., & Dennis, B. R. 1998, Astrophysical Journal, 502, 468

Aurass, H. & Klein, K. 1997, Astronomy and Astrophysics, Supplement, 123, 279

Aurass, H., Klein, K., Zlotnik, E. Y., & Zaitsev, V. V. 2003, Astronomy and Astrophysics, 410, 1001

Bárta, M. & Karlický, M. 2001, Astronomy and Astrophysics, 379, 1045

Bastian, T. S. 1994, Astrophysical Journal, 426, 774

Bastian, T. S., Benz, A. O., & Gary, D. E. 1998, Annual Review of Astronomy and Astrophysics, 36, 131

Battaglia, M., Grigis, P. C., & Benz, A. O. 2005, Astronomy and Astrophysics, 439, 737

Benz, A., ed. 2002, Astrophysics and Space Science Library, Vol. 279, Plasma Astrophysics, second edition

Benz, A. O. 1977, Astrophysical Journal, 211, 270

Benz, A. O. 2008, Living Reviews in Solar Physics, 5, 1

Benz, A. O., Barrow, C. H., Dennis, B. R., et al. 1983, Solar Physics, 83, 267

Benz, A. O., Grigis, P. C., Csillaghy, A., & Saint-Hilaire, P. 2005, Solar Physics, 226, 121

Benz, A. O., Guedel, M., Isliker, H., Miszkowicz, S., & Stehling, W. 1991, Solar Physics, 133, 385

Benz, A. O., Perret, H., Saint-Hilaire, P., & Zlobec, P. 2006, Advances in Space Research, 38, 951

Biskamp, D. 1986, Physics of Fluids, 29, 1520

Boischot, A. 1957, C. R. Acad. Sci., 244, 1326

Bougeret, J., Caroubalos, C., Mercier, C., & Pick, M. 1970, Astronomy and Astrophysics, 6, 406

Bougeret, J., Kaiser, M. L., Kellogg, P. J., et al. 1995, Space Science Reviews, 71, 231

Brown, J. C. 1971, Solar Physics, 18, 489

Brown, J. C., Emslie, A. G., Holman, G. D., et al. 2006, Astrophysical Journal, 643, 523

Brown, J. C. & Kontar, E. P. 2005, Advances in Space Research, 35, 1675

Buttighoffer, A., Pick, M., Roelof, E. C., et al. 1995, Journal of Geophysics Research, 100, 3369

Cane, H. V., Erickson, W. C., & Prestage, N. P. 2002, Journal of Geophysical Research (Space Physics), 107, 1315

Cane, H. V., Sheeley, Jr., N. R., & Howard, R. A. 1987, Journal of Geophysics Research, 92, 9869

Celnikier, L. M., Harvey, C. C., Jegou, R., Moricet, P., & Kemp, M. 1983, Astronomy and Astrophysics, 126, 293

Celnikier, L. M., Muschietti, L., & Goldman, M. V. 1987, Astronomy and Astrophysics, 181, 138

Cerenkov, P. A. 1934, C.R. Acad. Sci. U.S.S.R., 2, 451

Chernov, G. P., Kaiser, M. L., Bougeret, J., Fomichev, V. V., & Gorgutsa, R. V. 2007, Solar Physics, 241, 145

Coles, W. A. 1978, Space Science Reviews, 21, 411

Coles, W. A. & Harmon, J. K. 1989, Astrophysical Journal, 337, 1023

Coles, W. A., Liu, W., Harmon, J. K., & Martin, C. L. 1991, Journal of Geophysics Research, 96, 1745

Craig, I. J. D. & Brown, J. C. 1986, Inverse problems in astronomy: A guide to inversion strategies for remotely sensed data, ed. Craig, I. J. D. & Brown, J. C.

de La Noe, J. & Boischot, A. 1972, Astronomy and Astrophysics, 20, 55

Dennis, B. R., Benz, A. O., Ranieri, M., & Simnett, G. M. 1984, Solar Physics, 90, 383

Dennis, B. R. & Schwartz, R. A. 1989, Solar Physics, 121, 75

Drake, J. F., Swisdak, M., Che, H., & Shay, M. A. 2006, Nature, 443, 553

Drummond, W. E. & Pines, D. 1962, Nucl. Fusion Suppl., 3, 1049

Dulk, G. A. 1985, Annual Review of Astronomy and Astrophysics, 23, 169

Dulk, G. A., Gary, D. E., & Suzuki, S. 1980, Astronomy and Astrophysics, 88, 218

Dulk, G. A., Leblanc, Y., Robinson, P. A., Bougeret, J., & Lin, R. P. 1998, Journal of
    Geophysics Research, 103, 17223

Dulk, G. A., Steinberg, J. L., & Hoang, S. 1984, Astronomy and Astrophysics, 141, 30

Dulk, G. A. & Suzuki, S. 1980, Astronomy and Astrophysics, 88, 203

Ellis, G. R. A. 1969, Australian Journal of Physics, 22, 177

Ellis, G. R. A. & McCulloch, P. M. 1967, Australian Journal of Physics, 20, 583

Emslie, A. G. 1978, Astrophysical Journal, 224, 241

Emslie, A. G. 1989, Solar Physics, 121, 105

Emslie, A. G., Kontar, E. P., Krucker, S., & Lin, R. P. 2003, Astrophysical Journal,
    Letters, 595, L107

Ergun, R. E., Larson, D., Lin, R. P., et al. 1998, Astrophysical Journal, 503, 435

Evans, L. G., Fainberg, J., & Stone, R. G. 1973, Solar Physics, 31, 501

Fletcher, L. & Hudson, H. S. 2002, Solar Physics, 210, 307

Ginzburg, V. L. & Zhelezniakov, V. V. 1958, Soviet Astronomy, 2, 653

Gopalswamy, N., Aguilar-Rodriguez, E., Yashiro, S., et al. 2005, Journal of Geophysical
    Research (Space Physics), 110, 12

Gopalswamy, N., Kaiser, M. L., Thompson, B. J., et al. 2000, Geophysics Research Letters, 27, 1427

Gopalswamy, N. & Kundu, M. R. 1987, Solar Physics, 111, 347

Gopalswamy, N., Thompson, W. T., Davila, J. M., et al. 2009, Solar Physics, 259, 227

Gopalswamy, N., Xie, H., Mäkelä, P., et al. 2010, Astrophysical Journal, 710, 1111

Gosling, J. T., Skoug, R. M., & McComas, D. J. 2003, Geophysics Research Letters, 30, 130000

Grigis, P. C. & Benz, A. O. 2004, Astronomy and Astrophysics, 426, 1093

Grigis, P. C. & Benz, A. O. 2008, Astrophysical Journal, 683, 1180

Grognard, R. J.-M. 1982, Solar Physics, 81, 173

Grognard, R. J.-M. 1985, Propagation of electron streams (Solar Radiophysics: Studies of Emission from the Sun at Metre Wavelengths), 253–286

Gurnett, D. A. & Anderson, R. R. 1976, Science, 194, 1159

Gurnett, D. A. & Anderson, R. R. 1977, Journal of Geophysics Research, 82, 632

Hamilton, R. J. & Petrosian, V. 1992, Astrophysical Journal, 398, 350

Hamilton, R. J., Petrosian, V., & Benz, A. O. 1990, Astrophysical Journal, 358, 644

Hannah, I. G., Kontar, E. P., & Sirenko, O. K. 2009, Astrophysical Journal, Letters, 707, L45

Harvey, C. C., Manning, R., Etcheto, J., de Javel, Y., & Petit, M. 1978, IEEE Transactions on Geoscience Electronics, 16, 231

Ho, G. C., Roelof, E. C., Mason, G. M., Lario, D., & Mazur, J. E. 2003, Advances in Space Research, 32, 2679

Hollweg, J. V. 1970, Journal of Geophysics Research, 75, 3715

Holman, G. D. 1985, Astrophysical Journal, 293, 584

Holman, G. D. & Pesses, M. E. 1983, Astrophysical Journal, 267, 837

Holman, G. D., Sui, L., Schwartz, R. A., & Emslie, A. G. 2003, Astrophysical Journal, Letters, 595, L97

Jelley, J. V. 1958, Cerenkov radiation and its applications (Permagon Press.)

Kahler, S. & Ragot, B. R. 2006, Astrophysical Journal, 646, 634

Kai, K., Melrose, D. B., & Suzuki, S. 1985, Storms, ed. McLean, D. J. & Labrum, N. R., 415–441

Kane, S. R. 1972, Solar Physics, 27, 174

Kane, S. R. 1981, Astrophysical Journal, 247, 1113

Kane, S. R., Benz, A. O., & Treumann, R. A. 1982, Astrophysical Journal, 263, 423

Kane, S. R. & Raoult, A. 1981, Astrophysical Journal, Letters, 248, L77

Karpman, V. I. & Istomin, J. N. 1974, Physics Letters A, 48, 197

Kellogg, P. J., Goetz, K., Monson, S. J., et al. 2009, Journal of Geophysical Research (Space Physics), 114, 2107

Kellogg, P. J. & Horbury, T. S. 2005, Annales Geophysicae, 23, 3765

Kerdraon, A. & Delouis, J. 1997, in Lecture Notes in Physics, Berlin Springer Verlag, Vol. 483, Coronal Physics from Radio and Space Observations, ed. G. Trottet, 192–+

Kliem, B. 1994, Astrophysical Journal, Supplement, 90, 719

Kontar, E. P. 2001a, Solar Physics, 202, 131

Kontar, E. P. 2001b, Astronomy and Astrophysics, 375, 629

Kontar, E. P. 2001c, Computer Physics Communications, 138, 222

Kontar, E. P. 2001d, Plasma Physics and Controlled Fusion, 43, 589

Kontar, E. P. & Jeffrey, N. L. S. 2010, Astronomy and Astrophysics, 513, L2+

Kontar, E. P., Lapshin, V. I., & Mel'Nik, V. N. 1998, Plasma Physics Reports, 24, 772

Kontar, E. P. & MacKinnon, A. L. 2005, Solar Physics, 227, 299

Kontar, E. P. & Pécseli, H. L. 2002, Physical Review E, 65, 066408

Kontar, E. P., Piana, M., Massone, A. M., Emslie, A. G., & Brown, J. C. 2004, Solar Physics, 225, 293

Kontar, E. P. & Reid, H. A. S. 2009, Astrophysical Journal, Letters, 695, L140

Krasnoselskikh, V. V., Lobzin, V. V., Musatenko, K., et al. 2007, Journal of Geophysical Research (Space Physics), 112, 10109

Krucker, S., Kontar, E. P., Christe, S., & Lin, R. P. 2007, Astrophysical Journal, Letters, 663, L109

Krucker, S., Larson, D. E., Lin, R. P., & Thompson, B. J. 1999, Astrophysical Journal, 519, 864

Krucker, S., Oakley, P. H., & Lin, R. P. 2009, Astrophysical Journal, 691, 806

Labrum, N. R. & Stewart, R. T. 1970, Proceedings of the Astronomical Society of Australia, 1, 316

Le Chat, G., Issautier, K., Meyer-Vernet, N., et al. 2010, Twelfth International Solar Wind Conference, 1216, 316

Ledenev, V. G., Zverev, E. A., & Starygin, A. P. 2004, Solar Physics, 222, 299

Li, B., Robinson, P. A., & Cairns, I. H. 2006a, Physical Review Letters, 96, 145005

Li, B., Robinson, P. A., & Cairns, I. H. 2006b, Physics of Plasmas, 13, 082305

Lin, R. P. 1985, Solar Physics, 100, 537

Lin, R. P. 1990, in IAU Symposium, Vol. 142, Basic Plasma Processes on the Sun, ed.
E. R. Priest & V. Krishan, 467–479

Lin, R. P. 2000, in American Institute of Physics Conference Series, Vol. 528, Acceleration and Transport of Energetic Particles Observed in the Heliosphere, ed.
R. A. Mewaldt, J. R. Jokipii, M. A. Lee, E. Möbius, & T. H. Zurbuchen , 32–38

Lin, R. P., Anderson, K. A., Ashford, S., et al. 1995, Space Science Reviews, 71, 125

Lin, R. P., Anderson, K. A., & Cline, T. L. 1972, Physical Review Letters, 29, 1035

Lin, R. P., Dennis, B. R., Hurford, G. J., et al. 2002, Solar Physics, 210, 3

Lin, R. P., Evans, L. G., & Fainberg, J. 1973, Astrophysics Letters, 14, 191

Lin, R. P., Larson, D., McFadden, J., et al. 1996, Geophysics Research Letters, 23,
1211

Lin, R. P., Levedahl, W. K., Lotko, W., Gurnett, D. A., & Scarf, F. L. 1986, Astrophysical Journal, 308, 954

Lin, R. P., Potter, D. W., Gurnett, D. A., & Scarf, F. L. 1981, Astrophysical Journal,
251, 364

Litvinenko, Y. E. 2003, in Lecture Notes in Physics, Berlin Springer Verlag, Vol. 612,
Energy Conversion and Particle Acceleration in the Solar Corona, ed. L. Klein, 213–229

Liu, W., Petrosian, V., Dennis, B. R., & Jiang, Y. W. 2008, Astrophysical Journal,
676, 704

Liu, Y., Luhmann, J. G., Bale, S. D., & Lin, R. P. 2009, Astrophysical Journal, Letters,
691, L151

MacDowall, R. J., Richardson, I. G., Hess, R. A., & Thejappa, G. 2009, in IAU Symposium, Vol. 257, IAU Symposium, ed. N. Gopalswamy & D. F. Webb, 335–340

Magelssen, G. R. & Smith, D. F. 1977, Solar Physics, 55, 211

Maia, D., Pick, M., Hawkins, III, S. E., & Krucker, S. 2001, Astrophysical Journal, 560, 1058

Maksimovic, M., Zouganelis, I., Chaufray, J., et al. 2005, Journal of Geophysical Research (Space Physics), 110, 9104

Mann, G., Jansen, F., MacDowall, R. J., Kaiser, M. L., & Stone, R. G. 1999, Astronomy and Astrophysics, 348, 614

Manoharan, P. K. 1993, Solar Physics, 148, 153

Manoharan, P. K. 2010, in Magnetic Coupling between the Interior and Atmosphere of the Sun, ed. S. S. Hasan & R. J. Rutten, 324–331

Manoharan, P. K., Kojima, M., & Misawa, H. 1994, Journal of Geophysics Research, 99, 23411

Markwardt, C. B. 2009, in Astronomical Society of the Pacific Conference Series, Vol. 411, Astronomical Society of the Pacific Conference Series, ed. D. A. Bohlender, D. Durand, & P. Dowler, 251–+

Maroulis, D., Dumas, G., Bougeret, J. L., Caroubalos, C., & Poquérusse, M. 1993, Solar Physics, 147, 359

Marsch, E. 2006, Living Reviews in Solar Physics, 3, 1

Marsch, E. & Tu, C. 1990, Journal of Geophysics Research, 95, 11945

Maxwell, A. & Swarup, G. 1958, Nature, 181, 36

McCready, L. L., Pawsey, J. L., & Payne-Scott, R. 1947, Royal Society of London Proceedings Series A, 190, 357

McDonald, L., Harra-Murnion, L. K., & Culhane, J. L. 1999, Solar Physics, 185, 323

McLean, D. J. 1971, Australian Journal of Physics, 24, 201

Mel'Nik, V. N. 1995, Plasma Physics Reports, 21, 89

Melnik, V. N., Konovalenko, A. A., Brazhenko, A. I., et al. 2010, in American Institute of Physics Conference Series, Vol. 1206, American Institute of Physics Conference Series, ed. S. K. Chakrabarti, A. I. Zhuk, & G. S. Bisnovatyi-Kogan, 450–454

Mel'Nik, V. N. & Kontar, E. P. 1999, New Astronomy, 4, 41

Melrose, D. B. 1980a, Solar Physics, 67, 357

Melrose, D. B. 1980b, Plasma astrohysics. Nonthermal processes in diffuse magnetized plasmas - Vol.1: The emission, absorption and transfer of waves in plasmas; Vol.2: Astrophysical applications (New York: Gordon and Breach, 1980)

Melrose, D. B. 1980c, Plasma astrophysics: Nonthermal processes in diffuse magnetized plasmas. Volume 2 - Astrophysical applications (New York, Gordon and Breach Science Publishers, 1980. 430 p.)

Melrose, D. B. 1982, Solar Physics, 79, 173

Melrose, D. B. 1983, Solar Physics, 87, 359

Melrose, D. B. 1985, Plasma emission mechanisms (Solar Radiophysics: Studies of Emission from the Sun at Metre Wavelengths), 177–210

Melrose, D. B. 1989, Solar Physics, 120, 369

Melrose, D. B. 1990, Solar Physics, 130, 3

Melrose, D. B. 2009, in IAU Symposium, Vol. 257, IAU Symposium, ed. N. Gopalswamy & D. F. Webb, 305–315

Melrose, D. B., Cairns, I. H., & Dulk, G. A. 1986, Astronomy and Astrophysics, 163, 229

Melrose, D. B., Dulk, G. A., & Smerd, S. F. 1978, Astronomy and Astrophysics, 66, 315

Messmer, P., Benz, A. O., & Monstein, C. 1999, Solar Physics, 187, 335

Müller-Mellin, R., Böttcher, S., Falenski, J., et al. 2008, Space Science Reviews, 136, 363

Muschietti, L., Goldman, M. V., & Newman, D. 1985, Solar Physics, 96, 181

Nelson, G. J. & Melrose, D. B. 1985, Type II bursts, ed. McLean, D. J. & Labrum, N. R., 333–359

Neugebauer, M., Wu, C. S., & Huba, J. D. 1978, Journal of Geophysics Research, 83, 1027

Neupert, W. M. 1968, Astrophysical Journal, Letters, 153, L59+

Nindos, A., Aurass, H., Klein, K., & Trottet, G. 2008, Solar Physics, 253, 3

Paesold, G., Benz, A. O., Klein, K., & Vilmer, N. 2001, Astronomy and Astrophysics, 371, 333

Parker, E. N. 1958, Astrophysical Journal, 128, 664

Parker, E. N. 1963, Astrophysical Journal, Supplement, 8, 177

Parks, G. K. & Winckler, J. R. 1969, Astrophysical Journal, Letters, 155, L117+

Petschek, H. E. 1964, NASA Special Publication, 50, 425

Piana, M., Massone, A. M., Kontar, E. P., et al. 2003, Astrophysical Journal, Letters, 595, L127

Pick, M. 1986, Solar Physics, 104, 19

Pick, M., Kerdraon, A., Auchère, F., et al. 2009, Solar Physics, 256, 101

Pick, M. & Vilmer, N. 2008, Astronomy and Astrophysics Reviews, 16, 1

Pilipp, W. G., Muehlhaeuser, K., Miggenrieder, H., Montgomery, M. D., & Rosenbauer, H. 1987, Journal of Geophysics Research, 92, 1075

Press, W., Flannery, B., Teukolsky, S., & Vetterling, W. 1992, Numerical Recipes in C: The Art of Scientific Computing (Cambridge University Press)

Priest, E. & Forbes, T. 2000, Magnetic Reconnection, ed. Priest, E. & Forbes, T.

Priest, E. R. & Forbes, T. G. 2002, Astronomy and Astrophysics Reviews, 10, 313

Ramaty, R., Paizis, C., Colgate, S. A., et al. 1980, in Skylab Solar Workshop II, ed. P. A. Sturrock, 117–185

Raoult, A., Pick, M., Dennis, B. R., & Kane, S. R. 1985, Astrophysical Journal, 299, 1027

Raulin, J., Vilmer, N., Trottet, G., et al. 2000, Astronomy and Astrophysics, 355, 355

Reid, H. & Kontar, E. 2009, AGU Fall Meeting Abstracts, A6+

Reid, H. A. S. & Kontar, E. P. 2010, Astrophysical Journal, 721, 864

Robinson, P. A. & Cairns, I. H. 1994, Solar Physics, 154, 335

Robinson, P. A. & Cairns, I. H. 1998, Solar Physics, 181, 363

Robinson, P. A., Cairns, I. H., & Gurnett, D. A. 1992, Astrophysical Journal, Letters, 387, L101

Robinson, R. D. 1977, Solar Physics, 55, 459

Robinson, R. D. 1985, Flare continuum, ed. McLean, D. J. & Labrum, N. R., 385–414

Ryutov, D. D. 1969, Soviet Journal of Experimental and Theoretical Physics, 30, 131

Sheeley, Jr., N. R., Howard, R. A., Michels, D. J., et al. 1985, Journal of Geophysics Research, 90, 163

Sheeley, Jr., N. R., Howard, R. A., Michels, D. J., et al. 1984, Astrophysical Journal, 279, 839

Smith, D. F. & Riddle, A. C. 1975, Solar Physics, 44, 471

Smith, D. F. & Sime, D. 1979, Astrophysical Journal, 233, 998

Spangler, S. R. 2002, Astrophysical Journal, 576, 997

Steinberg, J. L., Hoang, S., & Dulk, G. A. 1985, Astronomy and Astrophysics, 150, 205

Stewart, R. T. 1974, Solar Physics, 39, 451

Sturrock, P. A. 1964, NASA Special Publication, 50, 357

Sui, L. & Holman, G. D. 2003, Astrophysical Journal, Letters, 596, L251

Sundaram, G. A. S. & Subramanian, K. R. 2005, Monthly Notices of the Royal Astronomical Society, 359, 580

Suzuki, S. & Dulk, G. A. 1985, Bursts of Type III and Type V (Solar Radiophysics: Studies of Emission from the Sun at Metre Wavelengths), 289–332

Suzuki, S. & Sheridan, K. V. 1977, Izv. vuzov. Radiofiz., Tom 20, p. 1432 - 1443, 20, 1432

Sweet, P. A. 1958, in IAU Symposium, Vol. 6, Electromagnetic Phenomena in Cosmical Physics, ed. B. Lehnert, 123–+

Takakura, T. 1982, Solar Physics, 78, 141

Takakura, T. & Shibahashi, H. 1976, Solar Physics, 46, 323

Tandberg-Hanssen, E. & Emslie, A. G. 1988, The physics of solar flares, ed. Tandberg-Hanssen, E. & Emslie, A. G.

Trottet, G., Pick, M., House, L., et al. 1982, Astronomy and Astrophysics, 111, 306

Uchida, Y. 1960, Publications of the ASJ, 12, 376

van Allen, J. A. & Krimigis, S. M. 1965, Journal of Geophysics Research, 70, 5737

van Leer, B. 1974, Journal of Computational Physics, 14, 361

van Leer, B. 1977a, Journal of Computational Physics, 23, 263

van Leer, B. 1977b, Journal of Computational Physics, 23, 276

Vedenov, A. A., Lelikhov, E. P., & Sagdeev, R. Z. 1962, Nucl. Fusion Suppl., 2, 465

Vedenov, A. A. & Ryutov, D. D. 1972, Voprosu Teorii Plasmu, 6, 3

Vilmer, N. 1987, Solar Physics, 111, 207

Vilmer, N., Krucker, S., Lin, R. P., & The Rhessi Team. 2002, Solar Physics, 210, 261

Wang, J. R., Fisk, L. A., & Lin, R. P. 1971, in International Cosmic Ray Conference, Vol. 2, International Cosmic Ray Conference, 438–+

Wang, L., Lin, R. P., Krucker, S., & Gosling, J. T. 2006, Geophysics Research Letters, 33, 3106

Weiss, L. A. A. & Stewart, R. T. 1965, Australian Journal of Physics, 18, 143

Welsch, B. T., Li, Y., Schuck, P. W., & Fisher, G. H. 2009, Astrophysical Journal, 705, 821

Wild, J. P. 1962, Journal of the Physical Society of Japan Supplement, 17, B249+

Wild, J. P. & McCready, L. L. 1950, Australian Journal of Scientific Research A Physical Sciences, 3, 387

Wild, J. P., Murray, J. D., & Rowe, W. C. 1954a, Australian Journal of Physics, 7, 439

Wild, J. P., Roberts, J. A., & Murray, J. D. 1954b, Nature, 173, 532

Wild, J. P., Sheridan, K. V., & Trent, G. H. 1959, in IAU Symposium, Vol. 9, URSI Symp. 1: Paris Symposium on Radio Astronomy, ed. R. N. Bracewell, 176–+

Woo, R. 1996, Astrophysics and Space Science, 243, 97

Woo, R. & Armstrong, J. W. 1979, Journal of Geophysics Research, 84, 7288

Woo, R., Armstrong, J. W., Bird, M. K., & Patzold, M. 1995, Geophysics Research
    Letters, 22, 329

Yoon, P. H., Ziebell, L. F., & Wu, C. S. 2000, Journal of Geophysics Research, 105,
    27369

Young, A. T. 1971, Astrophysical Journal, 168, 543

Zaitsev, V. V., Mityakov, N. A., & Rapoport, V. O. 1972, Solar Physics, 24, 444

Zheleznyakov, V. V. & Zaitsev, V. V. 1970, Soviet Astronomy, 14, 47

Zlotnik, E. Y., Zaitsev, V. V., Aurass, H., Mann, G., & Hofmann, A. 2003, Astronomy
    and Astrophysics, 410, 1011

Zweibel, E. G. & Yamada, M. 2009, Annual Review of Astronomy and Astrophysics,
    47, 291